# PRODUCTION AND DEVELOPMENT OF FLEXIBLE DYE SENSITIZED SOLAR CELLS

A THESIS SUBMITTED TO
THE GRADUATE SCHOOL OF NATURAL AND APPLIED SCIENCES
OF
MIDDLE EAST TECHNICAL UNIVERSITY

BY

BAHADIR CAN KOCAOĞLU

IN PARTIAL FULFILLMENT OF THE REQUIREMENTS
FOR
THE DEGREE OF MASTER OF SCIENCE
IN
METALLURGICAL AND MATERIALS ENGINEERING

AUGUST 2014

Approval of the thesis:

# PRODUCTION AND DEVELOPMENT OF FLEXIBLE DYE SENSITIZED SOLAR CELLS

Submitted by **BAHADIR CAN KOCAOĞLU** in partial fulfillment of the requirements for the degree of **Master of Science in Metallurgical and Materials Engineering Department, Middle East Technical University** by,

Prof. Dr. Canan Özgen ________________
Dean, Graduate School of **Natural and Applied Sciences**

Prof. Dr. Cemil Hakan Gür ________________
Head of Department, **Metallurgical and Materials Eng., METU**

Prof. Dr. Ahmet Macit Özenbaş ________________
Supervisor, **Metallurgical and Materials Eng., METU**

**Examining Committee Members:**

Prof. Dr. Cevdet Kaynak ______________________
Metallurgical and Materials Eng. Dept., METU

Prof. Dr. Ahmet Macit Özenbaş ______________________
Metallurgical and Materials Eng. Dept., METU

Assoc. Prof. Dr. Arcan F. Dericioğlu ______________________
Metallurgical and Materials Eng. Dept., METU

Assoc. Prof. Dr. Caner Durucan ______________________
Metallurgical and Materials Eng. Dept., METU

Assoc. Prof. Dr. Burcu Akata Kurç ______________________
Micro and Nanotechnology, METU

**Date:** __________

**I hereby declare that all information in this document has been obtained and presented in accordance with academic rules and ethical conduct. I also declare that, as required by these rules and conduct, I have fully cited and referenced all material and results that are not original to this work.**

Name, Last Name: Bahadır Can KOCAOĞLU

Signature:

# ABSTRACT

## PRODUCTION AND DEVELOPMENT OF FLEXIBLE DYE SENSITIZED SOLAR CELLS

Kocaoğlu, Bahadır Can
M. S., Department of Metallurgical and Materials Engineering
Supervisor: Prof. Dr. A. Macit Özenbaş

August 2014, 111 pages

Electrophoretic Deposition (EPD) of titania nanoparticles (P-25 Degusa) have been utilized in order to form the nanoporous photoanodes of dye-sensitized solar cells (DSSCs) on flexible polymeric (PEN) substrates. Highly uniform, adherent nanoporous thick films were produced by uniformly dispersing the titania nanoparticles in alcohol based solutions without any binders. Solution performances of each type of alcohols and mixtures of which have been examined considering their coating thickness, morphology and selective anatase deposition yield. Additionally, the effects of acetylacetone addition in solutions on zeta potential and effective particle size of the colloids were investigated. EPD process has been conducted in a single step while the uniformity of the morphology and the thickness of the films were maintained preventing the damage on ITO (Indium Tin Oxide) layer due to excessive voltage exposure. Subsequently, the mechanical compression is applied via cold isostatic pressing (CIP) with a clamping-effect pressure profile in order to obtain 14 - 15 μm film thickness and photon to current conversion efficiency of 4.22 % under AM 1.5 conditions.

**Keywords:** Flexible dye sensitized solar cell, Electrophoretic deposition, EPD, Cold isostatic pressing, CIP.

# ÖZ

## ESNEK BOYA DUYARLI GÜNEŞ GÖZELERİNİN ÜRETİMİ VE GELİŞTİRİLMESİ

Kocaoğlu, Bahadır Can
Yüksek Lisans, Metalurji ve Malzeme Mühendisliği
Tez Yönteticisi: Prof. Dr. A. Macit Özenbaş

Ağustos 2014, 111 sayfa

Elektroforetik kaplama, titanyum diyoksit nano parçacıkları (P-25 Degusa), indiyum kalay oksit kaplı esnek tabanlıklar (ITO/PEN) üzerine biriktirilerek, boya duyarlı güneş gözelerinin fotoanotlarını üretmek amacıyla kullanılmıştır. Oldukça homojen ve kaliteli kaplamalar ve bu kaplamaların seçici anataz kaplama özelliği, nano parçacıkların hiç bir yüzey ajanı kullanmaksızın, alkol bazlı kolloid süspansiyonlarının belirli voltaj değerleri uygulanmasıyla elde edilmiştir. Ayrıca, en çok kullanılan yüzey ajanı olan asetilasetonun etkisi de zeta potansiyel ve efektif parçacık boyutu ölçülerek incelenmiş ve katkısız süspansiyonlarla karşılaştırılmıştır. Son olarak, soğuk izostatik presleme işlemi alternatif baskılama profili ile gerçekleştirilmiş ve hem filmlerin tabanlıkla hem de parçacıkların birbirleriyle olan bağı kuvvetlendirilmiştir. Son ürün olarak ortaya çıkan fotoanotların kaplama kalınlıkları 14 - 15 µm olarak ayarlanmıştır. Üretilen foto anotlar, boya duyarlı "esnek" güneş gözeleri olarak birleştirilmiş ve 4.22 % verimliliğe sahip gözeler AM 1.5 koşulları altında elde edilmiştir.

Anahtar Sözcükler: Esnek boya duyarlı güneş gözeleri, Elektroforetik kaplama, Soğuk izostatik presleme.

*To My Family*

# ACKNOWLEDGEMENTS

I’m highly grateful and honored to be given the chance to prove myself on this M. Sc. Project to my supervisor Prof. Dr. A. Macit Özenbaş also patience, support and guidance of whom during this study.

It has been my pleasure and honor to work and share with my colleagues Halil İbrahim Yavuz, Kerem Çağatay İçli, Murat Güneş, Berk Akbay, Mustafa Burak Coşar. Also, I am very grateful for their support and friendship during this study.

I am very grateful to Metallurgical and Materials Engineering Department, METU for all the support, especially on XRD and SEM analysis for this study. I also want to appreciate METU Central Laboratory for their kind attention during “Zeta Potential” and “Particle Size” analysis.

Additionally, this work is supported by GÜNAM (Center for Solar Energy Research and Applications) at METU. I am very grateful to my colleagues in GÜNAM for their support and attention during profilometer and solar measurements.

Furthermore, I would like to appreciate my friend and colleague Onur Dinçer and TÜBİTAK SAGE for their support and kind attention during this work.

Finally, I want to thank my family, for their patience, support and caring during not only this study but also my whole life.

# TABLE OF CONTENTS

ABSTRACT ............................................................................................................v

ÖZ ..........................................................................................................................vi

ACKNOWLEDGEMENTS.....................................................................................viii

TABLE OF CONTENTS..........................................................................................ix

LIST OF TABLES....................................................................................................xii

LIST OF FIGURES..................................................................................................xiv

LIST OF ABBREVIATIONS................................................................................xviii

CHAPTERS

1. INTRODUCTION..........................................................................................1
2. LITERATURE SURVEY……………………………………………………7
    - 2.1. Features of Photovoltaic Energy Conversion……………………………7
        - 2.1.1. Solar Spectrum and Radiation…………………………………7
        - 2.1.2. Photovoltaic Materials and Devices..........................................9
        - 2.1.3. Semiconductors and pn Junctions...........................................11
        - 2.1.4. Collecting Solar Energy.........................................................13
        - 2.1.5. Transport and Recombination Mechanism.............................14
    - 2.2. Types of Solar Cells..................................................................................16
        - 2.2.1. Gallium Arsenide Solar Cells..................................................16
        - 2.2.2. Cadmium Tellurade Solar Cells..............................................16
        - 2.2.3. Copper (Indium, Gallium) Selenide Solar Cells......................17
        - 2.2.4. Crystalline Silicon Solar Cells................................................17
        - 2.2.5. Thin Film Silicon Solar Cells..................................................19
    - 2.3. Dye Sensitized Solar Cells (DSSC)........................................................19
        - 2.3.1. Components ..........................................................................21
            - 2.3.1.1. Transparent Conductive Oxide (TCO).........................21
            - 2.3.1.2. Nanoporous Photoanode ............................................23
            - 2.3.1.3. Sensitizer Dye ...........................................................25
            - 2.3.1.4. Redox Electrolyte........................................................28

        - 2.3.1.5. Counter Electrode ......................................................29
    - 2.3.2. Working Principle..................................................................29
    - 2.3.3. Electronic Transport Kinetics and Recombination...................31
    - 2.3.4. Production Method of Nanoporous Photoanodes for Conventional DSSCs……………………………………..36
- 2.4. Alternative Production Method of Nanoporous Photoanodes on TCO/Polymer Substrates for "Flexible" DSSC (FDSC)……..…………37
    - 2.4.1. Doctor – Blade Method .........................................................41
    - 2.4.2. Electrophoretic Deposition Method (EPD) .............................42
    - 2.4.3. Cold Isostatic Pressing Method (CIP) ……...............................47

3. EXPERIMENTAL PART...............................................................................49
- 3.1. Materials ..............................................................................................49
- 3.2. Thick Film Deposition and Formation.....................................................50
    - 3.2.1. Preparation of Colloidal Solutions ...........................................50
    - 3.2.2. Primary Characterizations .......................................................52
    - 3.2.3. Electrophoretic Deposition .....................................................53
    - 3.2.4. Secondary Characterizations ...................................................54
    - 3.2.5. Cold Isostatic Pressing ............................................................55
    - 3.2.6. Final Characterizations............................................................57
- 3.3. Assemblage of FDSCs..............................................................................58
    - 3.3.1. Dye Adsorption........................................................................58
    - 3.3.2. Preparation of Electrolyte........................................................58
    - 3.3.3. Preparation of Counter Electrode.............................................58
    - 3.3.4. Assembly and Characterization ..............................................59

4. RESULTS AND DISCUSSION .....................................................................61
- 4.1. Stability and Selective Performances of EPD Colloidal Solutions..........61
- 4.2. Zeta Potential and Particle Size Analysis of Stable EPD Colloidal Solutions.....................................................................64
- 4.3. Electrophoretic Deposition Using Stable Colloidal Solutions…………..69
- 4.4. SEM Characterizations of EPD Coatings................................................70
- 4.5. Current vs Time Analysis of Stable Colloidal Solutions During EPD Process...................................................................79

4.6. XRD Analysis for Selective Anatase Deposition Properties ..................83
4.7. SEM Characterization of Compressed Coatings......................................85
4.8. Solar Performances of Assembled Cells...................................................91
5. CONCLUSION AND SUGGESTIONS........................................................97
REFERENCES ..........................................................................................101

# LIST OF TABLES

TABLES

Table 2.1 Elements of semiconductor materials........................................................10

Table 2.2 Specifications of TCOs for DSSC applications on substrates .....................21

Table 2.3 TCO materials, deposition methods, resistivity ranges and band gap values [21-25] ..............................................................................................22

Table 2.4 Energy band properties and morphologies of anatase and rutile [11, 26, 27] ..........................................................................................23

Table 2.5 Production methods for photoanodes and counter electrodes and obtained efficiencies (η)...........................................................................38

Table 2.6 Solvents used for EPD coatings of several ceramic coatings......................46

Table 3.1 Prepared solutions and specifications.........................................................51

Table 4.1 Prepared colloidal solutions and observation on selective coating, stability and electrophoresis…………………...…………………….……...62

Table 4.2 Candidate EPD colloidal solutions with contents and pH values………...64

Table 4.3 Overall results of zeta potential and mean particle size measurements……………………………………………………………………..68

Table 4.4 Necessary minimum potential difference values for colloidal Solution ..…..…………………………………………………………………69

Table 4.5 Calculation of the empirical constant in Eq. [4.3]………………………..70

Table 4.6 Mean coating thickness and deviations of coating using solutions “IT” and “IA”.....................................................................................77

Table 4.7 Mean coating thickness and deviations of coating using solution “EA” with distinct durations..........................................................................78

Table 4.8 Mean coating thickness and deviations of coatings using solution “ET” with distinct durations..........................................................................78

Table 4.9 Measured coating thickness values of the compressed and non-compressed specimens……………………………………………………………85

Table 4.10 Overall solar performances of the assembled cells..................................93

# LIST OF FIGURES

FIGURES

**Figure 2.1** Solar Radiation Spectrum [13]....................................................................9

**Figure 2.2** Best Research – Cell Efficiencies (2014) [14]...........................................10

**Figure 2.3** Donor and acceptor energy levels in semiconductors [1]..........................11

**Figure 2.4** Schematics of pn junction in semiconductors [15]....................................12

**Figure 2.5** Typical industrial crystalline silicon solar cell structure (a) passivated emitter and real locally diffused (PERL), (b) back contact type [1]............18

**Figure 2.6** Schematic of structure of dye sensitized solar cell [20]..............................20

**Figure 2.7** Schematic view of the structure inside a pore observed in nanoporous photoanode..........................................................................................24

**Figure 2.8** Nanoporous Titania ($TiO_2$) Structure........................................................25

**Figure 2.9** Osmium, Platinum and Iron based organometallic sensitizers [28,29,30] ..........................................................................................26

**Figure 2.10** Ruthenium based organometallic sensitizers [32]...................................27

**Figure 2.11** Energy band diagram and desired electron cycle within the DSSCs [37] ..........................................................................................30

**Figure 2.12** Energy Band Diagram of DSSC with possible electron pathways [32] ..........................................................................................35

**Figure 2.13** Coating mechanism and frame motion [41] …………………………...41

**Figure 2.14** Cross-sectional view of doctor – blade frame [87]..…………………….41

**Figure 2.15** Doctor – blade device for roll-to-roll processing on polymeric substrates [88] ………………………………………………………….42

**Figure 2.16** Schematic view of a colloid with its induction, Stern layer (Debye length) and Zeta potential [89]..............................................................44

**Figure 2.17** Schematic view of cold isostatic pressing chamber [109]........................47

**Figure 3.1** SONOPULS Ultrasonic Probe Homogenizer..........................................52

**Figure 3.2** Integrated MALVERN Nano ZS90 and MALVERN Mastersizer 2000 (METU, Central Lab.)…………………….………………………52

**Figure 3.3** Schematic view of EPD setup...................................................................53

**Figure 3.4** YOKOGAWA GS-610 Source Measure Unit and EPD Setup ..........................................................................................................54

**Figure 3.5** Steps of Cold Isostatic Pressing..............................................................55

**Figure 3.6** Flow AutoClave Engineers CIP 42260….................................................56

**Figure 3.7** Alternating compression profile with given pressure levels......................57

**Figure 3.8** Assemblage of flexible dye sensitized solar cells....................................59

**Figure 4.1** Zeta potential measurement of isopropanol based colloidal Solution……………………………………………………………………..65

**Figure 4.2** Zeta potential measurement of isopropanol based colloidal solution with acetylacetone addition……………………………………………...65

**Figure 4.3** Zeta potential measurement of ethanol based colloidal solution……………………………………………………………….………...66

**Figure 4.4** Zeta potential measurement of ethanol based colloidal solution with acetylacetone addition……………………………………………...66

**Figure 4.5** Particle size distributions of the four stable colloidal solutions……………………………………………………...………………...67

**Figure 4.6** Modelling of the limited dispersion effect of acetylacetone in ethanol based colloidal solutions…………………………………………………...68

**Figure 4.7** The SEM image of coating by using colloidal solution "IT" with applied 11 V for 60 s……………………………………………………..71

**Figure 4.8** The SEM image of coating by using colloidal solution "IA" with applied 9 V for 60 s………………………………………………………72

**Figure 4.9** The SEM image of coating by using colloidal solution "EA" with applied 5 V for 60 s……………………………………………………...73

**Figure 4.10** The SEM image of coating by using colloidal solution "EA" with applied 5 V for 120 s……………………………………………………..74

**Figure 4.11** The SEM image of coating by using colloidal solution "ET" with applied 5 V for 60 s………………………………………………………75

**Figure 4.12** The SEM image of coating by using colloidal solution "ET" with applied 5 V for 60 s……………………………………………………...76

**Figure 4.13** The SEM images of coating by using colloidal solution "ET" with applied 5 V for (a) 180 s and (b) 240 s………………..…………………...77

**Figure 4.14** The graph of coating thickness vs coating duration................................79

**Figure 4.15** The change in the current vs time graph for all colloidal solutions with distinct voltage values..........................................................................80

**Figure 4.16** Current vs time graphs for solutions "ET" and "EA" at 5V of applied voltage..........................................................................................82

**Figure 4.17** The schematic view of the aim of the selective anatase coating before and after EPD process……………………………………………….83

**Figure 4.18** XRD spectra of coatings by using solutions “EA”, “ET” and as received P-25 particles……………………………………………………….84

**Figure 4.19** SEM image of the photoanode compressed at 150 MPa………………86

**Figure 4.20** SEM image of the nanoporous structure of photoanode compressed at 150 MPa…………………………………………………….……..87

**Figure 4.21** SEM image of the photoanode compressed at 225 MPa…………..……88

**Figure 4.22** SEM image of the nanoporous structure of photoanode compressed at 225 MPa…………………………………………………….……..89

**Figure 4.23** SEM image of the photoanode compressed at 300 MPa……………..……90

**Figure 4.24** I-V curves of assembled cells................................................................91

**Figure 4.25** Incident photon to current conversion efficiencies (IPCE) of the assembled cells..........................................................................................94

# LIST OF ABBREVIATIONS

| | |
|---|---|
| c-Si | Crystalline Silicon |
| CIGS | Copper Indium Gallium Selenide |
| DSSC | Dye Sensitized Solar Cell |
| FDSC | Flexible Dye Sensitized Solar Cell |
| TCO | Transparent Conductive Oxide |
| HOMO | Highest Occupied Molecular Orbit |
| LUMO | Lowest Unoccupied Molecular Orbit |
| EPD | Electrophoretic Deposition |
| CIP | Cold Isostatic Pressing |
| IT | Non-additive Isopropanol Solution |
| IA | Acetylacetone Additive Isopropanol Solution |
| ET | Non-additive Ethanol Solution |
| EA | Acetylacetone Additive Ethanol Solution |
| SEM | Scanning Electron Microscopy |
| XRD | X-Ray Diffraction |
| CIP# | The Sample Compressed at # MPa |

# CHAPTER 1

# INTRODUCTION

Worldwide necessity on renewable, clean energy sources along the past several decades has been increased, tremendously. Although, the majority of the energy sources being utilized such as fossil fuels, natural gas and coal have been able to provide the demand almost completely, the $CO_2$ exposure into the atmosphere resulted in global warming with possible consequences of inevitable climate changes and toxic effects of habitat. Additionally, due to the limited quantities of such energy sources, the cost of energy has been increasing over time as well as decrement in availability of such resources. Several governments have established medium term solutions to such availability and cost issues of commercial energy sources by promoting the utilization of renewable energy sources such as wind, bio-fuel, geothermal and solar energy. Considering all those renewable energy sources, solar energy is perceived the most available with the highest efficiency on performance, cost and $CO_2$ emission issues. There exits two ways of using solar energy, one is using solar thermal energy by collecting the solar energy to heat up the water which is also used to heat up indoor facilities, or by harvesting the solar spectrum and conversion of which directly into electricity using photovoltaic devices. In order to obtain reliable efficiency from solar thermal systems, it is vital to have intense solar radiation and ambient temperature; on the other hand, most of the photovoltaic devices are able to operate under medium and low radiation regions while having a large ambient temperature range. However, due to excessive production costs of photovoltaic devices, comparing with the other commercial and renewable energy sources, this technology still goes through as a medium term alternative energy source. Therefore, photovoltaics are, nowadays, the most popular research field among the other renewable energy alternatives [1].

The production costs of photovoltaic devices around the world differentiate due to labor costs, market share and government regulations. For instance, in Germany, factory gate prices of c-Si modules was 2.34 €/W [2]. Considering lower efficiency solar modules of a-Si and CdTe thin film solar cells the production costs were around 1.50 €/W among the Europe [2]. For an overall review, a study indicated established c-Si solar module production facility with a capacity of 347 MW in US and Germany, due to lower labor and raw materials costs China was able to provide 25% lower costs [3]. However, it has been observed that unit prices of energy production decreasing with the increasing system sizes, such that from small scale (2 kW) to large scale (600kW) unit prices decrease from 9.2 \$/W to 6.5 \$/W, in US. To sum up, comparing the average prices of established systems in 2008, in Germany 6.1 \$/W, in Japan 6.9 \$/W and in US 7.9 \$/W, such prices continues to decrease along 2009 [4].

It is possible to indicate that the solar energy market has been dominated by Si based photovoltaic materials and devices. Best solar harvesting efficiencies have been obtained with single crystal Si solar modules, among Si based photovoltaics. The production of single crystal, or even poly crystal Si wafers requires very high temperature (~1600 $^{o}$C) and vacuum levels ($10^{-6}$ mbar) such that this consists of the majority of the production costs. Therefore, new generation of photovoltaics have been introduced to the literature such as organic solar cells, polymeric solar cells and dye-sensitized solar cells.

Among these, dye sensitized solar cells (DSSC) perceived to be a highly promising photovoltaic devices due to low materials and fabrication costs and also less complex production methods such that it does not require very high processing temperatures and vacuum levels. Thus, dye-sensitized solar cells are one of the most cost effective and versatile alternative for common p-n junction solar cells. Remarkable efficiency values of 10.1 % [6], 11 % [6], 12 % [7] have been reported during the past few years.

Unlike p-n junction photovoltaics, its unique working principle provides efficient low radiation light harvesting properties [5]. The c-Si solar modules require 48.5$^{o}$ of incident light angle and 100 mW/cm$^2$ solar radiation intensity to exhibit high efficiency values. However, despite the lower obtained efficiency values than that of c-Si solar cells, its performance does not effected by the intensity of the radiation or the angle of the incident light. Therefore, such property makes DSSCs indoor applicable photovoltaic devices. Additionally, due to its architecture (which will be explained later), it is possible to manufacture DSSCs on flexible substrates leading them to be able to utilize for mobile and daily applications. Combining these two properties, it is possible to manufacture “flexible” dye sensitized solar cells (FDSC) in order to obtain in-situ recharging of several mobile electronic devices such as mobile phones, tablets, laptop computers as well as other civil and military applications.

Fabrication of conventional DSSC simply requires deposition $TiO_2$ nanoparticles on a TCO coated glass substrate by screen printing of a dispersion paste of which, following firing at 550 $^{o}$C in order to form a nanoporous thick film. Accordingly, the most challenging part of such fabrication is the deposition and formation of titania nanoporous thick film on polymeric substrates due to the impossibility of a sintering process as for the conventional ones. Therefore, several different methods such as low temperature volatile paste deposition by screen printing, doctor blade and deposition titania nanoparticles by using electrophoretic deposition to fabricate dye sensitized solar cells on flexible substrates. The fabrication of DSSC on flexible polymeric substrates is possible and relatively efficient such that some commercial applications were introduced [8, 9, 10].

Several methods have been introduced in order to deposit titania nanoparticles and to form the nanoporous structure:

Primary Processes:

- Doctor blade via low-temperature non-viscous volatile pastes
- Screen printing via low-temperature non-viscous volatile pastes
- Oxidative anodization on titanium foils
- Oxidative titanium sputtering on titanium foils

- Conventional photoanode processing for $SiO_x$ – FTO coated stainless steel foils
- Electrophoretic Deposition (EPD)

Secondary Processes:

- Heat Treatment at < 140 $^{o}$C (Glass transition temperature of PEN)
- Hydraulic Uniaxial Pressing
- Cold Isostatic Pressing (CIP)

Indicated in primary processes are the deposition methods for titania on the flexible substrates. Doctor blade and screen printing methods are applied for polymeric (PEN/PET) substrates while the given two oxidative processes are applied for Titanium foils. Using stainless steel foils as flexible substrates is slightly challenging. Due to lattice mismatch in between stainless steel and FTO coating, an intermediate layer of silica ($SiO_x$) is deposited which also resulted in challenges on taking contacts by deposition of an insulator layer between substrate and FTO. Although, the mechanical stabilities of metal foil based DSSCs are higher, the light harvesting can be achieved only from the counter electrode side which is mainly Pt coated ITO/PEN. Therefore, flexible polymeric substrates are cheap, practical, light-weight and efficient. However, unlike metal substrates, fabrication on polymeric substrates requires secondary completing process due to the impossibility of a high temperature process. Although, the doctor blade and screen printing methods are more popular for the fabrication on polymeric substrates, electrophoretic deposition technique is the most promising, practical and reliable process in order for metal oxide nanoparticles to be deposited. The specifications of this technique is explained in section 2.4.2.

As mentioned in secondary processes, polymeric substrates (e.g. PEN) cannot withstand temperature exceeding 140 $^{o}$C. Therefore, heat treatments conducted at around that temperatures are considered as simple drying and removal of volatile organics like ethanol. Therefore, in order to provide mechanical stability and interparticular coalescence of metal oxide nanoparticles, two types of compression processes are applied. Although, uniaxial compression is reported as a good secondary process for formation of a nanoporous layer, there is an extensive possibility of damaging the ITO coating as well as the titania layer. Since the polymeric substrates are highly flexible, compression of 1 ton/cm$^2$ results in bulging and increased stress concentrations at interface; hence, cold isostatic pressing is accepted to be the most suitable compression method. Additionally, using CIP, the attainable and the applicable pressure levels are much higher than the uniaxial compression. Therefore, CIP technique is included to this study as a complementary process.

In this study, binder-free EPD coating with its selective coating properties by adjustment of pH value of the colloidal solution were investigated. Since commercially available P-25 (Degusa, Germany) contains two phases of titania which are anatase (80%) and rutile (20%), it is perceived to obtain a cost and time effective process to coat only anatase particles on the substrate by EPD method. In DSSC, the desired phase of titania is anatase due to its band gap, morphology and dye adsorption properties [6, 7, 11]. In order to provide a rutile-free deposition, we desire to take benefit of the difference in the isoelectric points of anatase (pH 6.3) [23] and rutile (pH 5.2-5.3) [12] and prepare a colloidal solution resulting in idle rutile colloids and mobile anatase colloids, simultaneously. Afterwards, subsequent CIP process was applied on the substrates to increase the nanoparticle interaction and mechanical stability by optimizing a pressure profile.

# CHAPTER 2

# LITERATURE SURVEY

## 2.1. Features of Photovoltaic Energy Conversion

Although, photovoltaic effect was observed by Becquerel about a century ago, photovoltaic energy conversion concept had not been a popular research topic until 1970s. At that time, solar energy conversion concept was motivated by space and satellite researches and applications due to necessity of a long lasting, renewable energy source. The main features of photovoltaic energy conversion concept are:

- Completely renewable,
- Highly durable,
- Easy repair and maintenance (direct conversion of solar energy into electricity, almost no need for mechanical moving parts)
- Abundant raw material resource (e.g. Si, Al, P, etc...)
- Versatile utilization region worldwide,
- Promotion and legislation for applications of photovoltaics by governments and companies,
- Accelerated decrease in production costs.

### 2.1.1. Solar Spectrum and Radiation

Sunlight is an electromagnetic radiation of photons carrying energy. Due to its wave-like motion along its path, the energy carried by a photon, $E_\lambda$ is denoted with the equation:

$$E_\lambda = \frac{hc}{\lambda}$$

Eq. [2.1]

where h is the Planck's constant, c is the speed of the light and λ is wavelength of the radiation.

Although the sun has an almost spherical shape and thus, homogeneous energy emission from its surface, the homogeneity of the incident solar radiation on the earth is deteriorated by atmospheric absorption, refraction and reflection interactions. Therefore, it is important to define "air mass" term in order to calculate such interaction parameters such that flux of solar radiation is calculated for several standard conditions. Air mass (AM) equation is denoted by:

$$Air\ Mass = \frac{1}{\cos\theta}$$

Eq. [2.2]

where θ is angle incidence.

Estimated temperature of the surface of the sun has been calculated at around 5250 $^o$C by its black-body radiation. AM 0 condition stands for zero air mass which means that the solar energy per unit area above the atmosphere is calculated. The solar energy flux for AM 0 conditions is 1353 kW/m$^2$. Considering the atmospheric conditions, taking the sea level as the reference point AM 1.5 conditions occur. The solar energy flux for AM 1.5 conditions is 1 kW/m$^2$.

Electromagnetic energy emission from the sun is not monochromatic i.e. it is a beam with different wavelengths of electromagnetic radiation which is shown in Fig 2.1.

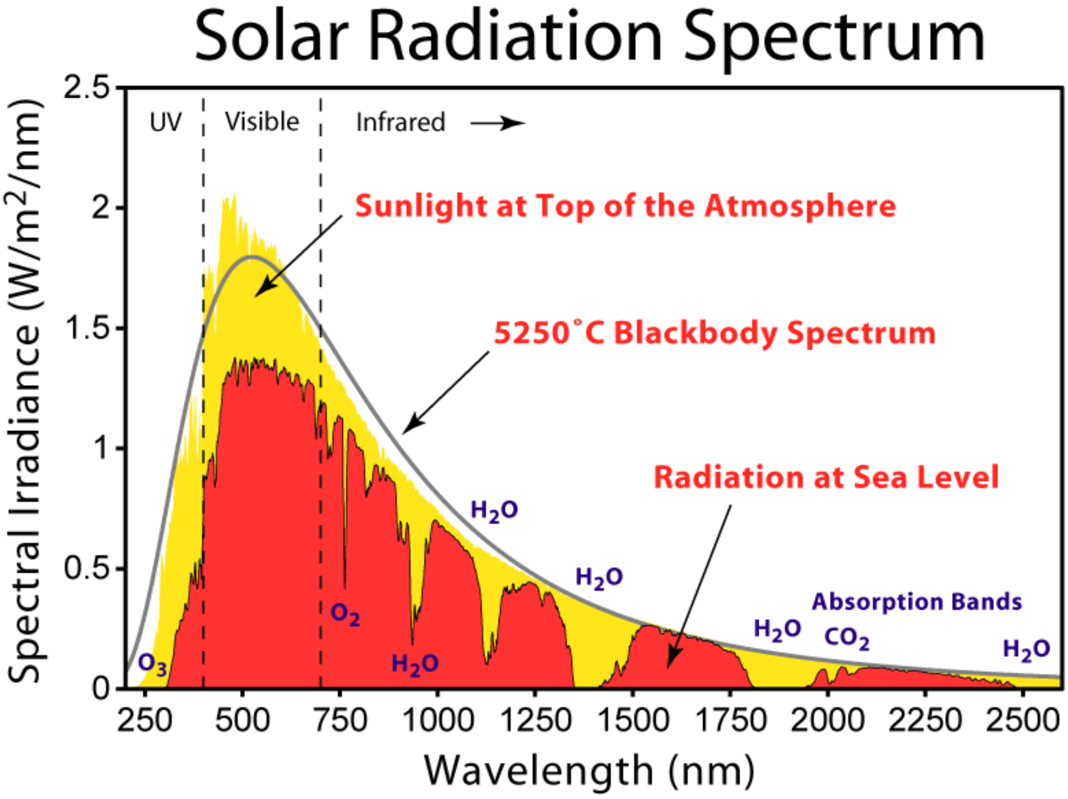

Figure 2.1 Solar Radiation Spectrum [13].

Discontinuities in the distribution of fluorescence observed due to absorption by $CO_2$, $H_2O$ and $O_2$ present in the atmosphere of the earth. Due to such absorption in distinct bands, the incident light intensities of UV and infrared regions of the spectrum are decreased dramatically. Therefore, the photovoltaics which are produced to be used on earth are designed to operate for absorption of visible range and near infrared range and its conversion.

### 2.1.2. Photovoltaic Materials and Devices

Photovoltaic devices require “semiconductor” materials due to their characteristic light absorption and electron transport features. Semiconductor materials have their characteristic energy band gap values such that they are also perceived as intermediate materials in between conductors and insulators. Semiconductor materials were, initially, defined as Group IV elements, afterwards III-V, II-VI and I-III-VI compounds have been utilized. In table 2.1, the elements and their groups are tabulated, accordingly.

Table 2.1 Elements of semiconductor materials

| I | II | III | IV | V | VI |
|---|---|---|---|---|---|
|  |  | B | C | N | O |
|  |  | Al | Si | P | S |
| Cu | Zn | Ga | Ge | As | Se |
| Ag | Cd | In | Sn | Sb | Te |

As mentioned before solar energy system market has been dominated by Si (Group IV), Cu(In,Ga)Se (I-III-VI) and CdTe (II-VI) solar modules. Additionally, GaAs (III-V) solar modules are widely used in space and satellite applications due to its tremendous efficiency values under AM 0 conditions, unlike Si, CdTe or Cu(In,Ga)Se solar modules. Differing utilization regions and distinct efficiency values of solar cells, best research-cell efficiencies have been plotted on Fig 2.2.

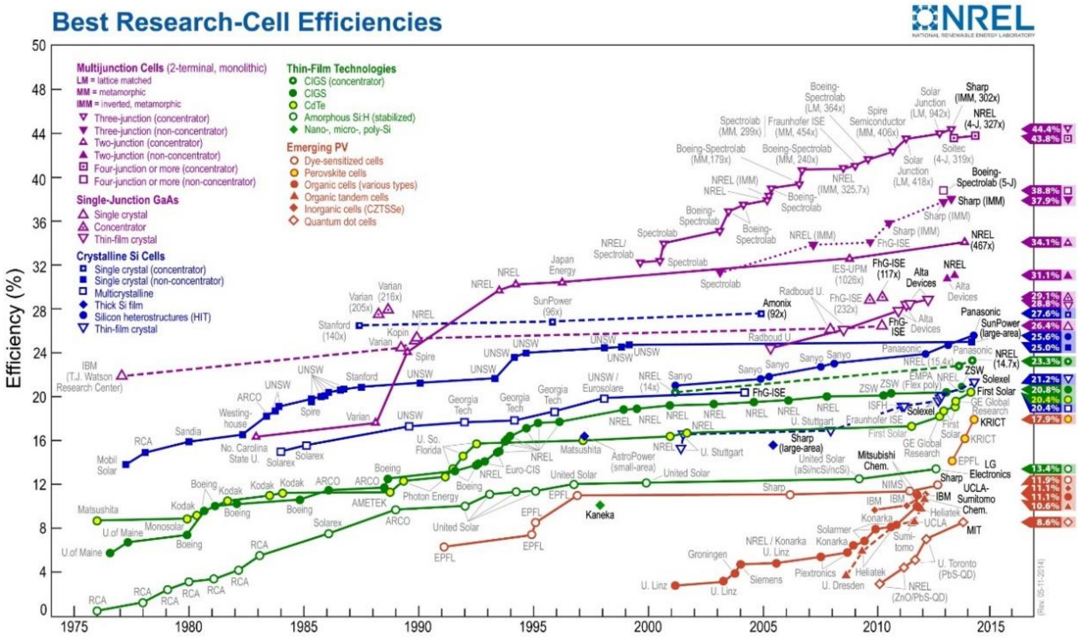

Figure 2.2 Best Research – Cell Efficiencies (2014) [14].

### 2.1.3. Semiconductors and pn Junctions

Semiconductors, due to their characteristic band gap values provide not only for solar cells but also for other microelectronic devices, desired optical and electronic properties. Energy band gap in between valance band and conduction band prevents excitation of electrons such that conductivity is not achieved unless the required energy is not applied to the material. Such state of semiconductors are called intrinsic state. However, semiconductor materials can be modified in order to increase its conductivity via doping by introducing donor or acceptor levels on the energy band gap. This is called extrinsic semiconductor materials. In Fig.2.3, donor and acceptor levels are shown with the energy levels along the energy band gap.

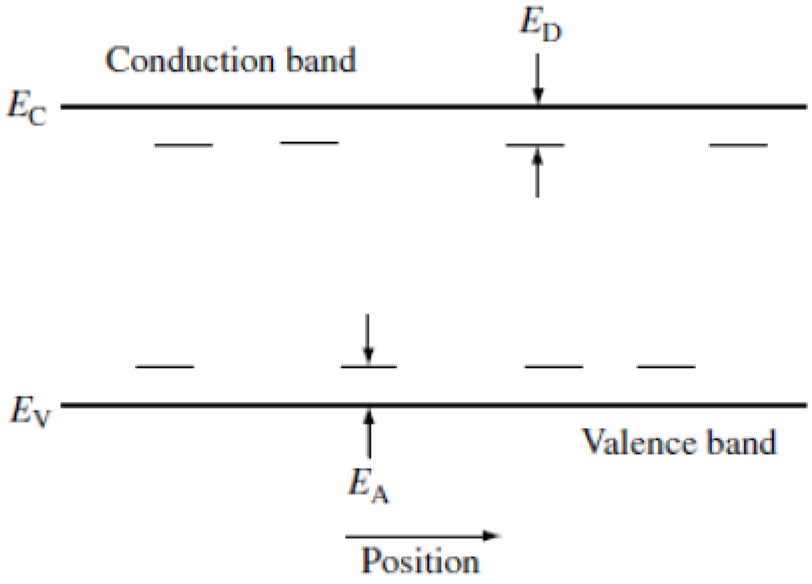

Figure 2.3 Donor and acceptor energy levels in semiconductors [1].

Although, semiconductor materials can vary in accordance with the elemental group combinations, doping mechanism does not vary amongst. For instance, considering pure Si (IV), it is an intrinsic semiconductor. Doping with a group III element (at ppm) like Al, B, etc. results in a p-type (positive) extrinsic Si by increasing the concentration of holes as charge carriers. Similarly, doping with group V elements like P, Sb, etc.

results in n-type (negative) extrinsic Si increasing the concentration of electrons as charge carriers.

Semiconductors with its unique properties provide stability in conductivity within a temperature range. It is known that the conductivity of metals decreases with the increasing temperature due to increasing frequency of atomic vibrations. However, semiconductors with characteristic band gap values lead to thermal threshold values such that within a specific temperature range, the conductivity remains constant.

Another advantage of utilization of semiconductors are revealed by forming p-n junction between two of which.

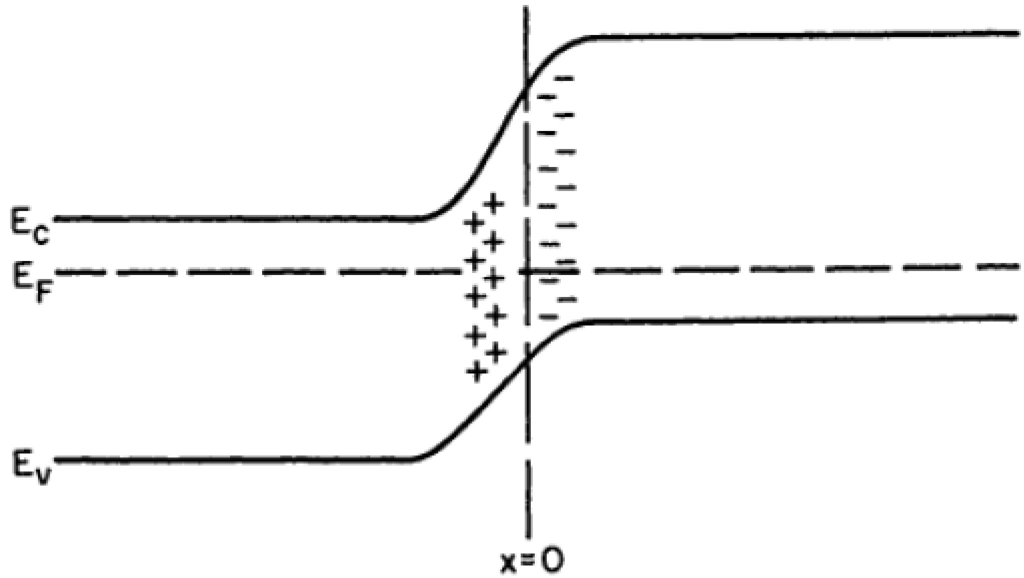

Figure 2.4 Schematics of pn junction in semiconductors [15].

In Fig.2.4 the occurrence of band gap bending at the p-n junction interface is shown. Along the interface due to the excess amounts of holes and electrons in p-type and n-type semiconductors, respectively, the charger carriers diffuse into each other resulting in an identical Fermi energy level ($E_F$). Such effect also leads to a favorable separation of holes and electrons at the interface. Solar cells are also produced by forming a p-n junction in which the formation of electrical field along the interface by incident solar energy, the electron hole pairs are separated from each other.

### 2.1.4. Collecting Solar Energy

As mentioned before, in order to convert solar energy into electrical energy, a charge separation is necessary at the p-n junction by the incidence of light. Therefore, it is vital to consider the three possibilities of interaction in between incident light and the semiconductors:

- Reflection
- Transmission
- Absorption

Reflection mechanism depends on mostly the atomic confinement along the surface of the materials rather than energy band gap values. Thus, transmission and absorption mechanisms are considered opposing interactions depending on the energy band gap values. Actually, if the energy of the incident photon exceeds the energy band gap value, then the photon is absorbed and the electron is excited from valance band to conduction band of the material. Otherwise, the electron in the valance band cannot be excited up to the conduction band and the light is not absorbed i.e. transmission of light occurs.

In quantum mechanics point of view, the case is not that simple as mentioned above. Since semiconductors are also classified having direct and indirect band gaps, the lattice momentum and emission of phonons are involved in the absorption mechanism of light. Considering direct band gap semiconductors, the highest energy level of the valance band has the identical lattice momentum with the lowest energy level of the conduction band. Thus, for direct band gap semiconductors the absorption mechanisms can be fulfilled independent from material thickness. However, for indirect band gap semiconductors, highest level of the valance band and lowest level of the conduction band have opposite lattice momentums such that, since incident light cannot result in phonon emission or absorption, the material has to provide its own momentum confinement. Therefore, increasing material thickness results in increasing atomic vibrations and phonons prohibiting electron excitation from valance band to conduction band. Considering c-Si solar cells a minimum thickness of 200 μm is necessary while GaAs solar cells requires much less.

In addition to such band to band transitions of electrons, some electrons already in the conduction band can absorb photons being excited to higher levels within the band. However, such a non-transitional excitation of electron does not create an electron hole pair and considered as a loss.

### 2.1.5. Transport and Recombination Mechanisms

Incidence of light leads to formation electron-hole pairs at interface of p-n junctions. Normally, electrons and holes in semiconductors are in equilibrium unless an external energy is absorbed. Excitation of the electron to the conduction band by such an energy source leaves a hole in the valance which is called an electron-hole pair. The electric field along the p-n junction interface forces the electron-hole pairs to separate and transports each to opposite directions within the semiconductor. At the interface region holes move towards and along p-type semiconductor and electrons move towards and along the n-type semiconductor. These separated electrons and holes are called as "minority carriers" which is due to the fact that in normal conditions the diffusion of electrons are expected to occur towards p-type semiconductor and vice versa, which are also called "majority carriers".

Due to the existence of two distinct charge carriers (holes and electrons), it is important to calculate the mobility and the current densities of which, separately. In the Eq. [2.3] and [2.4] the current densities are calculated for electrons and holes, respectively.

$$J_n = q\mu_n n\varepsilon + qD_n\nabla_n$$

Eq. [2.3]

$$J_p = q\mu_p p\varepsilon - qD_p\nabla_p$$

Eq. [2.4]

In the upper equations “n” and “p” stands for electron and hole concentrations, respectively; while μ is the mobilities, D is the diffusivities, q is the elementary charge and ε is the electrical field.

In semiconductors whether it is p-type or n-type, the transport mechanisms depend on two phenomena:

- Drift
- Diffusion

These terms are not only material properties but also may vary due to temperature, dopant type and quantity, impurities, crystal structure, defects, dislocations and grain boundaries. In general, defects and undesired impurities in semiconductors lead to decrease in the mobilities and the diffusivities. Therefore, semiconductors used in such applications are produced as almost 100% (excluding dopants) pure and single crystal. Otherwise, defect assisted recombinations occur such that trap sites are formed within the band gap due to such defects. Point defects within the semiconductors act as p-type dopant such that simultaneous doping with N or Al leads to formation of 2 distinct energy bands within the band gap. The energy band due to point defects are called “trap sites” to where the excited electrons will remain as idle or return back to valance band. Similarly, dislocations and grain boundaries lead to such trap sites as well as hindering the motion of electrons and holes within the material, severely.

Another, recombination and loss mechanism is the one occurs due to the surface states of semiconductors. Since material surfaces are composed of open bonds, in other words, contain unbound atoms, every surface can be considered as defects. Surfaces are high energy regions such that recombination rates of charge carriers reaching to the surfaces increases, dramatically. Therefore, surface passivations are vital for semiconductors in order to decrease such recombination losses.

## 2.2. Types of Solar Cells

### 2.2.1. Gallium Arsenide (GaAs) Solar Cells

GaAs solar cells (III-V) are widely used for satellite applications due to its extensive efficiency values at around 44% for multi junction and 29% for single junction under AM 0 conditions and optimum band gap value of 1.42 eV [29]. Not only its optimum band gap but also its direct band gap structure provides absorption and conversion of the most intense part of the solar spectrum. Additionally, its direct band gap allows the production of which with a very low thicknesses such that material costs and lightweight conditions are satisfied as versatile as possible. However, GaAs solar cells are highly toxic mostly due to arsenic content and highly expensive for commercial use on daily basis.

GaAs solar cells can be produced via molecular beam epitaxy, MDVPE and liquid phase epitaxy methods. Also, doping can be conducted via addition of Al or Zn to obtain extrinsic properties. GaAs solar cells are produced by deposition of p-type and n-type of which, sequentially on GaAs substrates. Recently, studies have conducted in order to replace GaAs substrates with other semiconductors like Si and Ge. However, due to excessive thermal expansion mismatch, studies have failed [16].

### 2.2.2. Cadmium Tellurade (CdTe) Solar Cells

CdTe solar cell is a II-VI compound which is also denoted as metal chalcogenides. CdTe has a band gap value of 1.45 eV, almost identical to GaAs solar cells. Although the theoretical efficiency value has been determined as 29%, best cell efficiency obtained is around 20% while best module efficiencies are less than 10%. CdTe is a robust material such that due to its highly strong ionic bonding structure, it is highly stable in open environment and open space conditions. CdTe has an excellent absorption coefficient and hole conductivity within. Thus, those solar cells are fabricated by forming a p-n junction of p-type CdTe and n-type CdS. Initially, CdTe solar cells are produced via sputtering and vacuum assisted PVD techniques. Recently, more flexible and low cost techniques like electro deposition, CVD, screen-printing, spray pyrolysis have been applied. Despite the promising performances and stability due to its Cd content, it has been perceived as toxic, in the recent years [17].

### 2.2.3. Copper (Indium, Gallium) Selenide (CIGS) Solar Cells

CIGS is one of the most promising type of solar cells as a I-III-V compound of semiconductors. The energy band gap values can be tailored in accordance with the application areas like space or atmospheric conditions. Adjusting the In/Ga ratio the band gap of the absorber layer can be altered from 1.04 to 1.7 eV, mostly manufactured with 1.1 – 1.2 eV band gap values. Similar to CdTe solar cells, CIGS solar cells have excellent absorption properties as well as direct band gap properties. The best cell efficiency obtained is at around 20% while best module efficiency is 12-14%, one of which has monolithic interconnected structure with a surface area of 3459 $cm^2$ [29,33]. Similarly, CIGS is a remarkable p-type material with an excellent hole conductivity and heterojunction is obtained by layer deposition of n-type CdS on Mo coated (Sputtering) ceramic substrates (as back contact). Top contact materials are mainly high band gap transparent conductive oxides (TCO) like ITO or ZnO. Fabrication methods for CIGS are also versatile such that sputtering, co-evaporation, electro deposition and spray pyrolysis techniques can be used [1].

### 2.2.4. Crystalline Silicon (c-Si) Solar Cells

Silicon based solar cells have been dominating the photovoltaic industry over the last 20 years. Due to its robust raw material source which is silica (Si from $SiO_2$), crystalline Si solar cells are considered as the most cost effective photovoltaics. Si based solar cells are divided into three groups:

- Single Crystal Silicon Solar Cells
- Poly Crystal Silicon Solar Cells
- Amorphous Silicon Solar Cells

Unlike other photovoltaics mentioned above, single crystal silicon solar cells are produced from bulk silicon ingots by Czochralski technique. The silicon precursor is purified with successive melting – solidifying steps such that impurity content is less than tens of ppm. Poly crystal silicon is also purified similarly, however production of silicon ingots are completed with conventional solidification. Czochralski method requires a single crystal quartz seed with a specified lattice planes, (100) or (111), the silicon ingot has been solidified – grown with such specific crystal orientation as single crystal.

Due to its indirect band gap of 1.17 eV, it requires wafers cut into 200-300 μm as mention in section 2.1.4. Considering p-n junction fabrication, p-type Si is produced during Czochralski process while the Si is still in liquid phase. Unlikely, n-type Si is produced via diffusion techniques on wafer states. In a vacuum assisted quartz furnace, wafers are subjected to phosphorus (P) ambient environment in order to obtain the diffusion of P into Silicon wafers at one half of which. Right before obtaining such p-n junction, several etching steps are introduced in order to remove saw damages (with acidic solutions) and to obtain surface passivation by NaOH. Afterwards, junctions are isolated and antireflective coating is applied ($Si_3N_4$). Finally, silver or aluminum contacts are printed and fired.

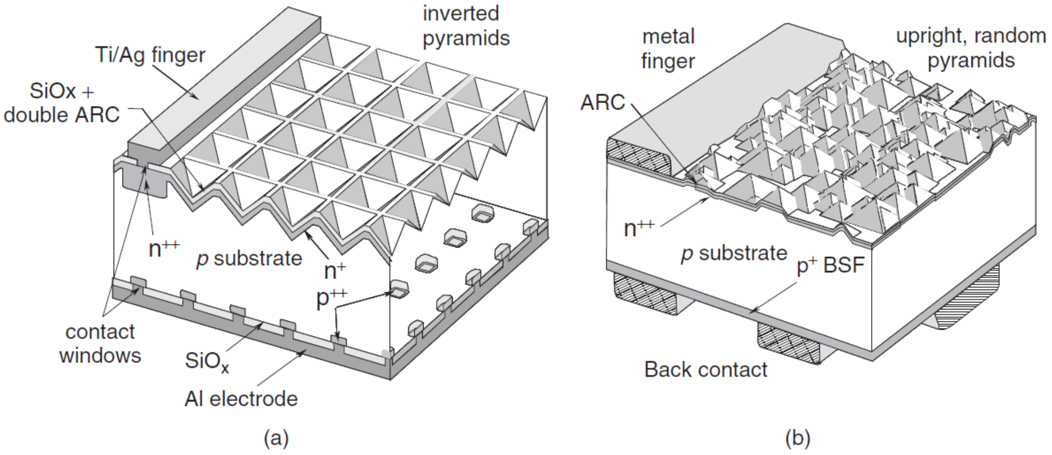

Figure 2.5 Typical industrial crystalline silicon solar cell structure (a) passivated emitter and real locally diffused (PERL), (b) back contact type [1].

The efficiencies obtained for c-Si solar cells are reported to be 27.6% with concentrator which is almost the theoretical limit, while conventional c-Si solar cells have 25.6% efficiencies. Additionally, multicrystalline solar cells have at most 21.2% efficiency and amorphous silicon has only 13.4% efficiency value due to its highly defective and short range ordered structure. In large scale module production, c-Si solar modules are reported to exhibit efficiency values at around 20%.

Single crystal silicon solar cells are the most widely used for commercial light harvesting applications with a warranty of 20 years. [14,19]

### 2.2.5. Thin Film Silicon Solar Cells

Although the raw material cost for crystalline silicon solar cells are low, due to processing into highly pure and single crystalline state increases the overall costs, dramatically. Therefore, thin film coatings of Si have been in concern over the last few years. In order to carry out such thin film coating approach several coating methods have been applied such as evaporation, CVD, liquid phase epitaxy, sputtering of silicon layers on substrates. However, as mentioned before due its indirect band gap, absorption of light for such thin film coatings are highly low. Therefore, light scattering layers, concentrators and several other light trapping techniques are required. Best cell efficiencies are reported to be at around 16% [1,14,17].

## 2.3. Dye Sensitized Solar Cells (DSSC)

Dye sensitized solar cells are one of the most promising 3rd generation solar cell type such that its working principle is completely different from commercial p-n junction type photovoltaics. Actually, its working principle is identical to photosynthesis observed in plant leaves. As already mentioned in its name, dye sensitization is a sort of chlorophyll present in plant cells, therefore, DSSCs can also be called as “artificial chloroplasts”. In order to explain its working principle, it is important to identify components of DSSCs:

- Transparent Conductive Oxides (TCO) for Electrode
- Wide Band Gap Semiconductor
- Dye Molecules Adsorbed on Semiconductor Surface
- Redox Electrolyte
- Catalyst Coating on TCO as Counter Electrode

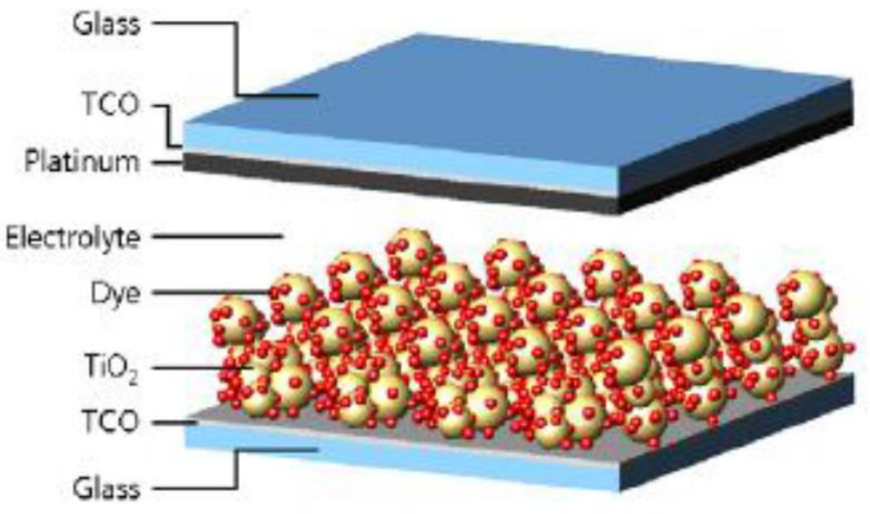

Figure 2.6 Schematic of structure of dye sensitized solar cell [20].

As shown in fig. 2.6, metal oxide nanoparticles ($E_g$ >3.1 eV) which are transparent are deposited on TCO coated transparent substrates as wide band gap semiconductors and interconnected with each other to form a nanoporous structure. Dye molecules reside on the surface of the metal oxide particles adsorbed which is called “dye sensitization”. A redox electrolyte (liquid or gel) is placed in between dye sensitized electrode and catalyst coated TCO counter electrode substrate [1].

### 2.3.1. Components

#### 2.3.1.1. Transparent Conductive Oxide (TCO)

Transparent conductive oxides (TCO) are widely used not only for photovoltaics but also for other optoelectronic devices. TCO materials used in DSSC applications are mainly fluorine doped tin oxide (FTO) or tin doped indium oxide (ITO). Utilization of which varies with the deposition and nanoporous thick film formation methods. Although ITO exhibits better transparency/sheet resistance performance, the stability of ITO diminishes at temperatures more than 300 $^{o}$C [1]. Therefore, for the processes that require more than such temperatures, FTO is used as TCO material.

As mentioned before ITO or FTO is used as TCO material in given conditions. Since production of conventional DSSCs requires firing at 550 $^{o}$C in order to form nanoporous structure, FTO is desired for such applications. However, due to better transparency and conductivity of ITO, for flexible polymeric substrate ITO is coated as TCO layer. Table 2.2 shows the specifications of FTO and ITO layer on glass or polymeric substrates.

Table 2.2 Specifications of TCOs for DSSC applications on substrates

| **TCO** | **Sheet Resistance (Ω/□)** | **Transparency (at 550 nm)** | **Substrate** |
|---|---|---|---|
| ITO | 3 – 8 | 80% | Glass |
| ITO | >45 | 80% | PET |
| ITO | <15 | 80% | PEN |
| FTO | 8 – 15 | 80% | Glass |

In order to obtain transparency it is crucial to have a wide band gap, preferably larger than 3.1 eV (visible spectrum edge). Thus, oxide materials are highly suitable for such property to be satisfied. However, increasing band gap, also leads to decrease in the electrical conductivity. In fact, such materials are good insulator. Therefore, it is impossible to obtain transparent and conductive oxides without doping. Mainly, n-type doping is conducted to the metal oxides (exception: NiO as p-type) by which the band gap value can be adjusted as desired. Table 2.3 shows the commonly used TCO materials, deposition methods, resistivity and band gap values.

Table 2.3 TCO materials, deposition methods, resistivity ranges and band gap values [21-25]

| **TCO** | **Deposition methods** | **Dopant** | **Resistivity range ($10^{-4}$ Ωcm)** | **Intrinsic band gap (eV)** |
|---|---|---|---|---|
| **$SnO_2$** | APCVD, spray pyrolysis | F. Sb, Cl | 3 – 8 | 3.6 |
| **ZnO** | Sputtering, PLD, LPCVD, APCVD | Al, Ga, B, In, F | 1 – 8 | 3.3 |
| **$In_2O_3$** | Sputtering, PLD, | Sn, Mo, Ti, Nb, Zr | 1 – 3 | 3.7 |
| **CdO** | MOCVD | In, Sn | 0.5 – 20 | 2.4 |
| **β-$Ga_2O_3$** | Sputtering | Si, Sn | $200 – 10^6$ | 4.9 |
| **$Cd_2SnO_4$** | Sputtering, sol-gel, spray pyrolysis | Self-doped | 1.2 – 10 | 3.1 |
| **$Zn_2SnO_4$** | RF sputtering (annealed at 600 ◦C) | Self-doped | 100 – 500 | 3.4 |
| **α-$Zn_2SnO_4$** | RF sputtering (*Ts* 375–430 ◦C) | Self-doped | 30 – 60 | 3.4 |
| **α-$Zn_2SnO_4$** | RF sputtering (*Ts* RT – 300 ◦C) | Self-doped | 40 – 100 | 3.4 |
| **$Zn_2In_2O_5$** | DC or RF sputtering | Self-doped | 2.9 | 2.9 |
| **α-IZO** | DC sputtering | Self-doped | 3 – 5 | 3.1 |
| **$TiO_2$** | Sputtering, PLD | Nb, N | $9 – 10^6$ | 3.2 |

#### 2.3.1.2. Nanoporous Photoanode

Nanoporous photoanode is layer of wide band gap semiconductor material with high surface area. In order to achieve this, a highly porous structure is required. There are several types of semiconductors used for nanoporous photoanodes. Most commons are $TiO_2$, $SnO_2$, ZnO, $Nb_2O_5$, $ZrO_2$, MgO, $CeO_2$, however, best cell and module efficiencies are obtained by using anatase $TiO_2$ as 11.9% and 7.2% respectively [14].

The reasons why anatase $TiO_2$ is desired are that its spherical nanostructure morphology, 3.2 eV band gap value, optimum coherence of conduction band with LUMO (Lowest unoccupied molecular orbit) level of the sensitizer dye. Table 2.4 shows band gap and morphological specifications of both rutile and anatase.

Table 2.4 Energy band properties and morphologies of anatase and rutile [11, 26, 27]

| **Phase** | **Conduction Band** | **Valance Band** | **Energy Band Gap** | **Ionization Potential** | **Morphology** |
|---|---|---|---|---|---|
| **Anatase** | -4.20 | -7.40 | 3.20 | 7.83 | Spherical |
| **Rutile** | -4.00 | -7.03 | 3.03 | 8.30 | Disc-like |

Considering the porous structure of the anatase phase it is important to emphasize that optimum surface are for the sensitizer dye adsorption is necessary to be formed. The total surface are of the porous anatase coating can be extended up to 10000 times more than that of the solid, continuous coating at the porosity levels of 70%. In order to fabricate nanoporous photoanodes of DSSC applications 15 µm of coating thickness is applied with the porosity levels of 50-60 %. The optimum value of the porosity is important for the redox electrolyte to infiltrate into these pores resulting in a structure as shown in fig. 2.7.

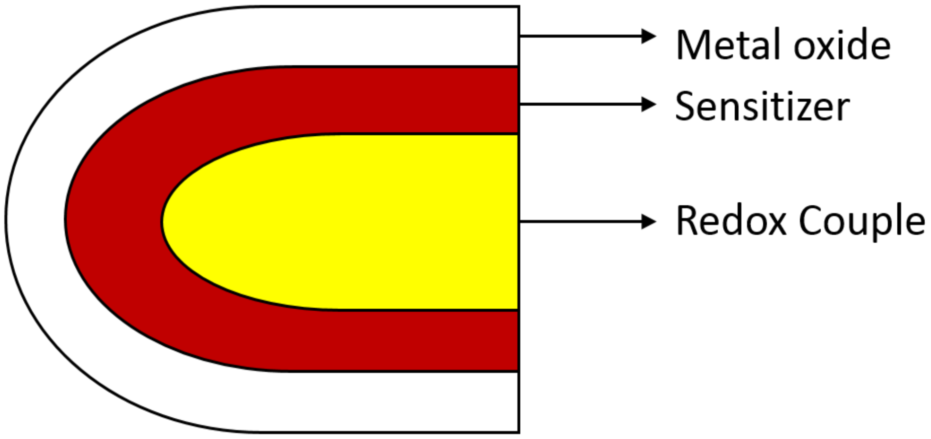

Figure 2.7 Schematic view of the structure inside a pore observed in nanoporous photoanode.

SEM image of a nanoporous anatase coating is shown on fig. 2.8 indicating porous structure with deposited nanoparticles. Nanoporous coatings for DSSC, optimum particle size for anatase is determined as 20 nm such that the energy band gap and Mie Theory conditions are satisfied in order to obtain total transparency for visible spectrum [26, 27].

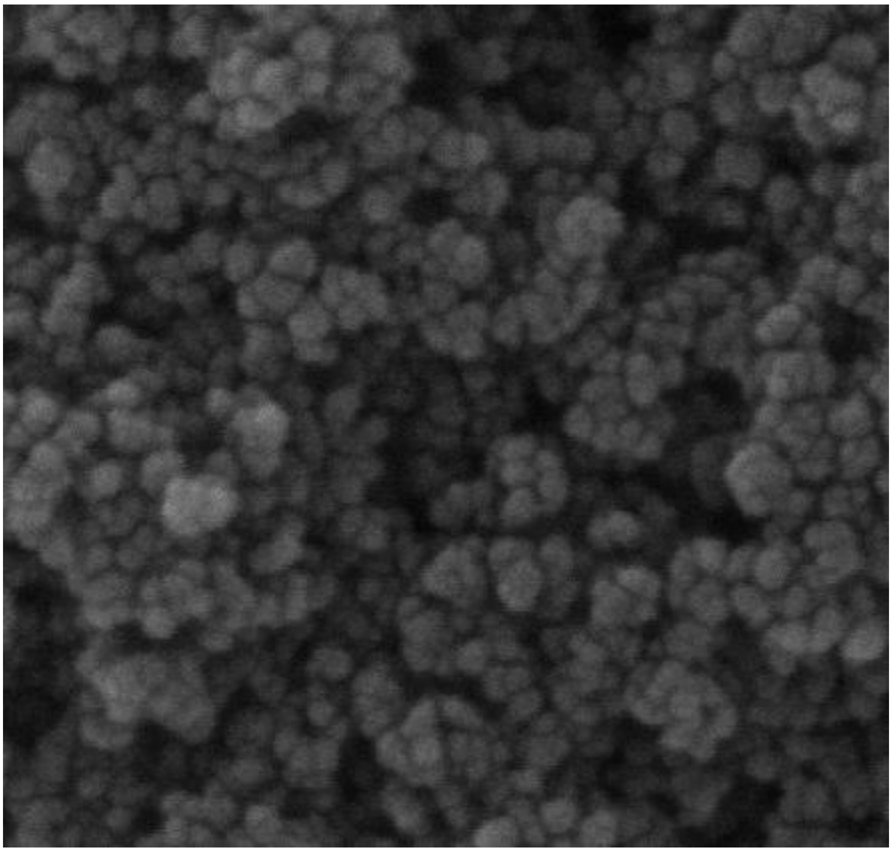

Figure 2.8 Nanoporous Titania ($TiO_2$) Structure [Taken in this study].

Although several applications of ZnO, $TiO_2$ nano rods or nano ribbons are reported in the literature, best cell and module efficiency values are reported for the ones in which anatase nanoparticles are used [32].

#### 2.3.1.3. Sensitizer Dye

Sensitizer dye is the component of DSSCs where the incident photons are absorbed and emission of photoelectrons occurs. By the incidence of light, the electrons are excited from the HOMO (Highest occupied molecular orbit) level to the LUMO level of the sensitizer (photoelectrons), after which the photoelectrons are directly injected to the nanoporous photoanode. Sensitizers are designed and selected in accordance with the solar spectrum intensities such that total absorption of which is expected. Although, the effective wavelength range is 400-800 nm in the solar spectrum, organic sensitizer dyes are modified with metals (Ru, Pt, Os) which is called organometallic dyes, for absorption of the IR range in the spectrum.

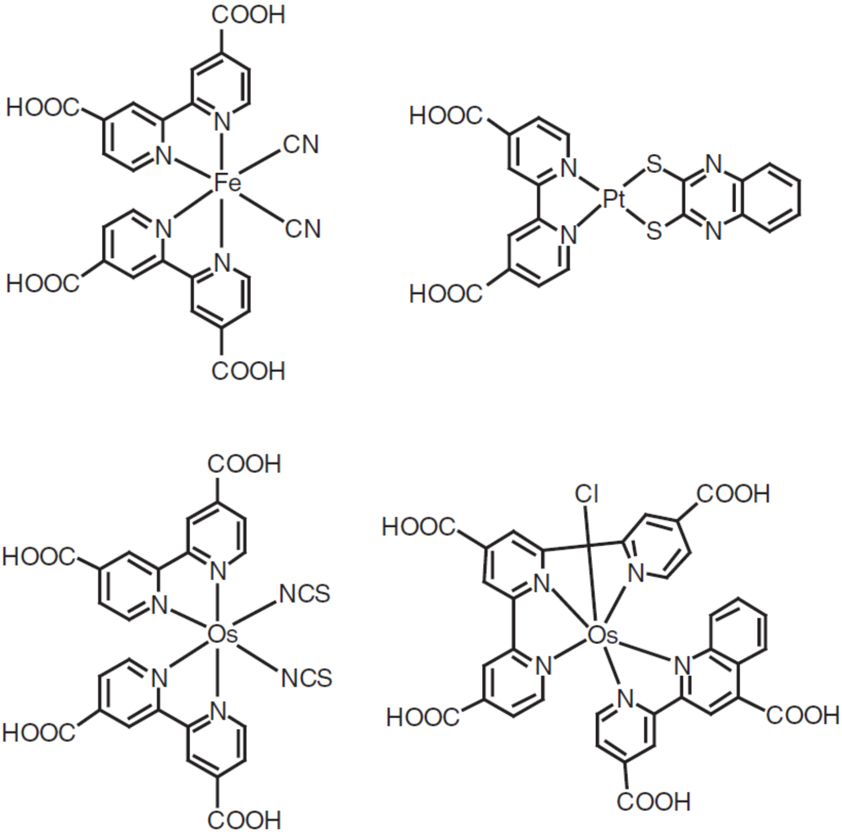

Figure 2.9 Osmium, Platinum and Iron based organometallic sensitizers [28,29,30].

Fig. 2.9 shows the Os, Pt, Fe based organometallic dyes used for DSSC applications. Although, Os based organometallic sensitizers exhibit excellent light absorption range (400 – 1100 nm) with IPCE value of 65%, the coherence of HOMO level – redox Fermi Energy and LUMO level – conduction band of titania is not sufficient enough [46]. The photo response of the Pt and Fe based organometallic sensitizers are limited to 400 – 600 nm and 400 – 700 nm respectively such that the overall absorption of solar spectrum cannot be achieved [28, 29].

**2(N3)**

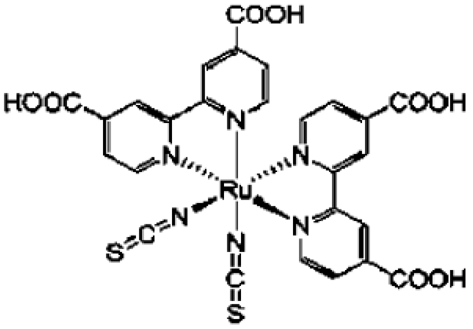

**4(N719)**

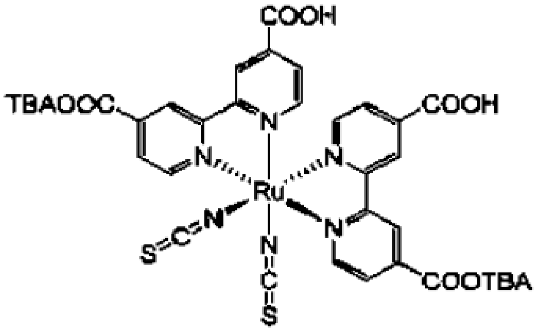

**6(Z907)**

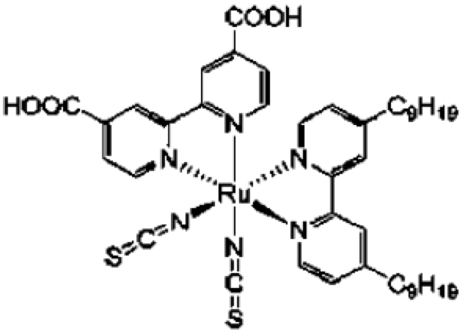

Figure 2.10 Ruthenium based organometallic sensitizers [32].

Ru-based organometallic dyes (Fig. 2.10) are the most preferred sensitizers due to its excellent photo response (400 – 1100 nm), great coherence with conduction band of titania and redox electrolyte. The intermolecular electron transfer rates from sensitizer to electrolyte is between 0.1 – 1 seconds while the reverse process occurs in nanoseconds. This means that Ru-based sensitizers are the most stable organometallic dyes with an extensive oxidative cycle times of $10^7$ – $10^8$ [33, 34].

#### 2.3.1.4. Redox Electrolyte

Redox electrolyte is the hole conductor component of the DSSCs. The holes generated in the HOMO level of the sensitizer dye is directly injected to the redox electrolyte, through which transport is continued towards Pt coated counter electrode. Therefore, Fermi level of the redox electrolyte has to reside at a higher level of HOMO level of the sensitizer dye. Similarly, it is also vital that Fermi level of the electrolyte also reside at a lower level of both LUMO level of the sensitizer dye and the conduction band of the titania. The maximum theoretical open circuit voltage ($V_{OC}$) is determined as the difference in between conduction band level energy of the titania and the Fermi level energy of the redox electrolyte.

The redox electrolyte has very high electrical conductivity and ionic strength such that the transport by migration due to electrical field is negligible. Low viscosity liquid electrolytes are necessary to be introduced to the cell in order to maintain increased diffusion of the ions within. Since the main transport mechanism through the redox electrolyte is the diffusion mechanism, viscous electrolyte are not preferred. Although, there exists quasi solid and gel electrolytes which are highly stable comparing with the liquid redox electrolytes, due to increased viscosity of the gel electrolytes or hole hopping mechanism which are observed for quasi solid electrolytes, result in diffusion resistance and loss in ionic strength [32].

Typically, in DSSC applications iodite/triiodite ($I^-/I_3^-$) liquid redox couple is used. Iodite content is involved to the system by dissolving LiI, NaI, KI (up to 0.5 M) with 0.1 M $I_2$ into acetonitrile, valeronitrile, propionitrile and methoxypropionitrile and/or mixtures of which. The reason of the utilization of compounds of the iodite with Group I A alkali metal is formation of highly ionic salts in order to increase the ionic strength of the media [35].

#### 2.3.1.5. Counter Electrode

Counter electrode is the component where the injected photoelectrons complete the circuit cycle and reinjected to the system. Simultaneously, the oxidized iodite ions which are triiodite, are regenerated by the reinjected photoelectrons at the surface of the counter electrode. During regeneration the triiodite is deoxidized into iodite balancing the iodite/triiodite ratio at its initial state. However, there is a possibility of TCO coating on the substrate to get oxidize since the Fermi level of the TCO coating is higher than the Fermi level of the redox couple which makes the holes to be injected directly into the TCO layer oxidizing it. Therefore, TCO counter electrode is required to be coated with highly stable and noble conductors like Pt, Au or Carbon. The Fermi levels of which lay upon the Fermi level of the redox couple, thus, Pt, Au or Carbon coatings act as a hole blocking layer also [36].

Fabrication of counter electrodes for DSSCs are mainly conducted by coating the TCO substrate with Pt. Since the deoxidation of iodite/triiodite couple takes place at the interface of redox couple and the metal layer, Pt coating morphologies are desired to be formed as particular morphology rather than a solid continuous film in order to increase the regeneration rate by increasing the interaction surface area. Another advantage of utilization of noble and stable materials for the counter electrode coating is that over oxidation of the redox couple is prevented [32].

### 2.3.2. Working Principle

The working principle of the DSSCs is completely different from the conventional p-n junction solar cells as mention in the previous sections. Rather than a charge separation occurring at the interface of a p-type and an n-type semiconductor, the photoelectron and hole generation takes place at the sensitizer dye molecule and metal oxide interface, titania layer acts as an electron transport layer and redox couple acts as a hole transport layer as well. In fig. 2.11 the energy band diagrams and desired electron cycle within the DSSCs is shown.

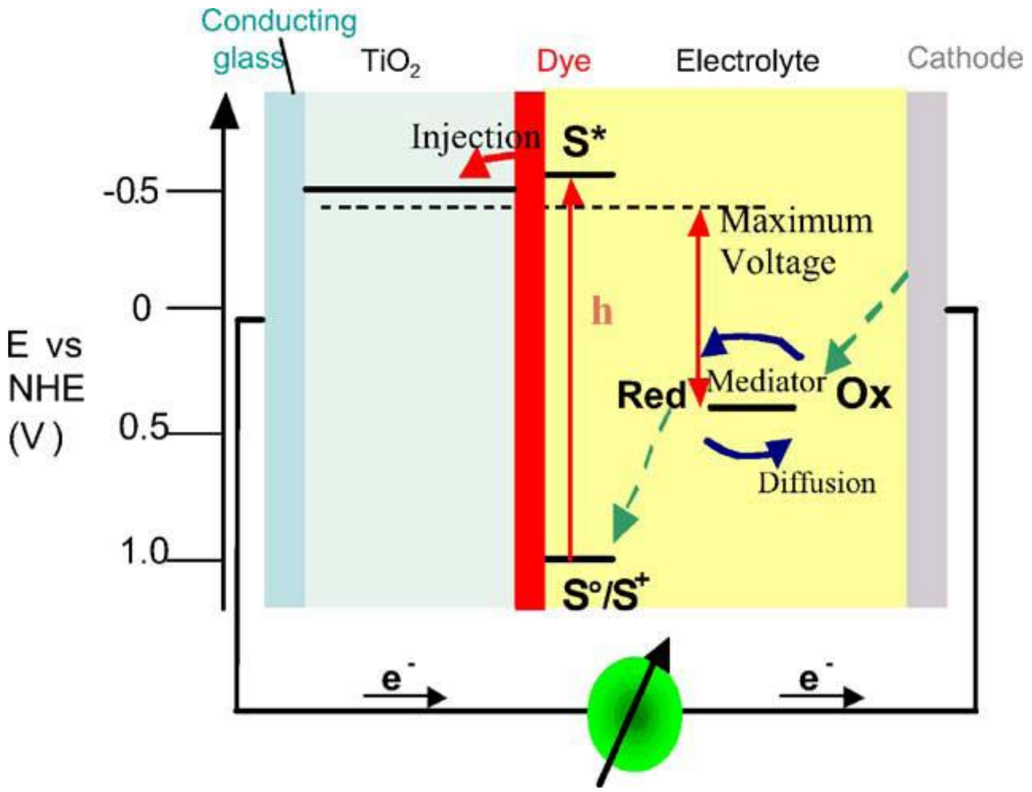

Figure 2.11 Energy band diagram and desired electron cycle within the DSSCs [37].

Upon incidence of photons to the sensitizer dye molecule, the electron is immediately excited form the HOMO level of the dye to the LUMO level. The excited electron (photoelectron) is directly injected to conduction band of the titania (or other high band gap metal oxide semiconductor) nanoporous layer. The metal oxide layer is, in a way, the electron transport layer. Since the dye molecules are adsorbed by the metal oxide surface (chemisorption by hydroxide groups) and the electron injection takes place within picoseconds, it is called “sensitized” metal oxide (titania, etc.) and the process is, as well, called “sensitization”. The electron path continues with transportation through the nanoporous layer and injection into TCO layer of the photoanode. By the contact taken from the TCO layer the electrons are reinjected from the work load into the counter electrode. The reinjected electron is, then, deoxidizes the triiodite into iodite at the Pt coating – redox couple interface. The diffused triiodite ions are regenerated into iodite. The mechanism of deoxidation of the sensitized dye does not work simultaneously with deoxidation of the redox couple. Deoxidation of the dye takes place just nanoseconds after the injection of the photoelectron into the conduction band of the metal oxide layer by oxidizing the redox electrolyte. Therefore, the desired electron path can be considered to complete its cycle with deoxidation of triiodite into iodite at the counter electrode – redox couple interface.

### 2.3.3. Electron Transport Kinetics and Recombination Mechanisms

Unlike p-n junctions solar cells, the electron and hole transport kinetics are different in DSSCs. Rather than a p-n junction interface, the electron – hole pair separation takes place at the metal oxide – sensitizer dye interface. While metal oxide layer acts as an electron transport layer, the redox couple acts as a hole transport layer. The photon absorption and formation photoelectrons takes place within the sensitizer dye according to the Eq. [2.5]. In picoseconds, the photoelectrons in the LUMO level of the sensitizer is directly injected to the conduction band of the metal oxide nanoporous layer (Eq. [2.6]). In the equations below S is the ground state, $S^*$ is the excited state, $S^+$ is the oxidized state of dye and $e_c$ is the photoelectron injected into the conduction band of the metal oxide.

$$S + h\nu \rightarrow S^* \qquad \text{Eq. [2.5]}$$

$$S^* \rightarrow S^+ + e_c \qquad \text{Eq. [2.6]}$$

The electron transportation and electron diffusion concepts for DSSCs cannot be explained with conventional p-n junction solar cell modelling and simulations concepts. Since there is no band edge banding at the interface and its nanoporous structure hinders the conventional measurement and modelling techniques to be applied. Therefore, utilization of electrical impedance spectroscopy (EIS), intensity modulated and transient photovoltage and photocurrent techniques are required. Such measurement techniques depend on the measurement of the small and periodic changes within the cell giving output data as a function of frequency, resistivity, current density and the photovoltage [38].

Considering the fully operating DSSC, the condition which cell is connected to a work load, is called as short circuit conditions. In the equations below R is the reduced component and O is the oxidized component of the redox couple and $e_p$ is the reinjected electron at the counter electrode – redox couple interface.

$$S^+ + R \rightarrow S + O$$

Eq. [2.7]

$$O + e_p \rightarrow R$$

Eq. [2.8]

Transportation of electron depends on the electron transport and electron diffusion concepts simultaneously. The electron transportation starts with the injection of the photoelectron from the LUMO level of the sensitizer into the conduction band of the metal oxide. There exists short circuit conditions as a result of insufficient dye adsorption (dye deficient metal oxide surfaces) and lack of interconnection between the metal oxide nanoparticles as indicated in Eq. [2.9] and Eq. [2.10] respectively.

$$e_c + O \rightarrow R$$

Eq. [2.9]

$$e_c + S^+ \rightarrow S$$

Eq. [2.10]

The short circuit conditions directly affect the IPCE (Incident photon to current conversion efficiency) or quantum efficiency values. IPCE phenomenon is the efficiency of obtained current with the incidence of the photon into the cell. IPCE value is a function of $I_{SC}$ (short circuit current), $P_{in}$ (incident power) and the energy of a single photon.

$$IPCE\% = \frac{I_{SC}(A)}{P(W)} * h\nu * 100$$

Eq. [2.11]

The situation explained by Eq. [2.9] is considered as a recombination mechanism. In DSSCs, the injection of photoelectrons in the conduction band of the metal oxide and transport through which occurs simultaneously with this back recombination. Although, transport rate of photoelectrons in the conduction band is higher than the back recombination rate, this loss mechanism effects obtained photocurrent values, i.e. ICPE. The term of electron diffusion length defined as the root mean square of the diffusion coefficient of the electron ($D_n$) and the electron life time ($\tau_n$), which is the duration of photoelectron without back recombination as indicated on Eq. [2.12].

$$L_n = \sqrt{D_n \tau_n}$$

Eq. [2.12]

The diffusivity and the life time of the photoelectron depends on light intensity, the impurities and the defects within the photoanode. Although, increasing intensity of the light increases the diffusion coefficient of the electrons, the electron life time decreases. This due to the trap levels within in the energy band gap of the metal oxide layer such that the entrapment rate of the photoelectrons increases with the illumination. The reason for the existence of the trap sites is due to impurities in the metal oxide matrix and the extended surface are of the nanoparticles. Since the metal oxide matrix is highly porous with an extreme surface area, the overall surface acts as defects such that metal oxide matrix can be considered as completely defective structure. However, it is possible to overcome the entrapments due to the surface of this matrix with thermal energy [39].

There is also contradictions due to the presence of cations of Li, Na, K within the redox couple the addition which provides ionic strength to the redox couple. As the illumination of the light occurs, the triiodite ions transport towards counter electrode. Simultaneously, due to the electric field the transport of those cations occurs towards the metal oxide matrix. The pile up of the cations at the metal oxide interface, suppresses the effect of electrical field within the matrix, resulting in electro neutralization. Due to the electro neutralization taking place, the electrolyte cannot penetrate through pores of metal oxide matrix with the formation of a Debye length at around 0.1 nm.

Transport of electrons within the metal oxide matrix occurs with the transfer of the electrons amongst the nanoparticles towards the TCO layer. In order to prevent recombination losses, the interconnection of the particles are required to be continuous and well established. As well as the interconnection of the nanoparticles, the electron transport is required to have transfer direction towards the TCO layer such that considering the Random Walk Theory, the possibility of the electrons to move backwards within the metal oxide matrix can be decrease by adjustment of the porosity. In accordance with the porosity level, the possible neighboring among the nanoparticles can be adjusted and defined with the coordination number, similar to lattice systems. Having a porosity level of 70-80 %, results in a coordination number of 2.5-3.0 while 50% porosity results in 5.0. It is observed that increasing porosity decreases the possible neighboring with decreasing backwards transport within the matrix. Electron transport in highly porous metal oxide matrix occurs in longer pathways unless the interconnection of the particles are poor [39].

There are several recombination mechanisms observed in DSSCs. In Fig. 2.12, the possible electron pathways and recombination mechanisms are shown.

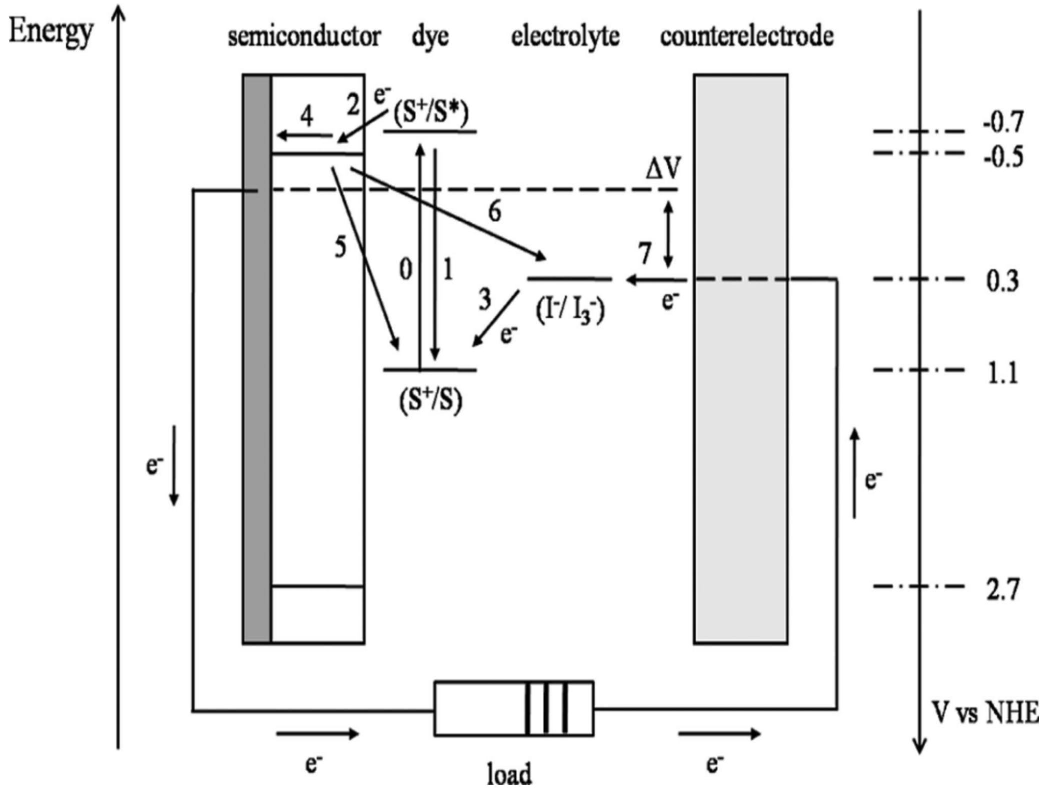

Figure 2.12 Energy Band Diagram of DSSC with possible electron pathways [32].

The desired electron cycle are labelled as:

(0) Excitation of electron form HOMO level to LUMO level of the dye,
(2) Injection photoelectron to the metal oxide conduction band,
(3) Neutralization of dye and oxidation iodite into triiodite,
(4) Transport through metal oxide matrix and injection to TCO layer,
(7) Reinjection of the electron from the counter electrode.

There are three main possible recombination mechanism within the cell:

(1) Recombination of the excited electron back to HOMO level of sensitizer,
(5) Back recombination of the photoelectron from conduction band of metal oxide to HOMO level of sensitizer,
(6) Back recombination of the photoelectron from conduction band of metal oxide to redox electrolyte.

Recombination (1) is observed when the adhesion between the metal oxide and the sensitizer is poor. This type of recombination is observed for Os, Fe, Pt based organometallic, slightly; however, this loss mechanism is almost surpassed with Ru-based organometallics.

Considering the back recombinations of (5), (6), the most severe of which is recombination back to the electrolyte (6). Although the recombination (5) is perceived to be the most possible, due to lower energy band gradient observed for metal oxide conduction band – redox electrolyte Fermi level, the rate of recombination (6) is much higher. In fact, this type of recombination is not necessarily observed for metal oxide – redox electrolyte interface, it is also observed at TCO – redox electrolyte interface [32].

### 2.3.4. Production Method of Nanoporous Photoanodes for Conventional DSSCs

The most popular and well-developed method for production of photoanodes for DSSCs is screen printing via titania paste. As synthesized anatase nanoparticles or commercially available P-25 (Degusa, 80/20 Anatase/Rutile) are dispersed in viscous paste prepared by binders. In order to prepare the titania paste, the nanoparticles are dispersed in a mixture of ethanol, terpienol and ethylcellulose (EC). Preparing 10:90 wt. % ethanol and EC containing 16 g of pure titania nanoparticle in a flask, 64.9 g terpienol is added to the mixture. The mixture is, then, mixed and diluted with 80 ml of ethanol to obtain a 280 ml of final volume. The final mixture is ultranonicated 3 times consequently, then the ethanol is removed from the mixture by a rotary evaporator in order to obtain the screen-printing paste.

The prepared paste is deposited on the FTO/Glass substrates with 90T mesh by screen printing. Each cycle of the deposition yields a coating thickness of 5 μm, thus 3 cycles of coating is conducted. The substrate is heated at 125 $^{o}$C such that each layer is dried before the next one.

The deposited substrates via screen printing, is fired/cured at distinct temperature for different time intervals. Heating profile involves:

- 325 $^{o}$C for 5 min
- 375 $^{o}$C for 5 min
- 450 $^{o}$C for 15 min
- 500 $^{o}$C for 15 min
- Blowing dry air at 500 $^{o}$C for 30 min

Subsequently, the DSSC assemble is completed with dye adsorption, sandwich closure of the counter electrode and electrolyte back filling [6].

### 2.4. Alternative Production Methods of Nanoporous Photoanodes on TCO/Polymer Substrates for "Flexible" DSSCs (FDSC)

In chapter 1, all the alternative production methods for nanoporous photoanodes for FDSCs are mentioned. In table 2.5, the reported production methods for both photoanodes and counter electrodes with their materials and obtained efficiency values for recent years.

Table 2.5 Production methods for photoanodes and counter electrodes and obtained efficiencies (η)

| **Photoanode** | **Counter Electrode** | **Method** | **η (%)** | **Reference** |
|---|---|---|---|---|
| $TiO_2$ (PEN) | Pt Sputtering (PEN) | EPD - Hydraulic Comp. | 4.57 | [40] |
| ZnO nanowire (Ti foil) | Pt Sputtering (PEN) | Doctor-blade | 2.19 | [41] |
| $TiO_2$ (Glass) | Amorphous Carbon and PEDOT-PSS (Metal mesh PEN) | Screen Printing | 5.5 | [42] |
| $TiO_2$ (PEN) | Pt Sputtering (PEN) | Doctor-blade and Hydraulic Comp | 4.92 | [43] |
| $TiO_2$ (PEN) | Pt Sputtering (PEN) | Doctor-blade and CIP | 6.3 | [44] |
| $TiO_2$ (PEN) | Pt Sputtering (PEN) | Doctor-blade and CIP | 4.01 | [45] |
| $TiO_2$ (Ti foil) | Pt Electroplating (PEN) | Screen Printing | 6.53 | [46] |
| $TiO_2$ (PEN) | Pt Sputtering (PEN) | EPD - Hydraulic Comp. | 5.76 | [47] |
| $TiO_2$ (PEN) | Pt Sputtering (PEN) | Doctor-blade and CIP | 2.87 | [48] |
| $TiO_2$ nanotube-nanoparticles (Ti foil) | Pt (GLASS) | Anodization and EPD | 6.28 | [49] |
| $TiO_2$ (GLASS) | Pt Electroless (PEN) | Screen Printing | 4.62 | [50] |
| $TiO_2$ (PEN) | Pt Sputtering (PEN) | EPD - Hydraulic Comp. | 5.25 | [51] |
| $TiO_2$ (Ti foil) | Pt Electroplating (PEN) | Screen Printing | 5.8 | [52] |
| $TiO_2$ (Ti foil) | Pt Sputtering (GLASS) | EPD - Hydraulic Comp. | 6.5 | [53] |
| ZnO (PEN) | Pt Sputtering (GLASS) | EPD - Hydraulic Comp. | 3.36 | [54] |
| $TiO_2$ (Ti Mesh) | Pt Electroplating (Ti Mesh) | Doctor-blade | 6.13 | [55] |
| $TiO_2$ (PEN) | Pt Sputtering (PEN) | EPD | 6.63 | [56] |

Table 2.5 (Continued)

| | | | | |
|---|---|---|---|---|
| $TiO_2$ (PEN) | Pt Sputtering (PEN) | Doctor-blade and CIP | 4.0 | [57] |
| $TiO_2$ nanotube (PEN) | Pt Sputtering (PET) | Ti Sputtering and Anodization | 3.5 | [58] |
| $TiO_2$ (Ti foil) | Pt - CNT (PEN) | Doctor-blade | 5.96 | [59] |
| $TiO_2$ (Ti foil) | Pt (GLASS) | Screen Printing | 6.75 | [60] |
| $TiO_2$ (PET) | Pt Sputtering (GLASS) | Doctor-blade | 3.53 | [61] |
| $TiO_2$ (PEN) | Pt Sputtering (PEN) | Doctor-blade | 3.02 | [62] |
| $TiO_2$ (PEN) | Pt Sputtering (PEN) | Doctor-blade | 4.41 | [63] |
| $TiO_2$ nanotube – nanoparticle (Ti foil) | Pt Sputtering (GLASS) | Anodization | 5.75 | [64] |
| $TiO_2$ (PEN) | Pt Sputtering (PEN) | Doctor-blade and Hydraulic Comp. | 7.6 | [65] |
| ZnO-$SnO_2$ (PEN) | Pt Sputtering (PEN) | Doctor-blade | 4.91 | [66] |
| $TiO_2$-SrO nanotube – nanoparticle (Ti foil) | Pt Sputtering (PEN) | Anodization | 5.39 | [67] |
| $TiO_2$ (Ti foil) | Pt (GLASS) | Doctor-blade | 5.45 | [68] |
| $TiO_2$ (Ti foil) | Pt Reduction (PEN) | Screen Printing | 5.41 | [69] |
| $TiO_2$ (PEN) | Pt (GLASS) | Doctor-blade | 3.39 | [70] |
| $TiO_2$ (PEN) | Pt Sputtering (PEN) | Doctor-blade | 5.0 | [71] |
| $TiO_2$ (PEN) | Pt (GLASS) | Doctor-blade | 3.25 | [72] |
| $TiO_2$ (Ti foil) | Pt (GLASS) | Doctor-blade | 4.77 | [73] |
| $TiO_2$ (Ti foil) | Pt Sputtering (PEN) | Doctor-blade | 5.95 | [74] |
| $TiO_2$ (PEN) | Pt (GLASS) | Doctor-blade | 5.0 | [75] |
| $TiO_2$ (PEN) | Pt (GLASS) | Doctor-blade | 6.31 | [76] |
| $TiO_2$ (Ti foil) | Pt (GLASS) | EPD | 6.33 | [77] |
| $TiO_2$ (PEN) | Pt Sputtering (PEN) | Doctor-blade | 4.2 | [78] |
| $TiO_2$ nanotube (Ti mesh) | Pt Sputtering (PET) | Anodization | 1.23 | [79] |
| $TiO_2$ nanotube (Ti foil) | Pt Sputtering (PEN) | Anodization | 3.6 | [80] |

Table 2.5 (Continued)

| | | | | |
|---|---|---|---|---|
| $TiO_2$ (Steel foil) | Pt Reduction (PET) | Doctor-blade | 8.0 | [81] |
| ZnO (PET) | Pt doctor-blade (PET) | Doctor-blade | 3.8 | [82] |
| $TiO_2$ (Steel foil) | Pt Reduction (PET) | Doctor-blade | 6.1 | [83] |
| $TiO_2$ (Steel foil) | Pt (GLASS) | Doctor-blade | 3.55 | [84] |
| $TiO_2$ (Tungsten foil) | Pt (GLASS) | Doctor-blade | 3.34 | [84] |
| $TiO_2$ (Ti foil) | Pt (GLASS) | Doctor-blade | 3.54 | [84] |
| $TiO_2$ (Ti foil) | Pt Electroplating (PEN) | Screen Printing | 7.2 | [85] |

The production of the flexible photoanodes on polymeric substrates are mainly dominated by “Doctor-blade” method as indicated in table 2.5. Some studies includes secondary processes such as hydraulic compression and cold isostatic pressing (CIP) as a replacement for curing/firing process available for conventional DSSCs. As mentioned in the previous section, it is important to obtain excellent interconnections and neckings among the metal oxide nanoparticles in order to maintain reliable IPCE values and decrease the recombination losses. Therefore, extensive compression levels are to be used in order to provide a sintering effect for metal oxide nanoparticles.

Although, the binders and solvents of the doctor-blade paste is acknowledged to be highly volatile, easily removable, the thickness control of the coating is not sufficient. Due to nanoporous coating structure, during the removal of such binders and solvents the volumetric contraction cannot be estimated clearly. Therefore, an alternative deposition method is necessary by which the control on coating thickness can be achieved.

### 2.4.1. Doctor – Blade Method

Doctor – Blade method is named for applications of slurries on moving plaster batts by a doctor blading device in 1952 [86]. Recently, replacing the doctor blades with a tape frame, doctor – blade technique has been one of the versatile and low cost method for ceramic nanoparticle coating for large areas. In fig. 2.13-14, the motion of the doctor blade frame and its cross-section view is shown.

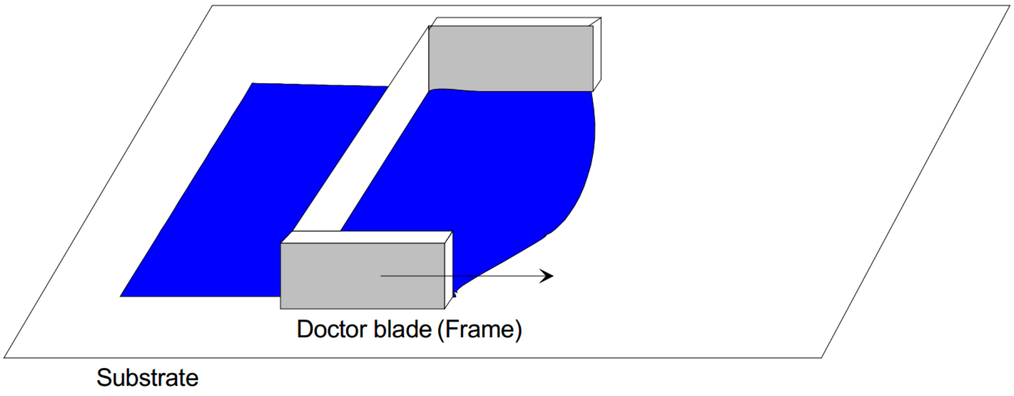

Figure 2.13 Coating mechanism and frame motion [41].

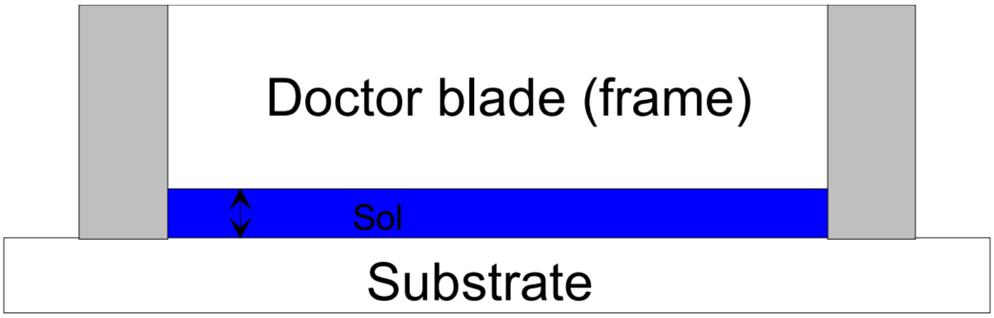

Figure 2.14 Cross-sectional view of doctor – blade frame [87].

In order to deposit the $TiO_2$ nanoparticles onto the substrates via doctor – blade method, it is necessary to prepare a $TiO_2$ paste i.e. a colloidal solution. The paste is prepared via mixing ethanol and tert-butanol 1:2 volume fractions, then adding ~10% wt. of $TiO_2$ nanoparticles. Furthermore, the colloidal solution is subjected to ultrasonication for about 30 min in order to get rid of the agglomerated nanoparticles [44]. Finally, the paste is poured on the doctor blade sol tank and coating is conducted as shown in fig. 2.15.

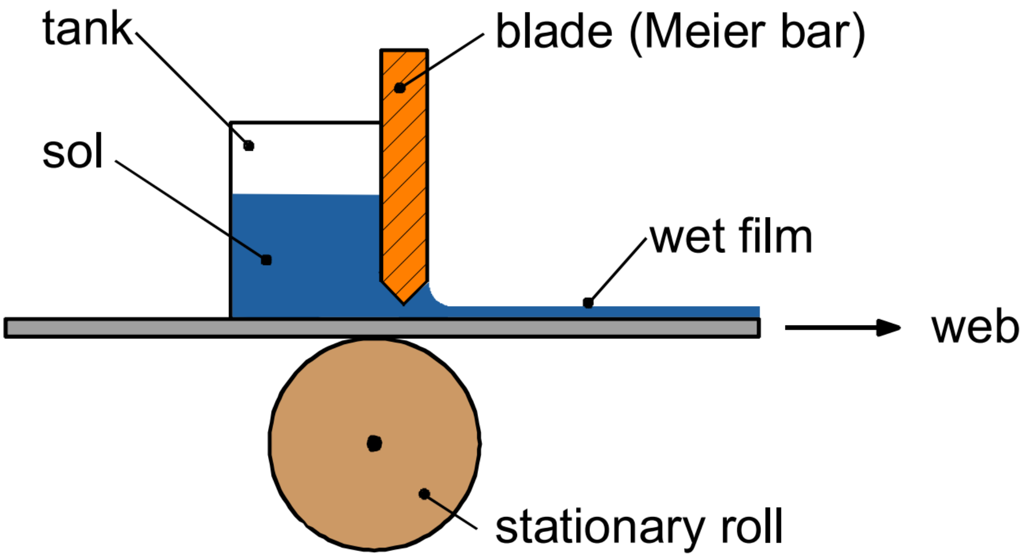

Figure 2.15 Doctor – blade device for roll-to-roll processing on polymeric substrates [88].

### 2.4.2. Electrophoretic Deposition Method (EPD)

Electrophoresis and dielectrophoresis phenomena have been observed on solutions of non-conductive/insulating particles within a media. Early applications of electrophoresis has been conducted on biological materials like protein, lipids and cells in order to isolate and separate them from each other. Electrophoresis is obtained immersion of two parallel electrodes into the colloidal solution. As the application of potential difference proceed, the motion of dielectric particles (dielectrophoresis) takes place towards the corresponding electrode.

EPD method or observation of electrophoresis (dielectrophoresis) is observed and attainable only for dielectric colloids. Upon dispersion of dielectric particles within the solution media, there exists a charge built-up onto the surface of the particles due to the pH gradient between solution media and the surface pH value of the surface of the particle. The pH gradient is denoted as ΔpH and calculated:

$$\Delta pH = pH_{particle} - pH_{media}$$

Eq. [2.13]

For instance, if the ΔpH value is zero, there exist no electrophoretic mobility such that under no applied voltage can transport of the particles occur. Thus, the corresponding pH values is called "Isoelectric point" such that the colloids are idle particles. Additionally, if it is larger than zero, then the particle surface is positively induced such that upon application of a potential difference, the electrophoretic motion of the particles proceed towards the negative electrode. The positive or negative induction is not necessarily to be attained by only the intrinsic pH value of the solution media. In fact, most of the time, the pH value of the solution media is adjusted by addition of polar substances such as acids, bases or some other surfactant agents. Increasing pH gradient will increase the mobility of the particles upon applied voltage which is called electrophoretic mobility ($\mu_{EP}$).

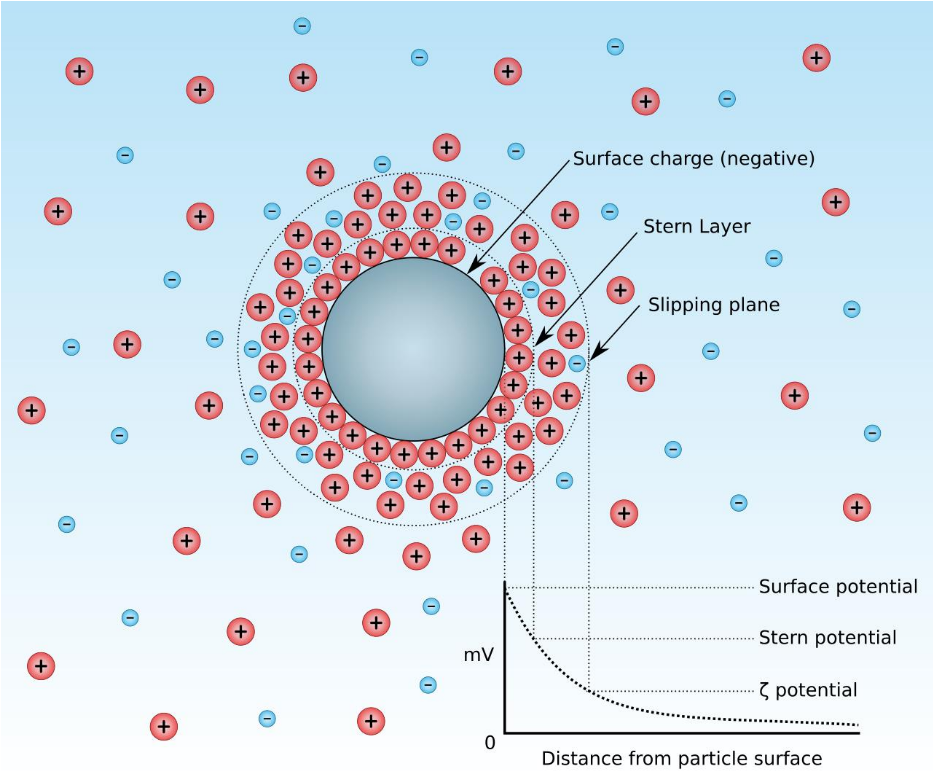

Figure 2.16 Schematic view of a colloid with its induction, Stern layer (Debye length) and Zeta potential [89].

The pH gradient terms indicates the existence of the concentration of the cations over a specific distance from the surface of the particle to the solution media. This distance is denoted as Debye length such that the length values do not exceed a few nm mainly as shown in fig. 2.16. However, considering the electrophoresis of the nanoparticle, the Debye length strongly effects the mean particle size values, resulting in the necessity of the use of “effective particle size”. Additionally, this concepts also leads to a potential difference between particle surface and the solution media along the Debye length which is called “Zeta Potential (ζ)” and calculated as:

$$\zeta = \frac{\mu_{EP}\eta}{\varepsilon_M \varepsilon_0}$$

Eq. [2.14]

where η is the dynamic viscosity and $\varepsilon_M$ is dielectric constant of the solution media and $\varepsilon_0$ is permittivity of free space.

In order to obtain electrophoretic mobility, it is important to apply sufficient electric field between the electrodes. Therefore, in Eq. [2.15], the threshold electric field $E_0$ (V/m) necessary is calculated:

$$E_0 = \frac{kTa^2}{6\pi\varepsilon_M\zeta}$$

Eq. [2.15]

where k is the Boltzmann constant, T is temperature (°K), $a$ is the effective particle size.

Considering the threshold voltage term, one can see the effect of electrode distance by observing the V/m unit. Therefore, it is important to optimize the electrode distance for the EPD applications. Having very short electrode distance will decrease the necessary applied voltage; however, the effective particle concentration will be limited to the amount between the electrodes [90].

Electrophoretic deposition of ceramic particles are mainly conducted by colloidal solution of alcohol based solution with surfactants and ionizing agents like water, acids, bases, acetylacetone, etc. Since the alcohol based liquids are highly dielectric and easily removed from the coated specimens due to its volatile nature, ethanol, methanol and isopropanol and also their mixtures are widely used as solution media. Although these substances have their own ionizing effects ($H^+$ donor), it is not sufficient to conduct low voltage coatings. Therefore, this ionizing effect requires to be supported by external ionizing agents. Additionally, in order to obtain highly homogeneous dispersion of the colloids surfactant agents are necessary to be added.

For EPD applications of the nanoparticle coatings, acetylacetone is the most effective surfactant agent. In fact, utilization of acetylacetone itself is observed to be a solution media for the coatings of YSZ (yttria stabilized zirconia) nanoparticles [91]. In table 2.6, the coatings conducted using EPD methods with specified solvent and materials are listed.

Table 2.6 Solvents used for EPD coatings of several ceramic coatings

| **Material** | **Solvent** | **Reference** |
|---|---|---|
| Alumina / Zirconia | Water | [92, 93, 94,95] |
| YSZ / LaSrGaMgO | Acetone | [96, 97] |
| YSZ | Ethanol – Acetone | [98] |
| YSZ | Acetylacetone | [91, 96] |
| YSZ | Cyclohexane | [96] |
| Hydroxyapatite $YBa_2Cu_3O_7$ | Isopropanol | [99, 100] |
| Alumina / Zirconia | Ethanol | [101] |
| $CeO_2$ / $SnO_2$ / $CaSiO_3$ | Ethanol – Water | [102, 103, 104] |
| MgO / Alumina | Ethanol – Acetylacetone | [105] |
| PZT | Glacial Acetic Acid | [106] |
| β-Alumina | Dichloromethane | [107] |
| Alumina | Methyl ethyl ketone (MEK) | [108] |
| Alumina | Toluene – Ethanol | [108] |

In chapter 3 – Experimental Section, the optimization of the EPD solvent and effects of ionizing agent and acetylacetone addition are investigated.

### 2.4.3. Cold Isostatic Pressing (CIP)

Cold Isostatic Pressing is a robust method for the compression applications. As shown in fig. 2.17, the specimens to be compressed are covered with flexible molding materials like rubber, polyethylene or latex and placed into the pressure chamber.

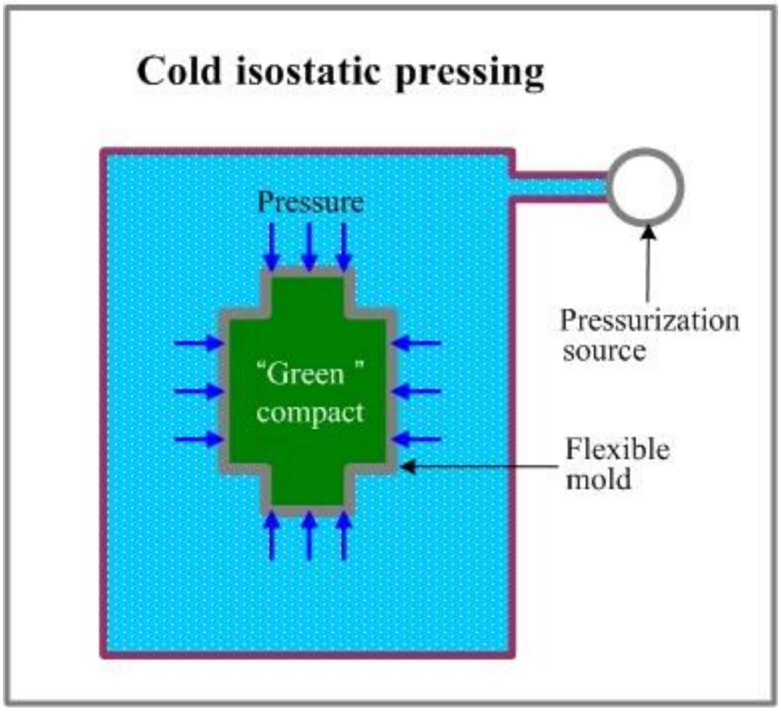

Figure 2.17 Schematic view of cold isostatic pressing chamber [109].

The applied compression is hydrostatic pressure such that compression is conducted homogeneously in 3-D. Therefore, CIP method is the most suitable compression method for hydraulic compression due to such homogeneity in pressurizing.

# CHAPTER 3

# EXPERIMENTAL PART

In this work, in order to fabricate “flexible” dye sensitized solar cells, electrophoretic deposition (EPD) and cold isostatic pressing (CIP) methods are optimized. Starting with the characterization of the commercially available P-25 (Degusa) $TiO_2$ nanoparticles in order to determine the anatase: rutile wt. ratio, the EPD solution optimizations and pressure level profiles are investigated. Since the most challenging part of this work is the deposition of the $TiO_2$ nanoparticles as thick film, the majority of the optimizations are focused on EPD process. This chapter mainly focuses on:

- Thick Film Deposition and Formation
    - Electrophoretic Deposition
    - Primary Characterizations
    - Secondary Characterizations
    - Cold Isostatic Pressing
    - Tertiary Characterizations
- Assemblage of FDSC
    - Final Characterizations (Solar Simulator)

## 3.1. Materials

P-25 (Degussa AG, Germany), absolute anhydrous ethanol (Sigma-Aldrich), anhydrous isopropanol (Sigma-Aldrich), acetylacetone (Merck) were purchased in order to prepare EPD colloidal solution. 4-tert-butylpyridine (Merck), Valeronitrile (Alfa Aesar), guanidinium thiocyanate (Merck), 1-butyl-3-methyl imidazolium iodite (BMII) (Merck), Iodine 99.999% (Aldrich), LiI 99.999% (Aldrich) are purchased and used as received for liquid electrolyte. As a sensitizer cis-diisothiocyanato-bis(2,2’-bipyridyl-4,4’-dicarboxylato) ruthenium (II) bis(tetrabutylammonium) or commonly known as N719 dye was purchased from Solaronix.

Indium tin oxide (ITO) coated PEN substrates (~15Ω/□, Peccell Technologies, Inc., Japan) were washed with mild soap, rinsed with deionized water, ethanol and isopropanol 3 times and dried with nitrogen.

## 3.2. Thick Film Deposition and Formation

### 3.2.1. Preparation of Colloidal Solutions

As mentioned in the section 2.4.2, the solution media for EPD is required to be selected and optimized. Considering the most common solvents of methanol, ethanol, isopropanol, water (also as ionizing agent) and acetylacetone (also as surfactant), the colloidal solution stabilities and coating performances are investigated. In table 3.1, the prepared colloidal solution with involving solvents, surfactants, ionizing agents are listed.

The colloidal solutions are prepared by mixing 0.5 gr of P-25 titania nanoparticles with the solvents, surfactants and ionizing agents and their mixture by balancing to 100 mL of solutions. All the solutions are mixed by magnetic stirrer for 72 h with ultrasonic probe homogenization applied 90 min for every 24 h interval. Addition of surfactants are limited to the amounts of 2 – 3 mL while the amounts of ionizing agents added are determined to adjust the pH values given in table 3.1. The ultrasonic probe homogenization is applied at 20 kHz, 70 W conditions such that the values are optimized for best performing homogenization and prevention of overheating of the solutions.

Table 3.1 Prepared solutions and specifications

| # | Solvent | Ratio | Surfactant | Ionizing Agent | pH |
|---|---|---|---|---|---|
| **1** | Ethanol | - | - | - | 4.0 |
| **2** | Ethanol | - | - | Acetic Acid | 3.0 |
| **3** | Ethanol | | Acetylacetone | Acetic Acid | 3.0 |
| **4** | Ethanol | - | | Water | 5.2 |
| **5** | Ethanol | - | Acetylacetone | Water | 5.2 |
| **6** | Pure Water | - | - | Nitric Acid | 3.0 |
| **7** | Methanol | - | - | - | 3.7 |
| **8** | Methanol | - | - | Acetic Acid | 3.0 |
| **9** | Methanol | - | Acetylacetone | Acetic Acid | 3.0 |
| **10** | Methanol | - | - | Water | 5.2 |
| **11** | Methanol | - | Acetylacetone | Water | 5.2 |
| **12** | Methanol / Ethanol | 1 / 1 | Acetylacetone | Acetic Acid | 3.0 |
| **13** | Ethanol / Pure Water | 1 / 1 | Acetylacetone | Acetic Acid | 3.0 |
| **14** | Isopropanol | - | - | - | 4.0 |
| **15** | Isopropanol | - | - | Nitric Acid | 3.0 |
| **16** | Isopropanol | - | Acetylacetone | Nitric Acid | 3.0 |
| **17** | Isopropanol | - | - | Water | 5.3 |
| **18** | Isopropanol | - | Acetylacetone | Water | 5.3 |
| **19** | Methanol / Ethanol / Isopropanol | 1 / 1 / 1 | Acetylacetone | Acetic Acid | - |
| **20** | Ethanol | - | - | $NH_4OH$ | 5.2 |

Figure 3.1 SONOPULS Ultrasonic Probe Homogenizer.

### 3.2.2. Primary Characterizations

Solution stabilities and the electrophoretic properties have been investigated using MALVERN Nano ZS90 for zeta potential measurements and MALVERN Mastersizer 2000 for effective particles size measurements as shown in fig. 3.2.

Figure 3.2 Integrated MALVERN Nano ZS90 and MALVERN Mastersizer 2000 (METU, Central Lab.).

Although, the effective particle size is influenced by the Debye length due to surface charging, in real case scenario, the particle agglomeration within the solution is inevitable. It is almost impossible to obtain completely dispersed particles as single colloids, therefore, effective particle size values are mean agglomerates size values as measured.

### 3.2.3. Electrophoretic Deposition

Electrophoretic deposition has been conducted using YOKOGAWA GS-610 source measure unit with altering applied DC potential values for given solutions. The average surface pH value of the P-25 titania nanoparticles is 6.0; therefore, all the particles in the prepared solutions are positively induced, resulting in the coating of the negative electrode as shown in fig. 3.3.

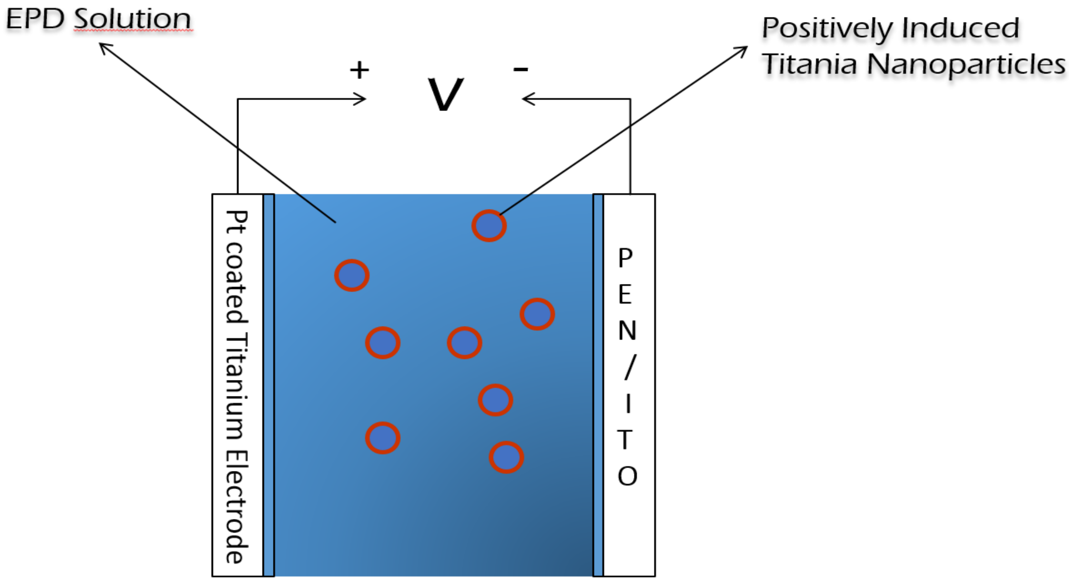

Figure 3.3 Schematic view of EPD setup.

As shown in fig. 3.3, the negative electrode is ITO coated PEN substrate while the counter electrode is Pt coated titanium sheet. The effective coating surface are is set to 1 $cm^2$ while the counter electrode surface area is adjusted to 4 $cm^2$ with an electrode distance of 1 cm. In fig. 3.4, the EPD setup is demonstrated with on-going coating process.

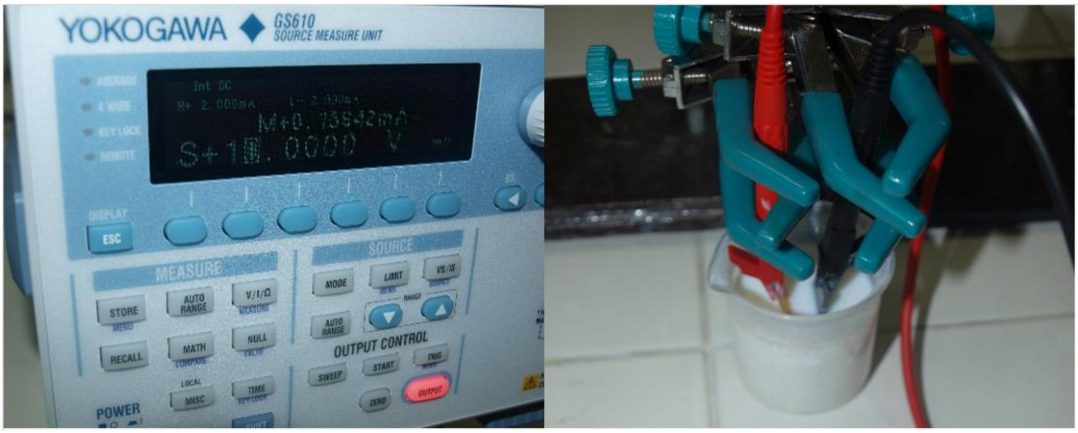

Figure 3.4 YOKOGAWA GS-610 Source Measure Unit and EPD setup.

### 3.2.4. Secondary Characterizations

After the primary characterizations of the solutions, the coatings conducted with the best performing and promising solutions. In accordance with the desired 15 µm of coatings, the coating thickness and morphologies are investigated using scanning electron microscopy (FEI 430 NanoSEM) in Metallurgical and Materials Engineering Department of METU. Additionally, the current vs time data of the candidate solutions are in-situ collected, plotted and investigated. XRD analysis is conducted using Rigaku D/MAX 2200/PC X-Ray diffractometer in Metallurgical and Materials Engineering Department of METU in order to observe the efficiency of the selective anatase coating such that anatase and rutile content of the coatings are investigated, qualitatively.

### 3.2.5. Cold Isostatic Pressing

The coated specimens are covered polyethylene and latex vacuum bags, then vacuum sealing is conducted using vacuum pump and heating sealer. In fig. 3.5, the schematic view of the cold isostatic pressing steps are shown.

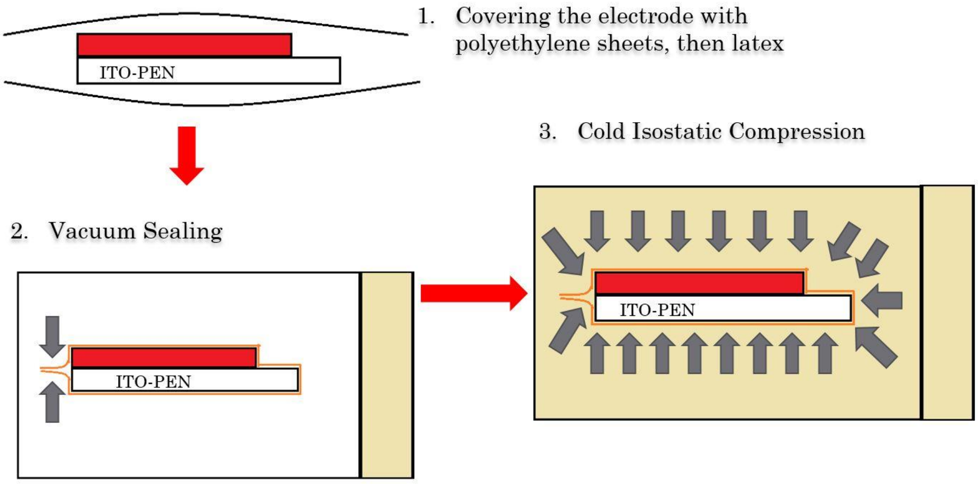

Figure 3.5 Steps of Cold Isostatic Pressing.

The coatings are compressed using Flow AutoClave Engineers CIP 42260 in TUBITAK SAGE, Ankara as shown in fig. 3.6. The compression liquid media is replaced with a mixture of boric acid, water and isopropanol in order to decrease the possibility of the covering vacuum bags to be subjected to excessive friction during compression.

Figure 3.6 Flow AutoClave Engineers CIP 42260.

The compression of specimens were conducted at three distinct compression levels of 150 MPa, 225 MPa and 300 MPa with an effective compression duration of 600 s. In fig. 3.7, the alternating compression profile is shown.

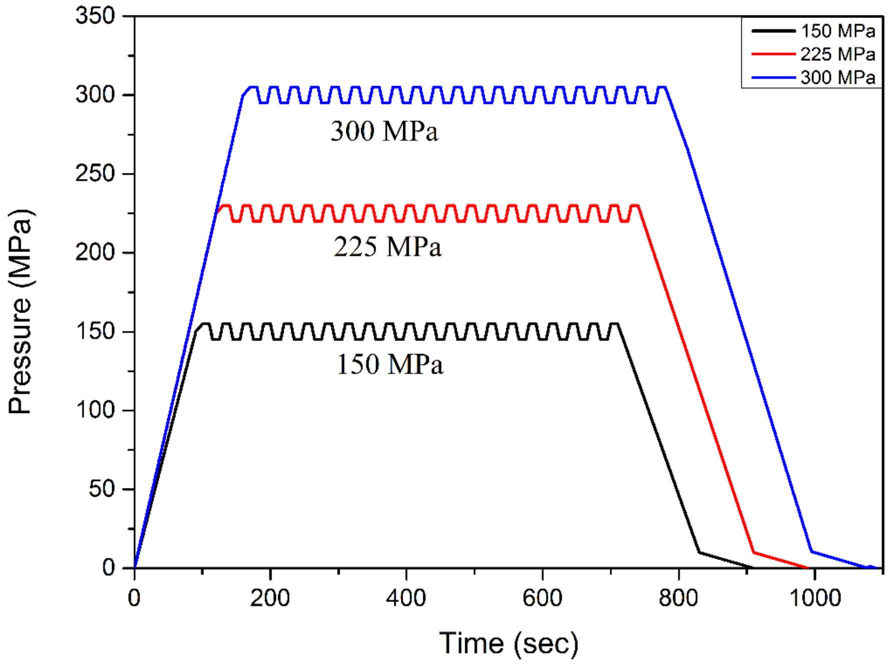

Figure 3.7 Alternating compression profile with given pressure levels.

The reason of the alternating pressure plateau is due to the prevention of the possible bulging of the polymeric substrates and back bouncing of the nanoparticles. The alternating clamping effect is expected to increase the confinement of the nanoparticles among each other such that a further enhancement of the surface roughness of the coatings can be achieved.

### 3.2.6. Final Characterizations

The final structure of the fabricated nanoporous photoanodes have been investigated using scanning electron microscopy. The coating microstructure of the morphology and the nanoporous structure was inspected in order to observe the continuity and the homogeneity of the coatings. Additionally, the final coating thickness values are measured using optical profilometer in GÜNAM, METU.

## 3.3. Assemblage of FDSCs

### 3.3.1. Preparation of Dye Solution and Adsorption

The sensitizer dye solution was prepared by dissolution of N719 Ru-based organometallic dye in the mixture of ethanol, acetonitrile, tert-butyl alcohol 50:25:25. The final concentration of the dye in the solution adjusted to 0.3 mM. The dye adsorption is conducted within an enclosed, opaque beaker for 72 hr. The dye adsorbed photoanodes, then soaked and rinsed with ethanol 3 times in order to remove the excess solvent and dye molecules.

### 3.3.2. Preparation of Redox Electrolyte

Although, gel or quasi-solid electrolytes which are mentioned in section 2.3.1.4 are much more suitable for the fabrication of flexible dye sensitized solar cells. However, in this study, the main focus is on production of flexible photoanodes, enhancement of their performances. It is also indicated that gel and quasi-solid electrolytes yield lower efficiencies due to lack of diffusivities of redox couples than the liquid electrolytes. Therefore, it is vital to eliminate the redox couple parameters in order to compare the performances of the flexible photoanodes with the conventional ones.

The liquid electrolyte is used in the cells are composed of 1 M DMII (Imidazolium Iodide Salt), 0.03 M $I_2$, 0.1 M guanidinium thiocyanate and 0.5 M 4-tert-butylpyridine and 0.05 M LiI in a mixture of acetonitrile and valeronitrile (80:20 volume ratio) is injected in the cell by vacuum backfilling through a drilled hole in the Pt coated counter electrode.

### 3.3.3. Preparation of Counter Electrode

The counter electrodes are prepared by using sputtering form Pt target. The ITO/PEN substrate were initially drilled for electrolyte injection and then coated with Pt at 1.5 kV applied voltage with a coating thickness of 50 nm.

### 3.3.4. Assembly and Characterization

The sensitizer dye adsorbed flexible nanoporous photoanode and the Pt coated flexible counter electrode was assembled by sandwich closure using Surlyn tape (20 µm thickness as a sealant) on a pre-heated table at 100 °C. Injecting the redox electrolyte from the drilled hole at the counter electrode final sealing is conducted using Surlyn tape and PEN as shown in fig. 3.8.

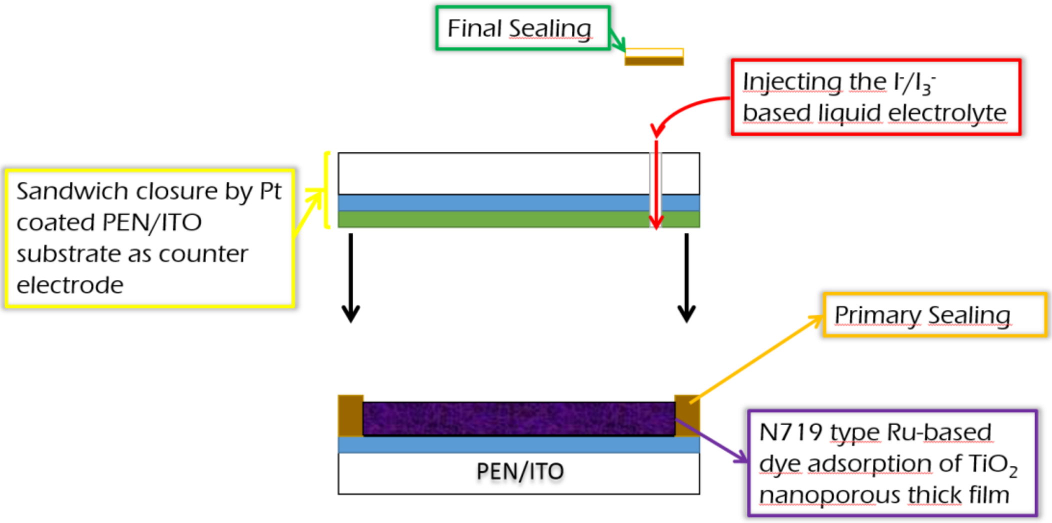

Figure 3.8 Assemblage of flexible dye sensitized solar cells.

The effective photovoltaic surface area of the cells were set to 1x1 cm. Considering this, the solar measurements have been conducted using Keithley 2440 source meter under AM 1.5 conditions with filtered irradiation by using 300W Solar Simulator, Newport 91192. Finally, the I-V characteristics and the IPCE performances of the cells were investigated.

# CHAPTER 4

# RESULTS AND DISCUSSION

In this study, the fabrication of highly pure and stable flexible photoanodes on flexible polymeric substrates is the key to the production and development of flexible dye sensitized solar cells. In order to enhance the properties of the cells, it is important to fabricate fully anatase (rutile-free) photoanodes with highly homogeneous film thickness and nanoporous structure. Since the commercially available titania nanoparticles contain 80% anatase and 20% rutile, the existence of rutile in the nanoporous structure will definitely deteriorate the efficiency and IPCE performance of the cell. Therefore, it is vital to optimize the colloidal solutions for EPD process such that the deposition of the rutile particles are required to be eliminated while obtaining a highly homogeneous nanoporous thick film coating.

## 4.1. Stability and Selective Performances of the EPD Colloidal Solutions

As indicated in table 3.1, the specifications of the solutions in terms of surfactant, ionizing agent additions and the attained pH values are tabulated. The mean isoelectric point of rutile is at around 5.2-5.3 pH value while that of anatase is at around 6.3 [12]. Considering the isoelectric points, in order to keep the rutile particles idle while electrophoretic mobility of anatase particles to be maintained, the pH value of the colloidal solutions are required to be adjusted to pH 5.2-5.3. In table 4.1, the colloidal solutions pH value of which are unable to be adjusted the corresponding pH value are denoted as “Fail”. Since the intrinsic pH values of the all the solvents are lower than the corresponding pH value, it is impossible to attain pH 5.2-5.3 by using acids. Although, utilization of bases as ionizing agents seem to be possible, majority of which contains metal cations when dissolved in solutions. These metal cations like $Na^+$, $Mg^+$ etc. (from hydroxides) results in an inevitable contamination of the films decreasing the dye loading of the nanoporous photoanodes. Addition of $NH_4OH$ into alcohol based colloidal solutions, labelled as “unstable” in table 4.1, the dispersion of the colloids was not able to be maintained more than a few minutes. Such an addition increased the vaporization rate of the colloidal solutions to extensive levels such that the precipitation of the colloids was inevitable.

Table 4.1 Prepared colloidal solutions and observation on selective coating, stability and electrophoresis

| **#** | **Solvent** | **Ratio** | **Surfactant** | **Ionizing Agent** | **pH** | **Result** |
|---|---|---|---|---|---|---|
| **1** | Ethanol | - | - | - | 4.0 | Fail |
| **2** | Ethanol | - | - | Acetic Acid | 3.0 | Fail |
| **3** | Ethanol |  | Acetylacetone | Acetic Acid | 3.0 | Fail |
| **4** | Ethanol | - |  | Water | 5.2 | Possible |
| **5** | Ethanol | - | Acetylacetone | Water | 5.2 | Possible |
| **6** | Pure Water | - | - | Nitric Acid | 3.0 | Hydrolysis |
| **7** | Methanol | - | - | - | 3.7 | Unstable |
| **8** | Methanol | - | - | Acetic Acid | 3.0 | Unstable |
| **9** | Methanol | - | Acetylacetone | Acetic Acid | 3.0 | Unstable |
| **10** | Methanol | - | - | Water | 5.2 | Unstable |
| **11** | Methanol | - | Acetylacetone | Water | 5.2 | Unstable |
| **12** | Met/Et | 1 / 1 | Acetylacetone | Acetic Acid | 3.0 | Unstable |
| **13** | Et/Pure Water | 1 / 1 | Acetylacetone | Acetic Acid | 3.0 | Hydrolysis |
| **14** | Isopropanol | - | - | - | 4.0 | Fail |
| **15** | Isopropanol | - | - | Nitric Acid | 3.0 | Fail |
| **16** | Isopropanol | - | Acetylacetone | Nitric Acid | 3.0 | Fail |
| **17** | Isopropanol | - | - | Water | 5.3 | Possible |
| **18** | Isopropanol | - | Acetylacetone | Water | 5.3 | Possible |
| **19** | Met/Et/Isop | 1 / 1 / 1 | Acetylacetone | Acetic Acid | - | Unstable |
| **20** | Ethanol | - | - | $NH_4OH$ | 5.2 | Unstable |

In table 4.1 the prepared colloidal solutions are classified as their selective coating properties, stabilities and electrophoresis or hydrolysis. The solutions labelled as “Fail” indicates the impossibility of the selective coating property such that the pH values was not able to be adjusted at around 5.2 – 5.3.

Considering the stabilities of the solutions, the ones labelled as “Unstable” indicates the lack of stability. All the methanol based solutions are observed to be unstable. There exists two reasons resulting in such instability:

- Methanol is highly volatile, leading to intoxication for human health and excessive colloid precipitation due to evaporation of Solution media.

- The alcohol based mixtures containing methanol are subjected to the breakdown of dielectric properties. In accordance with the Eq. [4.1] and [4.2], the methanol addition leads to dynamic ionizations and deionizations of the other alcohol based solvents.

$$CH_3OH + C_2H_5O^- + H^+ \leftrightarrow CH_3O^- + C_2H_5OH$$

Eq. [4.1]

$$CH_3OH + C_3H_7O^- + H^+ \leftrightarrow CH_3O^- + C_3H_7OH$$

Eq. [4.2]

The dynamic de/ionizations occurring within such mixtures of methanol with ethanol and isopropanol prevents a reliable measurement of pH such that upon application of a potential difference rather than a coating, the formation of $H_2$ gases observed. Therefore, mixture with methanol are eliminated and labeled as “Unstable”.
Utilization of deionized water and the mixtures of which with other alcohol based substances are observed to result in hydrolysis rather than coatings such that addition of ionizing agents prohibits an additional electrolysis reactions of decomposition of

acids. Hence, utilization of deionized water as solvent is impossible for EPD applications.

Considering the selective coating properties, stabilities and the suitability for EPD applications, 4 out 20 candidate solutions are labelled as “Possible” in table 4.2:

Table 4.2 Candidate EPD colloidal solutions with contents and pH values

| Code | Solvent | Surfactant | Ionizing Agent | pH |
|---|---|---|---|---|
| **ET** | Ethanol | - | DI Water (2 – 3 mL) | 5.2 |
| **EA** | Ethanol | Acetylacetone (~1mL) | DI Water (2 – 3 mL) | 5.2 |
| **IT** | Isopropanol | - | DI Water (2 – 3 mL) | 5.3 |
| **IA** | Isopropanol | Acetylacetone (~1mL) | DI Water (2 – 3 mL) | 5.3 |

## 4.2. Zeta Potential and Particle Size Analysis of Stable EPD Colloidal Solutions

Investigation of electrophoretic performances of the stable EPD colloidal solutions are conducted by measurements of zeta potential values and mean particle sizes. As mentioned in section 3.2.2, the mean particle size is the mean agglomerate size of the colloids dispersed in the solution. Also the viscosities of the colloidal solutions are measured to be almost identical at the value of 0.3 cP.

In fig.4.1-4, the zeta potentials measurements of the four candidate stable colloidal solutions are shown. In general, comparing the number of ionized particles (comparing the total counts) the ethanol based solutions are observed to exhibit more extended amounts of electrophoretically mobile particles than the isopropanol based. It is also observed that the addition of acetylacetone addition in both type of solutions led to a remarkable increase in the amount of electrophoretically mobile particles.

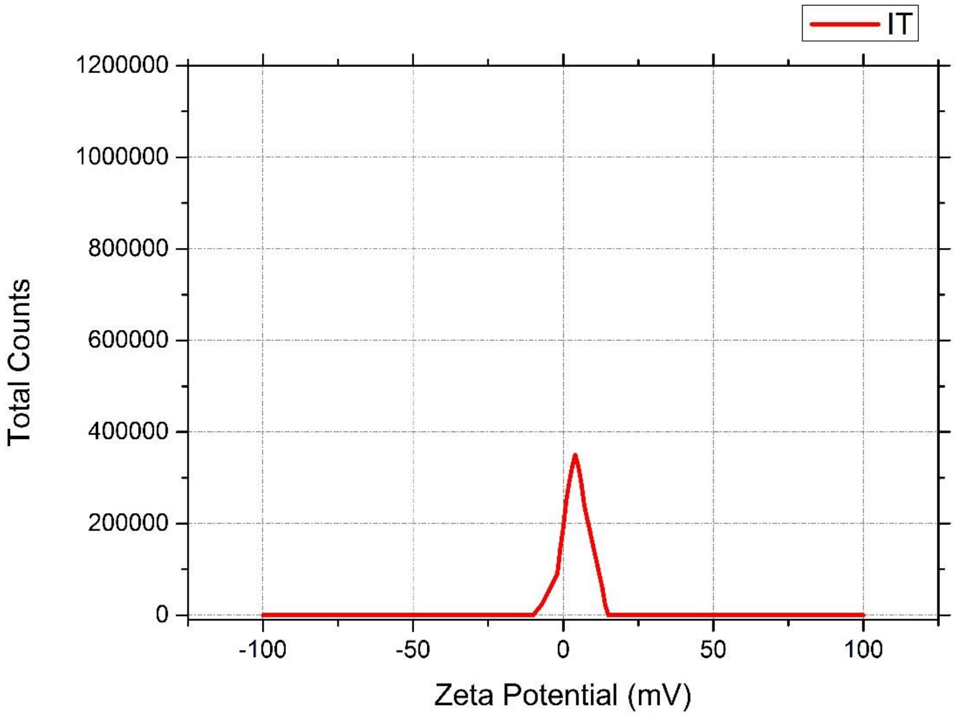

Figure 4.1 Zeta potential measurement of isopropanol based colloidal solution.

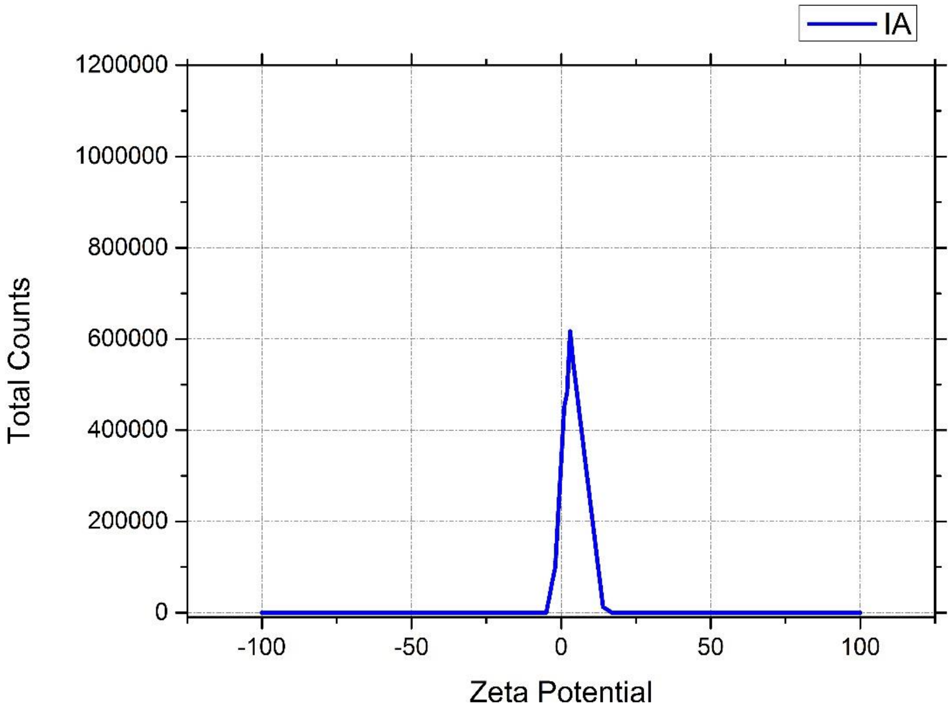

Figure 4.2 Zeta potential measurement of isopropanol based colloidal solution with acetylacetone addition.

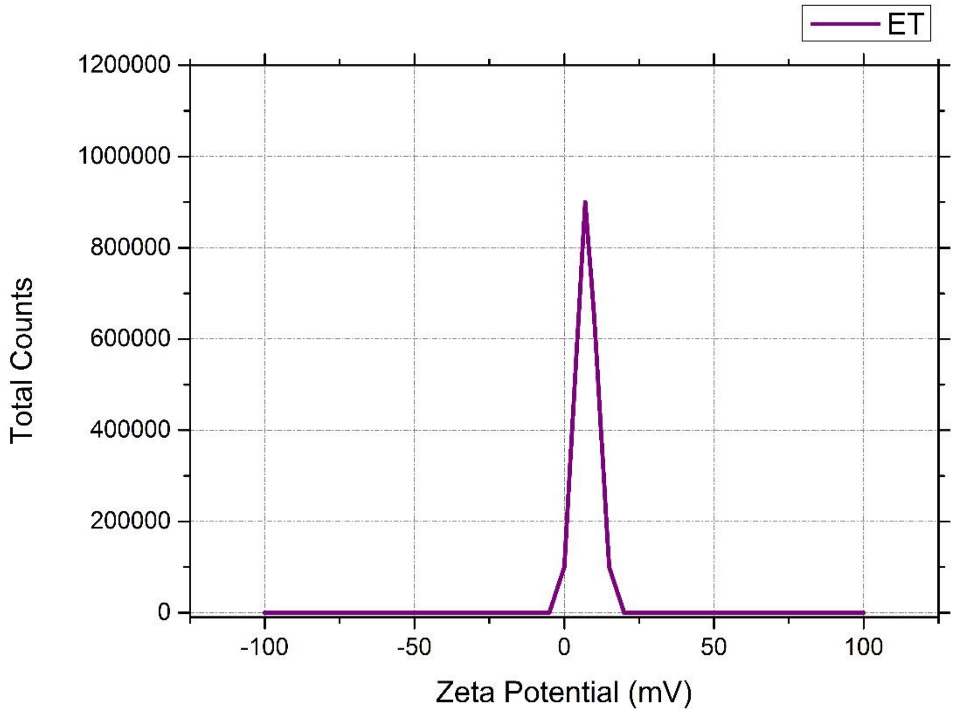

Figure 4.3 Zeta potential measurement of ethanol based colloidal solution.

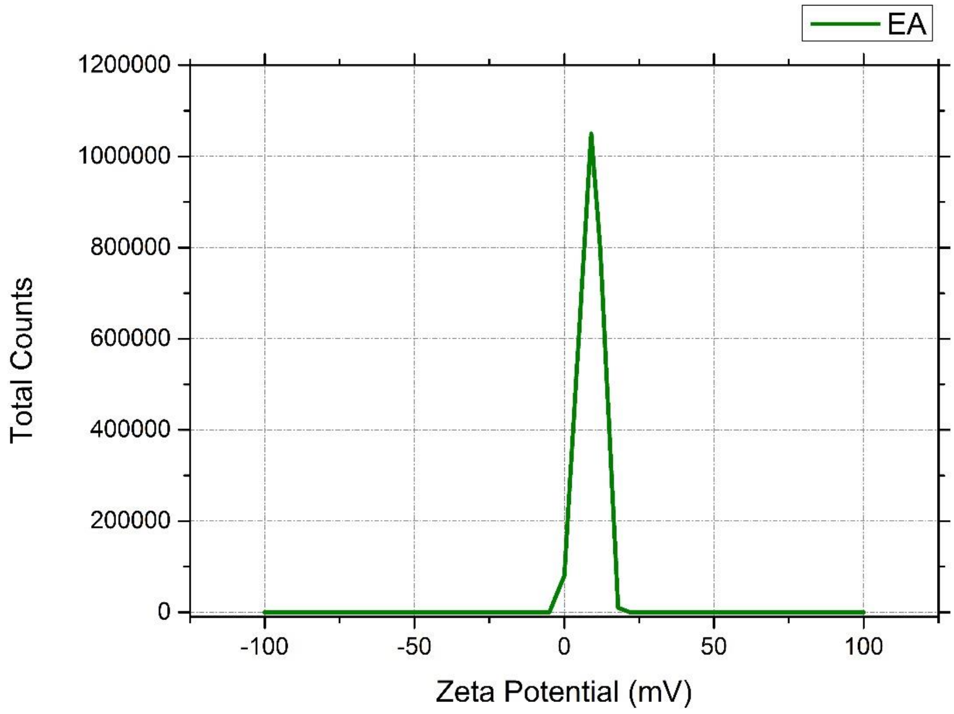

Figure 4.4 Zeta potential measurement of ethanol based colloidal solution with acetylacetone addition.

The mean agglomerate size distribution of the four stable colloidal solutions are plotted on fig. 4.5. It is observed that the mean particles size distribution is homogenized for both type of the solutions with the addition of acetylacetone.

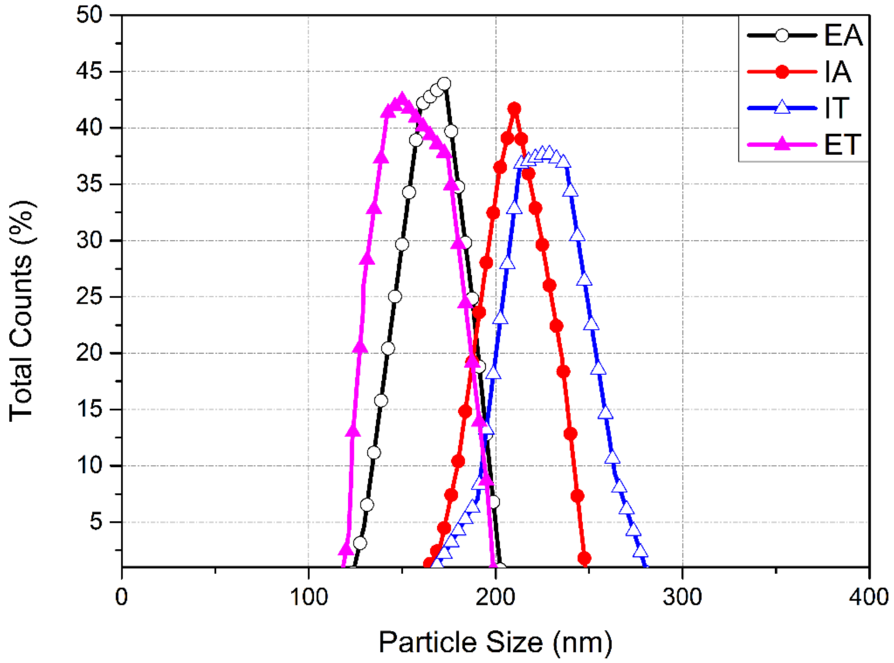

Figure 4.5 Particle size distributions of the four stable colloidal solutions.

Addition of acetylacetone in isopropanol based solution increased the homogeneity of the particles sizes as well as an increase in the zeta potential values. However, investigating the effect of acetylacetone addition to the ethanol based solution the situation is in conflict. Although, there exists a homogenization in the particle size distribution, the mean particle size is increased in acetylacetone added solution as well as the zeta potential. In table 4.3, the overall results of the measurements are tabulated, indicating the changes with the addition of acetylacetone to the both types of colloidal solutions.

Table 4.3 Overall results of zeta potential and mean particle size measurements

| Colloidal Solution | Zeta Potential (mV) | Mean Particle Size (nm) |
|---|---|---|
| IT | 4.02 | 241.7 |
| IA | 4.30 | 207.3 |
| ET | 7.06 | 150.6 |
| EA | 8.88 | 161.4 |

There are two possibilities that result in such a contradiction in between the increase in both zeta potential and mean particle size values of the ethanol based solution by the addition of acetylacetone. The first possibility is that there exists a minimum value of particle size of which the dispersion effect of acetylacetone is limited to. In fig.4.6, this possibility is modelled in order to demonstrate the effect on sub-micron level.

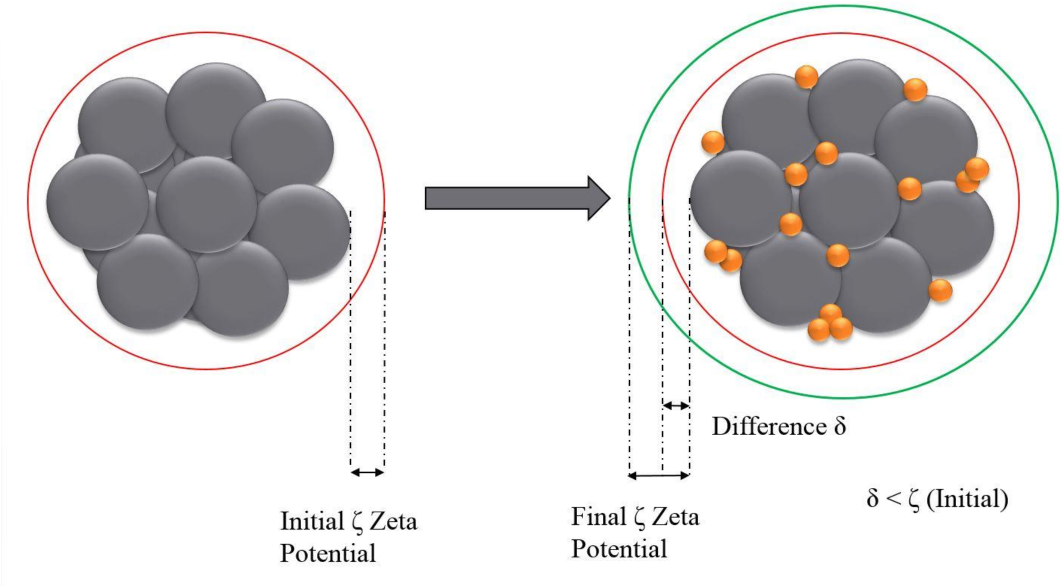

Figure 4.6 Modelling of the limited dispersion effect of acetylacetone in ethanol based colloidal solutions.

In fig. 4.6, the initial and final values of zeta potential values illustrated by Debye length approach where the δ is the difference between initial zeta potential and the final particle size. It is estimated the initial zeta potential, ζ (initial) value is smaller than the δ value such that if there exists no increase in the mean particles size by addition of acetylacetone, the final zeta potential would have been extended to higher values than obtained. Therefore, one can say that the dispersive ability of the acetylacetone is limited at that mean particle size values despite the enhancement in zeta potential values.

The second possibility is that due to the lack of addition of strong ionizing agents, the dispersive ability of the acetylacetone is limited. However, there exists some literature examples of solutions containing both acetylacetone and strong ionizing agents for which the minimum obtained particles size values are almost identical to what has been observed in this study. Therefore, the acetylacetone modelling of the ethanol based colloidal solutions is the most probable phenomenon.

### 4.3. Electrophoretic Deposition Using Stable Colloidal Solutions

As obtained from in Eq. [2.15], the necessary electrical field to conduct electrophoresis is directly proportional to effective particle sizes. However, the equation is applicable only for hypothetical single particle cases such that the calculation of minimum necessary electrical field is impractical for this situation. Therefore, the minimum necessary potential differences are investigated by ab-initio technique. In table 4.4 the necessary minimum potential differences of the four colloidal solutions are indicated.

Table 4.4 Necessary minimum potential difference values for colloidal solutions

| **Solution** | **IT** | **IA** | **ET** | **EA** |
|---|---|---|---|---|
| **Minimum Voltage (V)** | 11.0 | 9.0 | 4.0 | 3.5 |

The effect of acetylacetone on minimum necessary potential difference is not clearly observed, however it is obvious that increasing zeta potential values and decreasing mean particle sizes definitely decreases the minimum necessary potential difference. In accordance with this situation, it is possible to construct an equation:

$$V_{min} = A * \frac{a}{\zeta}$$

Eq. [4.3]

where $a$ is the mean particle size in nm, ζ is the zeta potential value in V and A is the empirical constant in $V^2$/nm. Processing the zeta potential and the mean particle size values, the determination of the empirical constant "A" is conducted in table 4.5.

Table 4.5 Calculation of the empirical constant in Eq. [4.3]

| **Solution** | **Zeta Potential ($Vx10^{-3}$)** | **Mean Particle Size (nm)** | **Minimum Voltage (V)** | **Empirical Constant ($V^2$/nm)** |
|---|---|---|---|---|
| **IT** | 4.02 | 241.70 | 11.0 | $1.82x10^{-4}$ |
| **IA** | 4.30 | 207.30 | 9.0 | $1.86x10^{-4}$ |
| **ET** | 7.06 | 150.60 | 4.0 | $1.87x10^{-4}$ |
| **EA** | 8.88 | 161.40 | 3.5 | $1.92x10^{-4}$ |
| **Average** | | | | $1.87x10^{-4}$ |

Considering the almost identical values of the empirical constant (A) in Eq. [4.3], it is observed that the minimum necessary potential difference is directly proportional to mean particle size ($a$) and inversely proportional to zeta potential (ζ) with an empirical constant (A), which is $1.87x10^{-4}$ $V^2$/nm.

## 4.4. SEM Characterizations of EPD Coatings

Using all four colloidal solutions, coatings were conducted with applying minimum necessary voltage values for 60 s. Afterwards, the coatings are examined using scanning electron micrograph in order to investigate the morphology, coating thickness and homogeneity. SEM images are taken from the cross-section of the specimens.

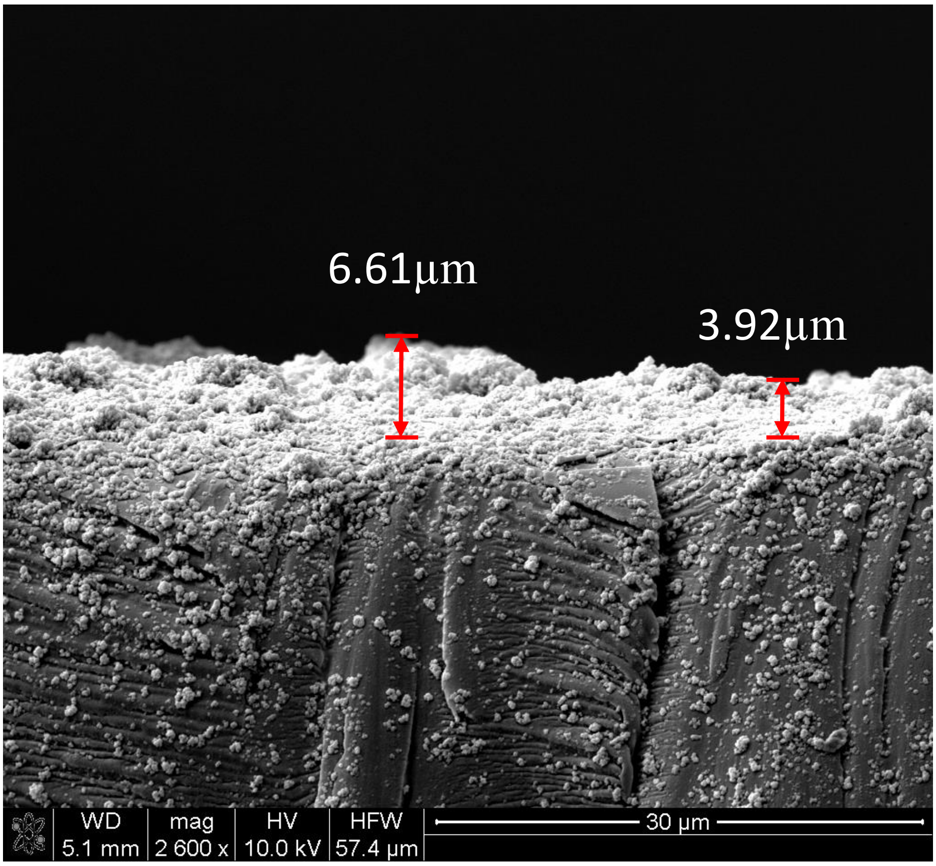

Figure 4.7 The SEM image of coating by using colloidal solution "IT" with applied 11 V for 60 s.

The coatings conducted using colloidal solution IT, as shown in fig.4.7, result in highly inhomogeneous coatings. It is obvious that there exists no control on coating thickness and morphology. The islands of agglomerates are also observed, clearly such that the inhomogeneous distribution of effective particle size within the colloidal solution is the main reason for such an inhomogeneous coating morphology. Additionally, the degradation of ITO layer is observed, indicating some sort of simultaneous oxidative electrolysis reaction taking place.

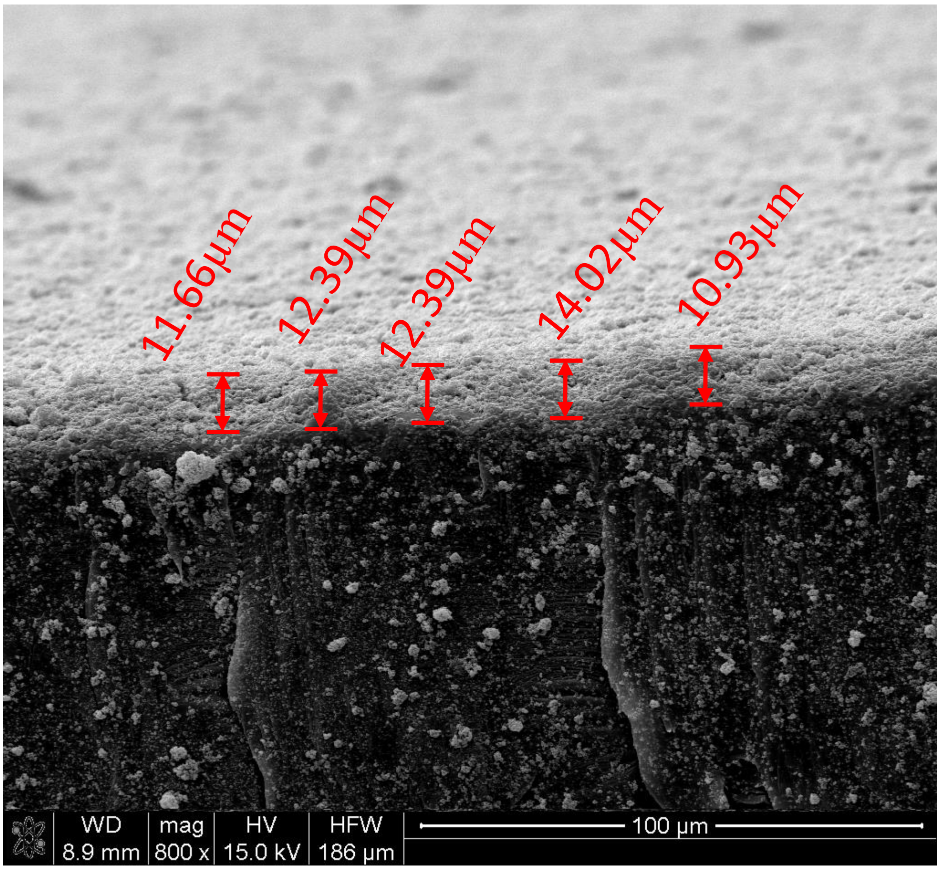

Figure 4.8 The SEM image of coating by using colloidal solution “IA” with applied 9 V for 60 s.

Investigating the coatings with the colloidal solution “IA”, a relatively homogeneous morphology and coating thickness properties are observed. The addition of acetylacetone effected the coating morphology, remarkably. The formation of a continuous and obtained relatively homogeneous coating thickness is a result of homogenized particle size distribution such that the effect of acetylacetone on the zeta potentials of isopropanol based colloidal solutions was not as significant as the effect on mean particle size and their distributions. Therefore, colloidal solution “IA” can be considered to perform excellently.

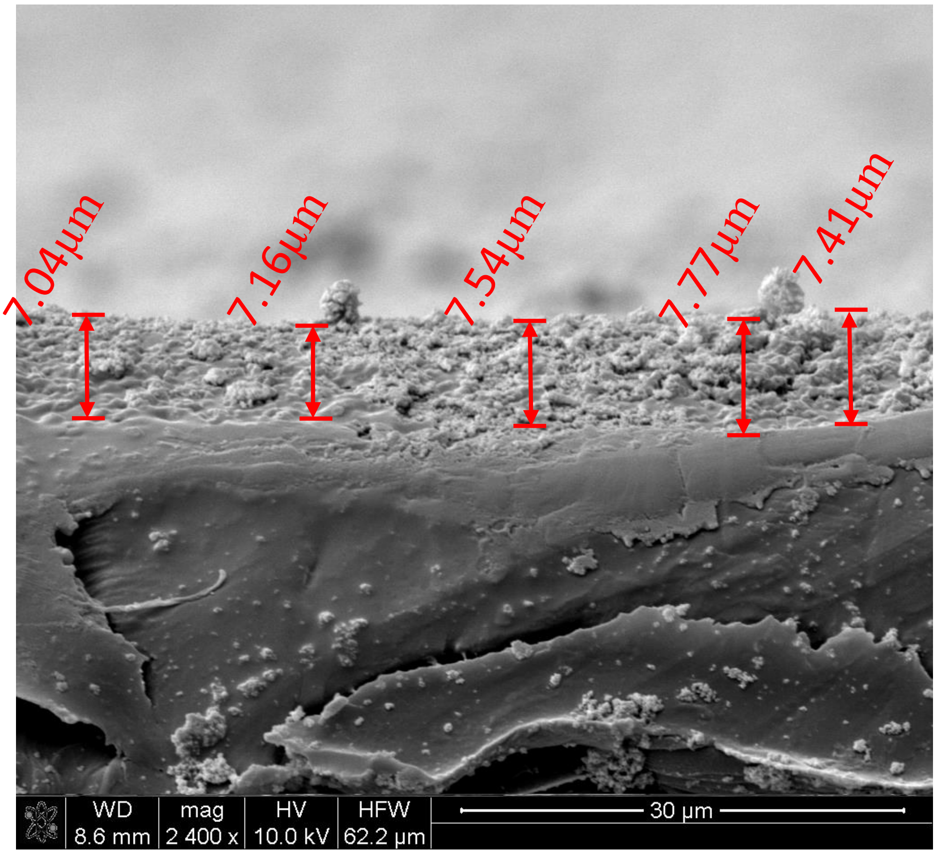

Figure 4.9 The SEM image of coating by using colloidal solution "EA" with applied 5 V for 60 s.

Coatings with the ethanol based solutions (ET & EA) were conducted with applied voltage of 5V, since there exists no significant difference in between the minimum necessary potential difference of both of the colloidal solutions. In fig. 4.9, the cross-section image of coating by using colloidal solution "EA", with an excellent result of coating thickness homogeneity. However, it is also possible to identify the agglomerates on the coating having diameter of micron levels. There exists micron size agglomerates residing in the colloidal solution such that the adverse effect of acetylacetone observed in ethanol based colloidal solution may extend to more severe levels. In order to conduct a further investigation of this case, the coating duration is extended to 120 s and the resultant SEM image is shown in fig. 4.10.

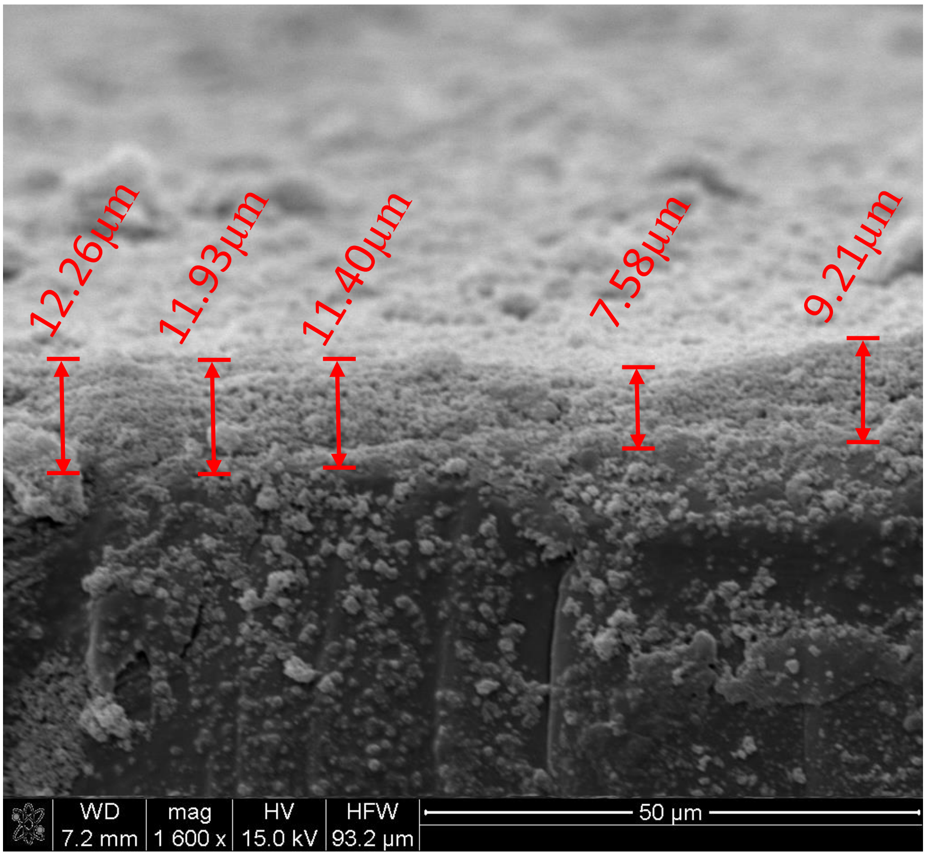

Figure 4.10 The SEM image of coating by using colloidal solution "EA" with applied 5 V for 120 s.

The SEM image of coatings by using solution "EA" with an extended duration of 120 s revealed the adverse effects more clearly. Extension of the coating duration, the coating thickness homogeneity was highly deteriorated that the micron size agglomerates are more visible by the tilted image of the coating.

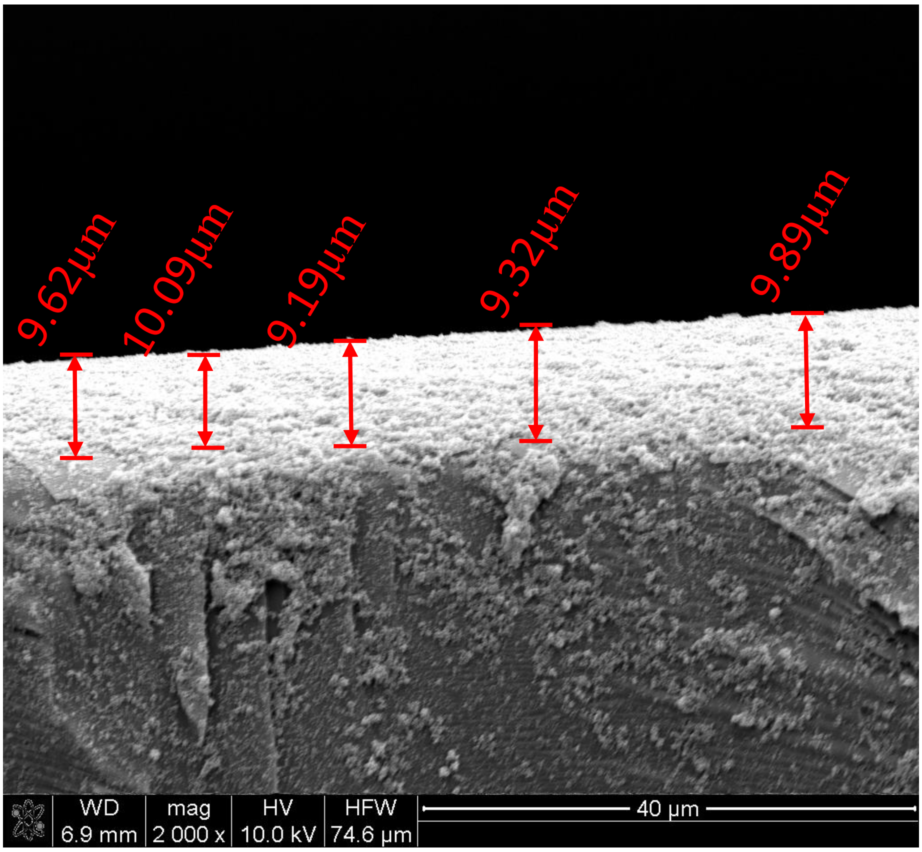

Figure 4.11 The SEM image of coating by using colloidal solution “ET” with applied 5 V for 60 s.

The contradictions on the acetylacetone addition in ethanol based solutions are solved by the investigation of SEM image of coating by using solution “ET” as shown in fig.4.11. The coating thickness and the morphology is extraordinarily homogeneous, despite the non-flat surface of the ITO/PEN substrates. As it can be observed in the previous images, the polymeric substrates are not as flat as other solid substrates like glass such that its highly soft and flexible properties lead to conflicts on surface coating. However, such a small angular lean is not a significant problem for EPD coatings as seen of fig. 4.11, that the coating homogeneity is still maintained. Furthermore, the coating duration for this colloidal solution is extended to 120, 180 and 240 s in order to observe the thickness limit for homogeneous coatings.

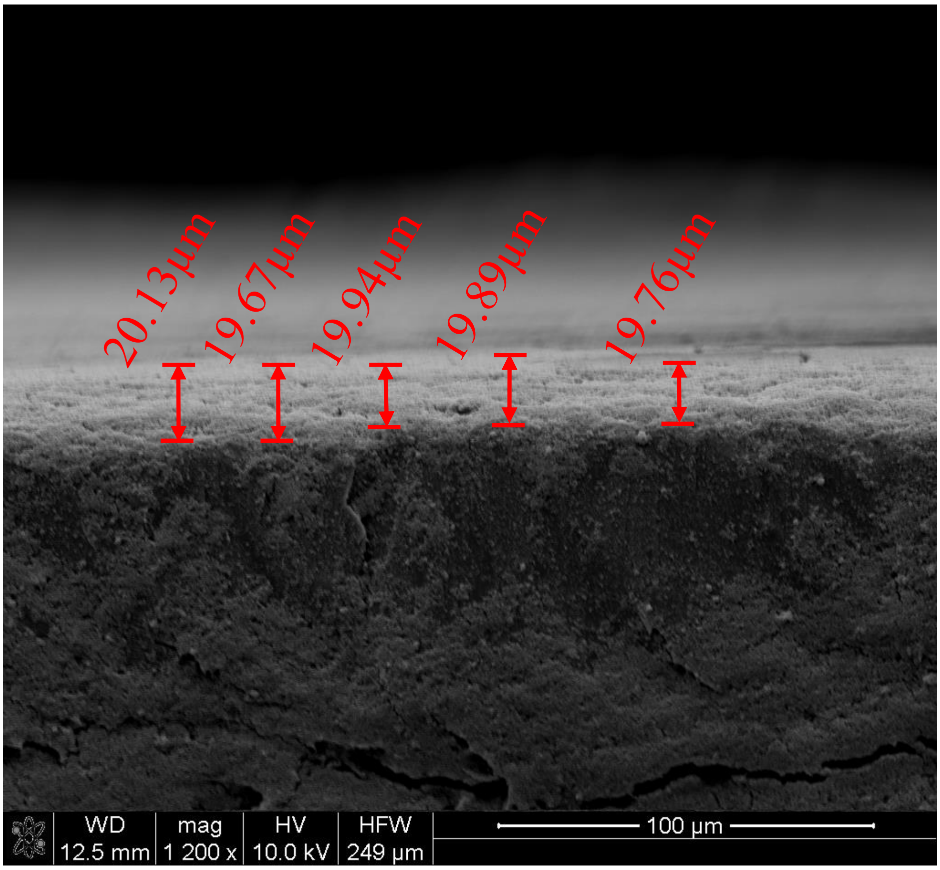

Figure 4.12 The SEM image of coating by using colloidal solution "ET" with applied 5 V for 120 s.

Extending the duration of coatings with colloidal solution "ET" to 120 s, the coating homogeneity is observed to be maintained. There exists no significant deviation along the coating in terms of thickness and no micron size agglomerates are observed. As mentioned chapter 3, the desired coating thickness of titania nanoporous layer for DSSC and/or FDSC applications is 15 µm. Therefore, it can be denoted that it is possible to obtain 15 µm of titania coatings with extraordinary homogeneity with a duration in between 60 – 120 s.

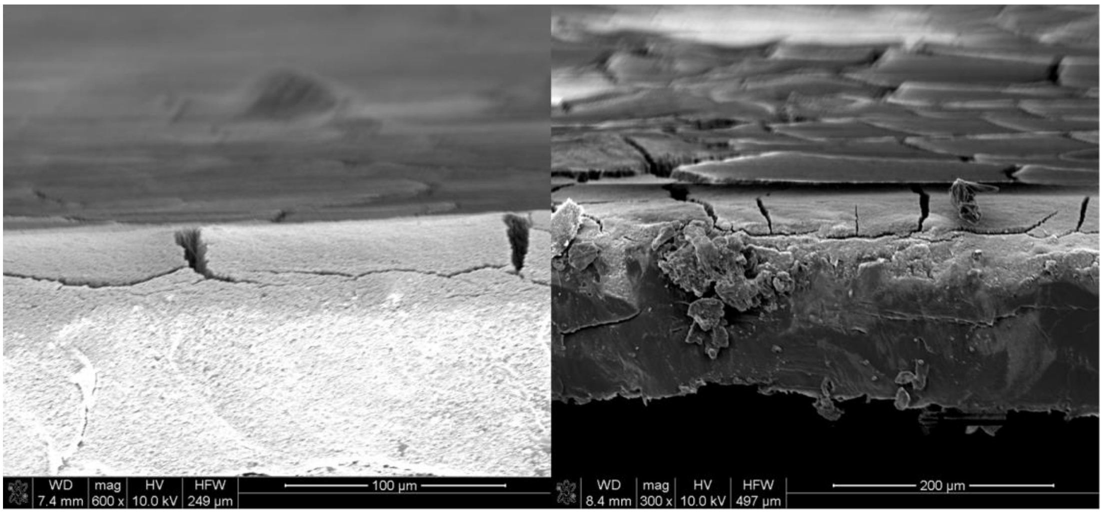

(a) (b)

Figure 4.13 The SEM images of coating by using colloidal solution “ET” with applied 5 V for (a) 180 s and (b) 240 s.

In fig.4.13a and fig.4.13b, the coating durations are extended to 180 s and 240 s, respectively. Although, the coating thickness homogeneity was observed to be better than that of the colloidal solutions “IT, IA and EA”, there exist cracks within the coatings due to the formation of an extensive capillary force during the evaporation of the excess solution. The reason for crack formations due to such capillary force is the utilization of highly volatile and low viscosity solvents along with lack of strong surfactants and binders. Considering the adverse effects of the proved-to-be the best performing surfactant, acetylacetone, this is another contradiction of binder-free electrophoretic deposition method.

Table 4.6 Mean coating thickness and deviations of coating using solutions “IT” and “IA”

| **Sample** | **IT(11V-60 s)** | **IA (9V – 60 s)** |
|---|---|---|
| **Mean Coating Thickness (µm)** | 5.21 | 12.34 |
| **Deviation (µm)** | 2.69 | 3.59 |
| **% Deviation** | 51.6 | 29.1 |

Table 4.7 Mean coating thickness and deviations of coating using solution “EA” with distinct durations

| **Sample** | **60 s** | **120 s** |
|---|---|---|
| **Mean Coating Thickness (μm)** | 7.38 | 10.48 |
| **Deviation (μm)** | 0.73 | 4.68 |
| **% Deviation** | 9.9 | 44.7 |

Table 4.8 Mean coating thickness and deviations of coatings using solution “ET” with distinct durations

| **Sample** | **60 s** | **120 s** | **180 s** | **240 s** |
|---|---|---|---|---|
| **Mean Coating Thickness (μm)** | 9.76 | 20.11 | 28.33 | 41.17 |
| **Deviation (μm)** | 0.51 | 0.91 | 2.93 | 5.26 |
| **% Deviation** | 5.2 | 4.5 | 10.3 | 12.8 |

Comparing the deviations is in the coating thicknesses obtained by using all four stable colloidal solutions as tabulated on table 4.6-7, the solution “ET” exhibited the least deviation as less than 1 μm. The deviations obtained for solutions “IA” and “IT” are 2.69 and 3.59, respectively while that of obtained for solution “EA” increased from 0.73 to a dramatic value of 4.68 when the coating duration is extended from 60 s to 120 s. However, as mentioned in table 4.8 also, the deviations are not catastrophic for solution “ET” up to coating durations of 120 s such that upon 20 μm of coating thickness values the coating homogeneity is guaranteed. In fig. 4.14, the coating thickness versus coating duration relationship is plotted for solution “ET”.

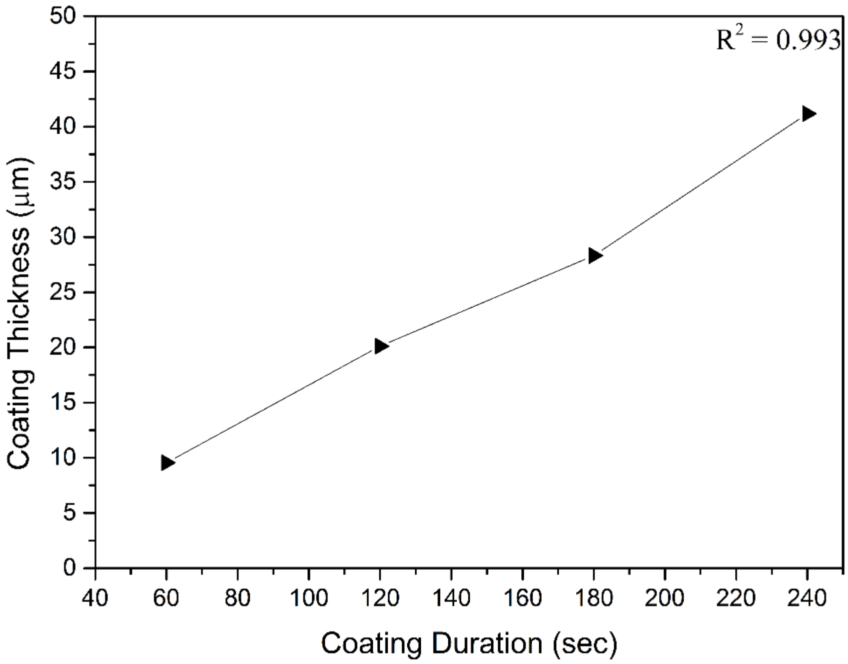

Figure 4.14 The graph of coating thickness vs. coating duration.

As shown in fig. 4.14, there exists almost a linear relationship in between the coating thickness and coating duration such that the regression ($R^2$) value of 0.993 proves such linearity. Therefore, using a linear interpolation, it is definite that 90 s of coatings will yield coating thickness of 15 μm with a deviation of less than 1 μm.

## 4.5. Current vs Time Analysis of Stable Colloidal Solutions During EPD Process

In order to yield a further investigation on the reasons for the differences in the coating characteristics of the four stable colloidal solutions, the change in current is examined with the coating duration through EPD process and plotted on fig. 4.15.

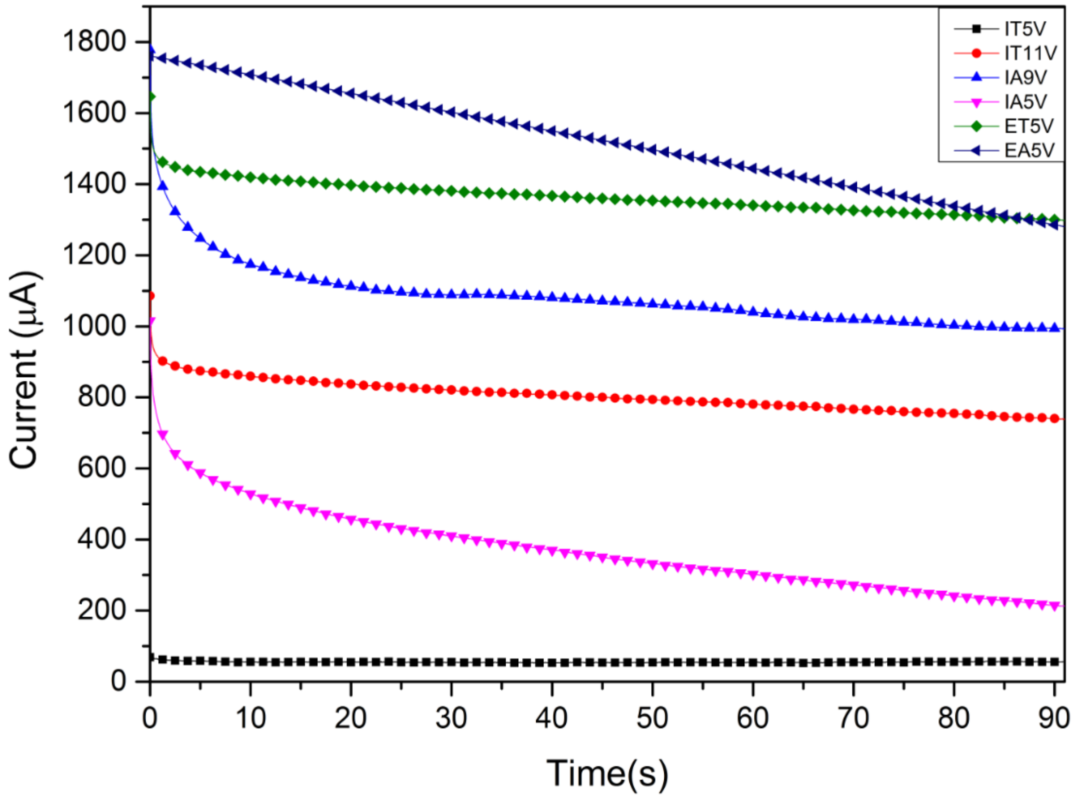

Figure 4.15 The change in the current vs. time graph for all colloidal solutions with distinct voltage values.

As electrophoretic deposition proceeds, it is natural to observe drops in the current. Throughout the coating process, the adhered ions on the surface of the nanoparticles are released directly into the solutions as the particles reaches and bonds with the electrode. Therefore, it is expected that both the ionic and electrical conductivity of the solution media to increase, which is also expected to increase the current passing through the solution. However, as coating of the electrode proceeds, the overall surface electrical resistance is increases, simultaneously, due to the coating of dielectric particles. Thus, there exists a dilemma on which one of the mechanisms to be the dominant.

Investigation of the current vs. time plots of the colloidal solutions has revealed the dominance of the current drop mechanism due to the reduction in surface resistance as the coating proceeds. However, the current drop rates for some of the solutions are more drastic comparing with the others. Considering the coating with solution “IA” at 5V of applied voltage, which is lower than the obtained threshold value, indicates that although there is no coating taking place, the current drop is, yet, observed. This means that rather than electrophoresis of particles, transport of adherent and free ions present in the solution is taking place towards the electrode. Since the ions reaching to the electrode remains idle and the voltage is insufficient for formation $H_2$ gas, the concentration of the mobile ions decreases, reducing the electrical conductivity of both solution and the electrode.

Comparing the current profiles of coatings with using solutions “IT” at 11 V and “IA” at 9V, the current vs time curve of solution “IT 11V” is observed to be more decent, while there are remarkable fluctuations on the curve of “IA 9V”. Despite such a difference, the performance of the coatings with solution “IT” is denoted to be the worst, especially considering the attainable maximum coating thickness at corresponding voltage values. If fact, it is nearly impossible to perceive such coating as a stable coating. The reason is the insufficient concentration of electrophoretically mobile particles within the solution “IT” as mentioned in the previous section using fig. 4.1. Analyzing the zeta potential measurements of both of the solutions by comparing the areas under the curve (the curves are estimated to have triangular shape) the number of ionized (area = 14800) particles in solution “IA” (area = 5700) is about 2.5 times higher than that in solution “IT”. Therefore, due to the lack of sufficient concentration of ionized particles, the coating homogeneity and reliable coating thickness values are restrained for coatings using solution “IT”, which also explains the overall low current values relative to solution “IA”. Additionally, the fluctuations observed for solution “IA” explains the lack of coating homogeneity despite the excellent obtained coating rates. The simultaneous transport of both particles and the free ions within the solution occurs such that in some time intervals, the idle ions on the electrode is replaced with upcoming particles, resulting in local increase in the solution conductivity as well as increase in the current.

The most stable and decent current profile is observed for solution “ET”. Neglecting the current incubation interval at first 5 – 6 s, the current vs time curve of which is relatively horizontal. Indicating a remarkable equilibrium between the reduction in the conductivity of the electrode and the increment in the conductivity of the solution. However, investigating the current profile of solution “EA”, although the overall current value is much higher than that of any of the other solutions, a relatively sharp decrease in the current is observed throughout the coating process. In fact, at interval around 82 – 85 s (fig. 4.16) the overall current value drops to the lower values than that of solution “ET”, which indicates that the coating rate is lower beginning at that interval. The sharp decreasing profile can be explained the lack of release of the adherent ions on the surface of the particles due to the acetylacetone content. Exceptionally, the addition of acetylacetone increased the mean particle size of the solution comparing with the non-additive ethanol based solutions. Therefore, it is proved that acetylacetone in ethanol acts as a binder rather than a dispersive surfactant.

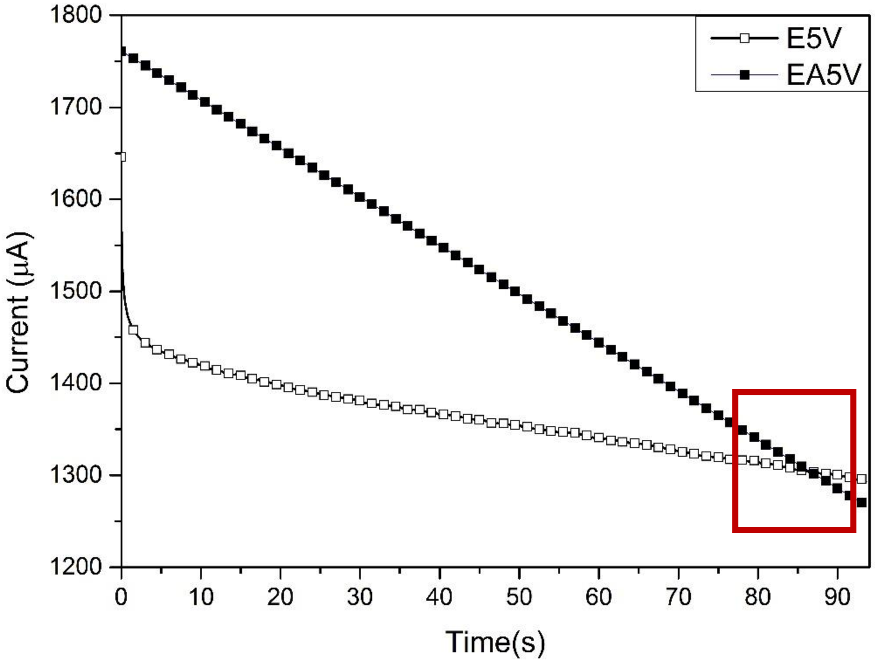

Figure 4.16 Current vs time graphs for solutions “ET” and “EA” at 5V of applied voltage.

## 4.6. XRD Analysis for Selective Anatase Deposition Properties

Optimizing the best performing colloidal solution for deposition of P-25 titania nanoparticles containing 80:20 anatase and rutile phases of which, the coatings were investigated using XRD method in order to observe whether selective anatase coating is achievable or not. In fig. 4.17, the schematic view of the purpose of the selective anatase coating during EPD process is shown.

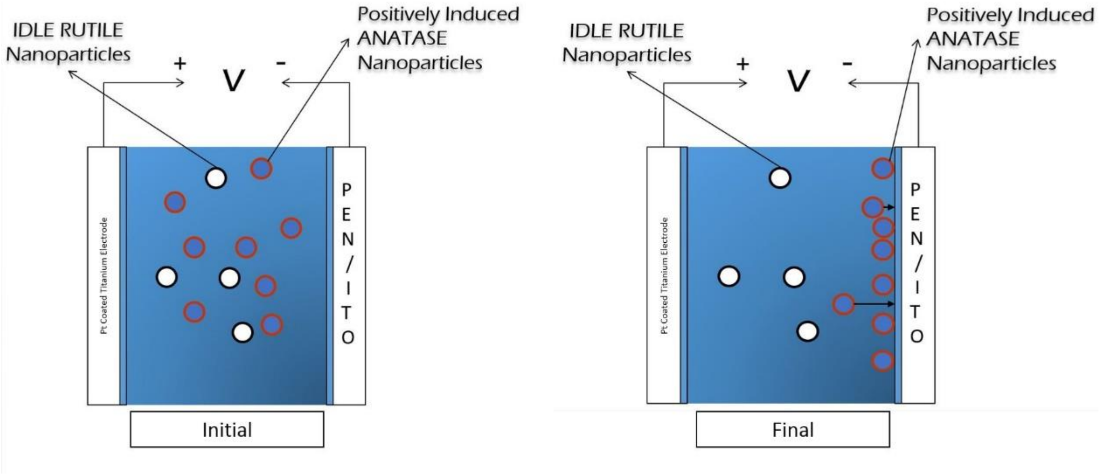

Figure 4.17 Schematic view of the aim of the selective anatase coating before and after EPD process.

As mentioned in section 4.1, the pH values of the solutions are adjusted to 5.2 – 5.3 in order to satisfy the isoelectric point of the rutile particles which is pH 5.2 – 5.3, roughly, while the isoelectric point of anatase is pH 6.3 [12]. As a reminder, if the colloids dispersed in a solutions which have the same pH value of their isoelectric point, then there is no observation of electrophoretic mobility of the particles such that under no applied voltage, transport of the particles occur. Therefore, adjusting the pH value of the colloidal solutions to the same value of the isoelectric point of the rutile, results in stationary (idle) rutile particles, favoring the coating of only anatase particles, as shown in fig. 4.17 “Final”.

In order to confirm whether such a selective coating concept is achieved or not, the phases involved in the coatings conducted by using colloidal solutions “ET” and “EA”. The reason of the investigation of solution “EA” is to examine the effect of acetylacetone of selective coating property. Additionally, as received P-25 particles are also analyzed in order to confirm that both rutile and anatase co-exist.

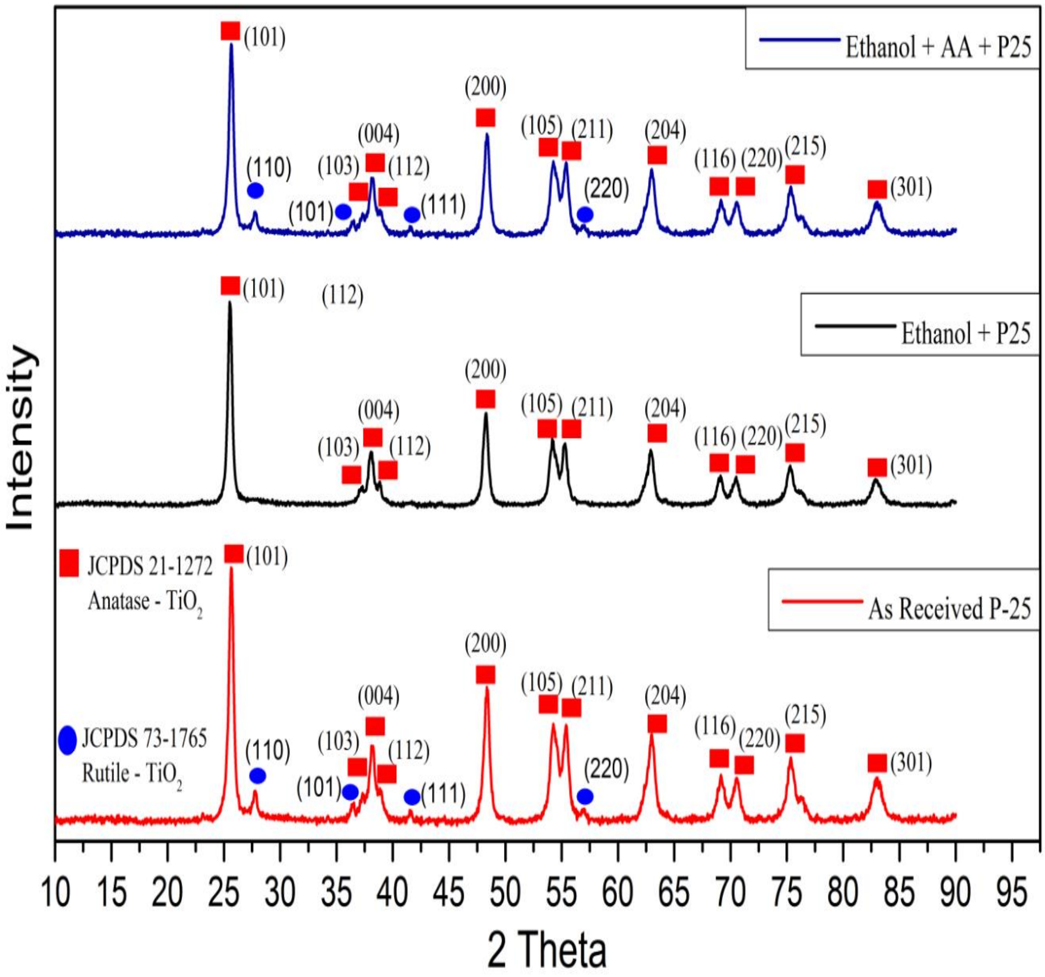

Figure 4.18 XRD spectra of coatings by using solutions “EA”, “ET” and as received P-25 particles.

The samples were prepared by peeling off the titania layer from the substrates which are coated with a thickness of 15 µm. This method expected to provide a highly precise examination of a real case scenario such that sample prepared with excessive coating thickness and durations may have deteriorate the selective property of the applied EPD. In fig.4 18, the XRD Diagrams of coatings with four distinct EPD solutions and as received P-25 nanoparticles are plotted. Investigating the diagrams of each type of coatings, one can say that almost no rutile phase is observed for the coatings with using solution "ET". The most intense peak plane of rutile phase is (110) plane which is almost diminished to the background as shown in figure. 4.18. Although, the addition of acetylacetone addition does not differentiate the pH values of the solutions, it deteriorates its selective properties due to the effect explained on fig. 4.6. Examining the SEM images of the coatings using solution "EA", it is highly possible that the observed micron size agglomerates contains excess amounts of rutile within. In addition to existence of micron size colloids , it was proved in the previous section that the behavior of acetylacetone as binder rather than a dispersive surfactant such that there is a possibility of intact rutile particles on anatase colloids. Therefore, one can say that colloids in non-additive solutions are agglomerates of either only rutile and/or only anatase phases of titania. Furthermore, there is a possibility that adsorbed acetylacetone on colloids may have altered the surface pH value of the rutile particles such that the effective isoelectric point of rutile, possibly anatase also, is diverged from its intrinsic value.

### 4.7. SEM Characterizations of Compressed Coatings

The nanoporous photoanodes are fabricated by coating using solution "ET" with a coating duration of 90 s at 5V with a subsequent compression using cold isostatic pressing method. As indicated in section 3.2.5, the coatings are compressed at three different pressure intervals of 150 MPa, 225 MPa and 300 MPa, with an alternating pressure profile shown in fig. 3.7.

Table 4.9 Measured coating thickness values of the compressed and non-compressed specimens

| **Sample** | **EPD** | **CIP150** | **CIP225** | **CIP300** |
|---|---|---|---|---|
| **Coating Thickness (µm)** | 16.17 | 15.41 | 15.09 | 14.89 |

Analyzing the data in table.4.9, it is observed that EPD coatings with a duration 90 s at 5V yield a 16 µm of coatings for which the expected coating thickness was 15 µm. Fortunately, due to the desired final thickness of 15 µm for DSSC and FDSC applications, the excess 1µm coating provided an safety factor, considering the inevitable contraction under the compression. The sample were named as their CIP compression levels such that "CIP150" indicates compression at 150 MPa and similar correspondence can be applied for other samples. Although the compression levels are highly extensive, the contraction of the coatings did not exceed 1.5 µm at the maximum compression level. Therefore, the final coating thickness values were considered to be in the vicinity of the desired value.

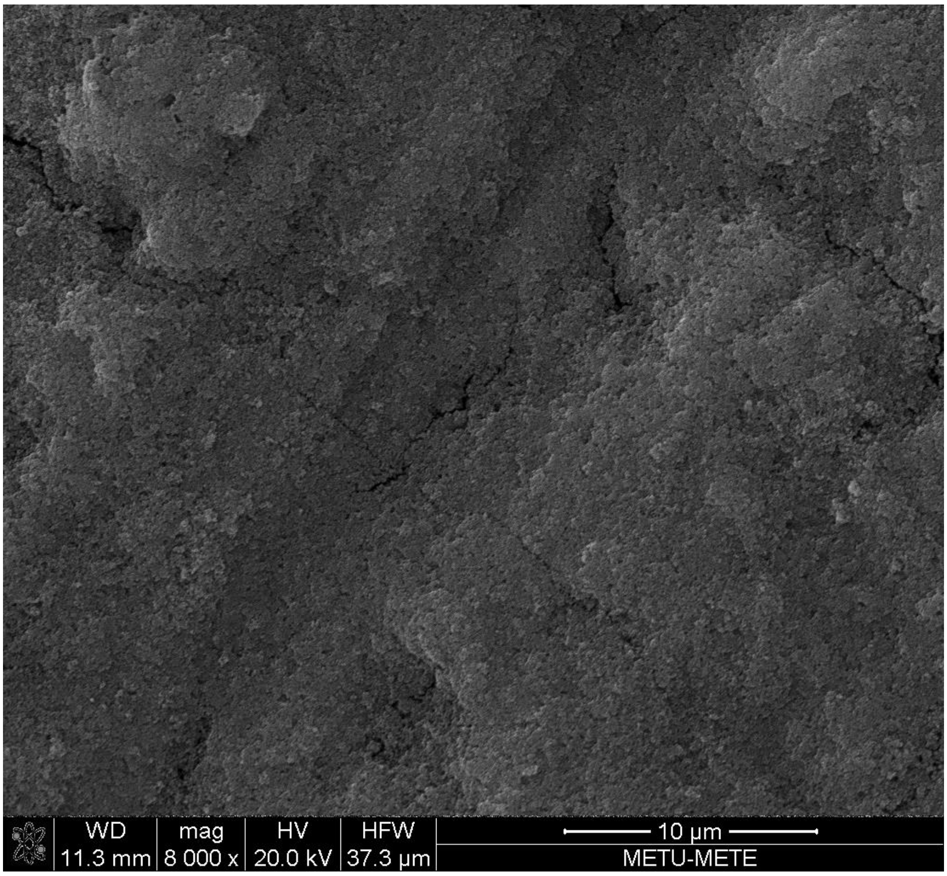

Figure 4.19 SEM image of the photoanode compressed at 150 MPa.

The compression at 150 MPa yield a fine mechanical stability while bending of the flexible substrates. However, as shown in fig. 4.19, there exists regions lacking particle interconnection such that the total homogenization of the porosity is not achieved. The observed crack-like regions prove this problem.

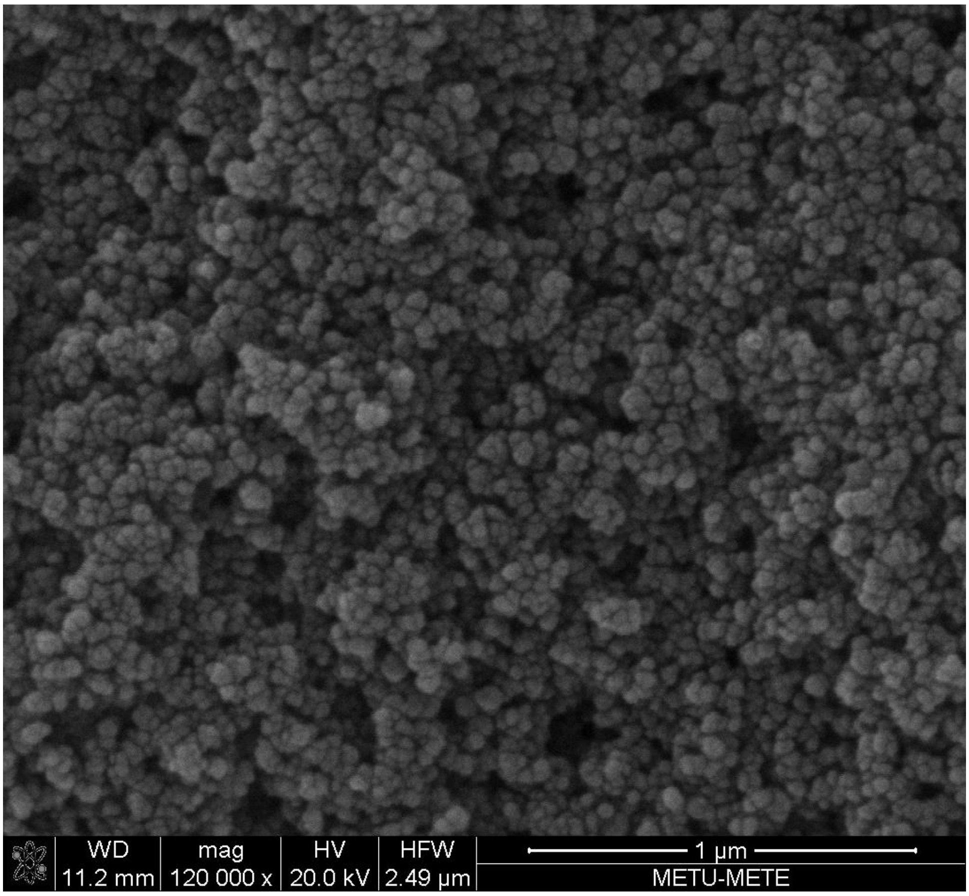

Figure 4.20 SEM image of the nanoporous structure of photoanode compressed at 150 MPa.

Although the coalescence of the pores in specific regions resulted in voids and crack-like structure, a well-developed nanoporous structure is still observed, in fig. 4.20.

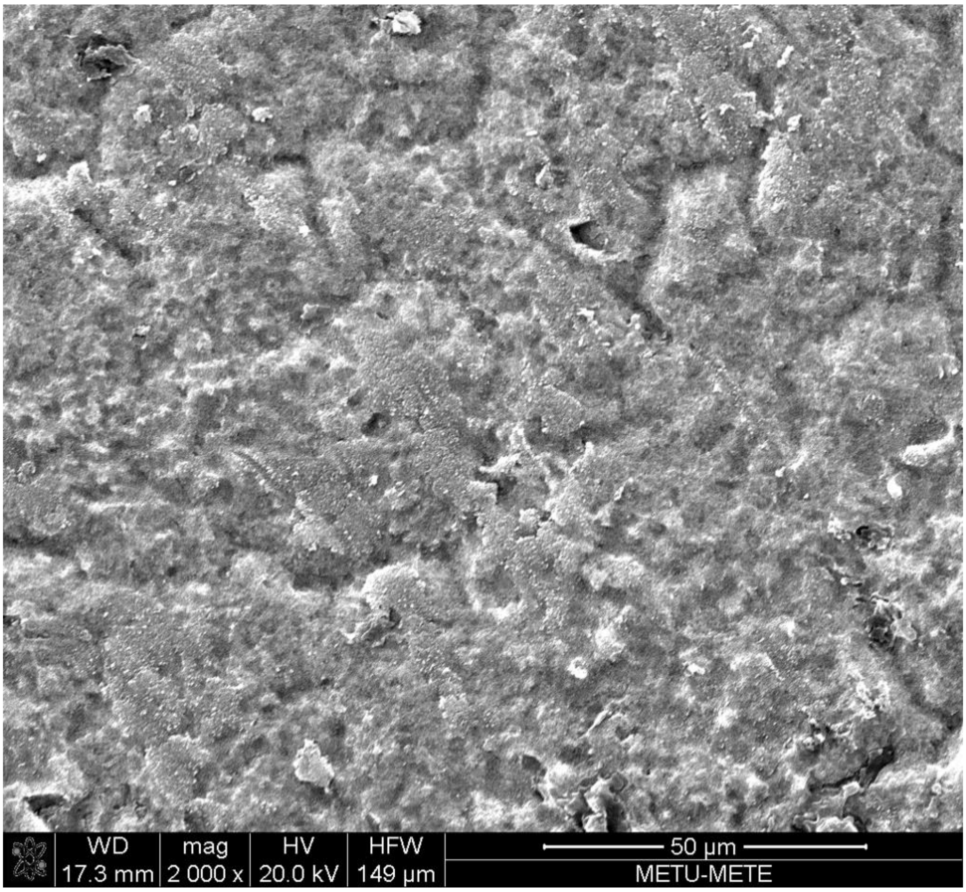

Figure 4.21 SEM image of the photoanode compressed at 225 MPa.

In fig. 4.21, it is clearly observed that the compression level of 225 MPa was sufficient enough to eliminate the voids and crack-like structures which are observed in samples compressed with 150 MPa. Although, the fabricated photoanodes yield a high surface roughness, the channel-like structures prove that the voids and cracks are filled by 225 MPa compression and interconnection of the particles are relatively homogenized.

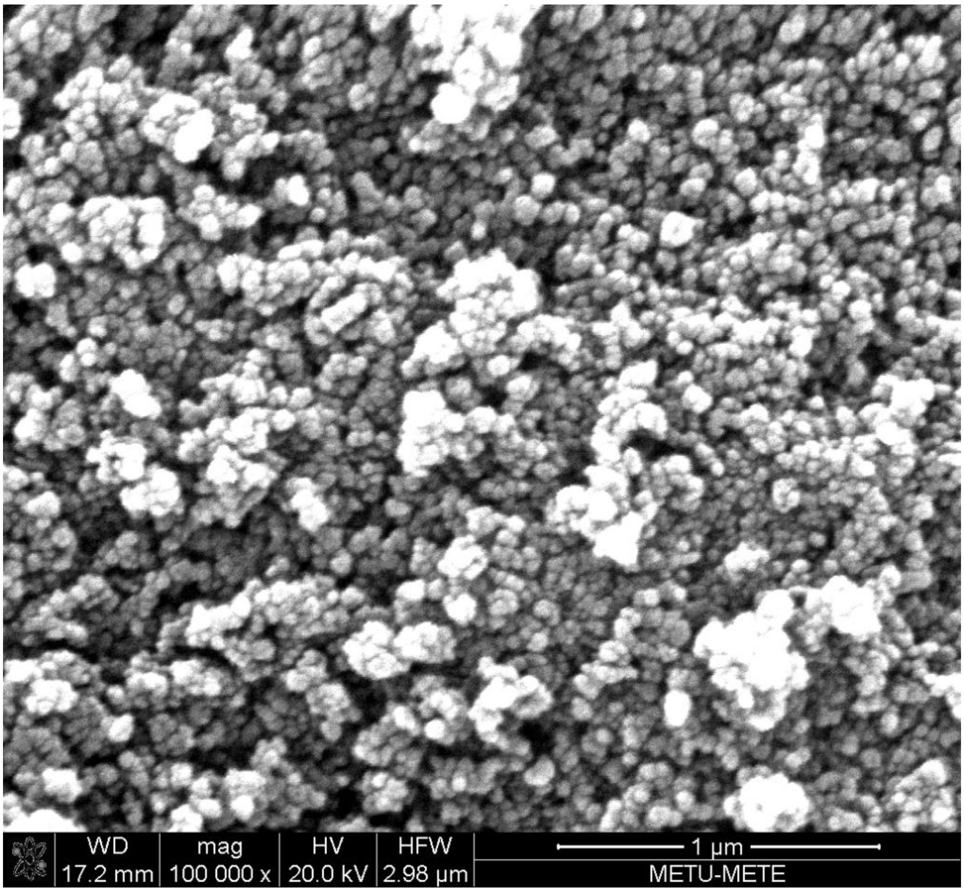

Figure 4.22 SEM image of the nanoporous structure of photoanode compressed at 225 MPa.

Examining the nanoporous structure of the photoanodes compressed at 225 MPa, in fig. 4.20, it is observed that the pore sizes and the distribution of the pores are much more homogeneous comparing with the photoanodes compressed at 150 MPa.

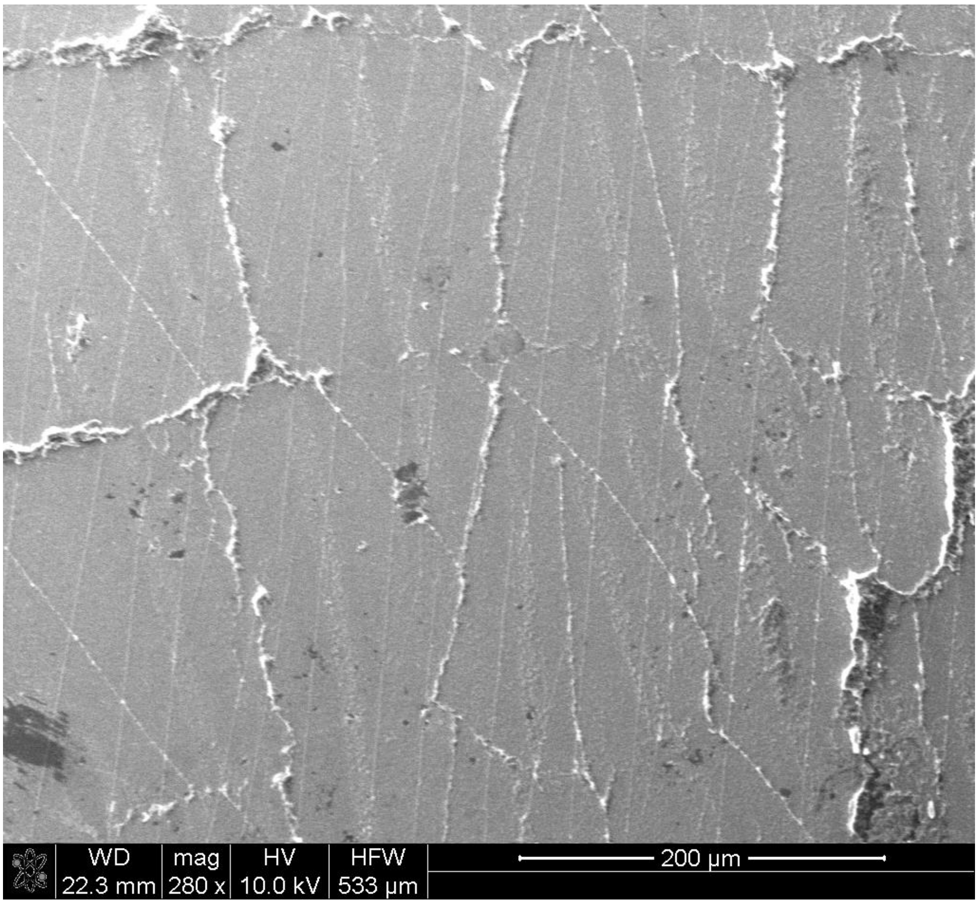

Figure 4.23 SEM image of the photoanode compressed at 300 MPa.

However, considering the samples with applied pressure of 300 MPa, in fig. 4.21, the titania layer is mostly peeled off, leaving remnant titania layers and potential ITO cracks are formed. Therefore, the sheet resistance of those substrates has been measured to have about 30 times larger than the as received substrates. Although 12 out of 15 compressed specimens failed to exhibit a stable nanoporous thick film, remaining stable coatings were assembled into cells in order to investigate whether ITO layer is still damaged or not. It is obvious that the case of ITO cracking will definitely decrease the overall cell efficiency.

### 4.8. Solar Performances of Assembled Cells

The assembled cells are characterized using solar simulator under AM 1.5 conditions and plotted in fig. 4.24. Investigating the photocurrent – voltage curves (I-V curves) of the cells, the largest I-V curve is obtained for the cell which is coated using selective EPD with a subsequent CIP at 225 MPa. Comparing the cells one of which is compressed at 150 MPa and the other one is compressed at 225 MPa, the effect of the void/crack filling is clearly observed. The homogenization of the pore size and distribution lead to an enhancement in obtained photocurrent values for cell which is compressed at 225 MPa. This is also due to the enhancement in interconnection of the particles such that increasing the bonding of the particles provides an improvement in the concentration of the transport of the electrons through metal oxide layer into TCO layer.

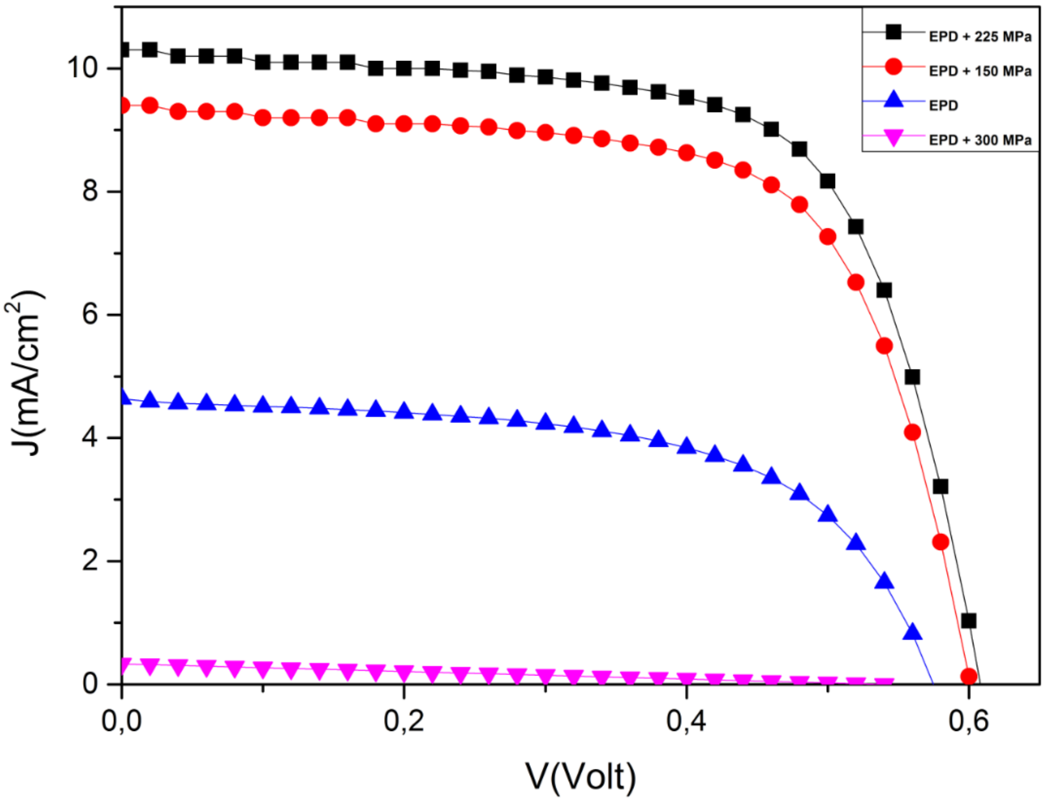

Figure 4.24 I-V curves of assembled cells.

Considering the samples which are compressed at 300 MPa, the obtained photocurrent and voltage values are even lower than that of the non-compressed samples. Comparing the photocurrent – voltage characteristics of compressed and non-compressed samples, the enhancement in the interconnection of the particles are observed clearly. Although, there exists no temperature or compression driven interconnection of particles for the non-compressed samples, it is proven that secondary weak physical bondings among the particles are sufficient enough for the transport of the electrons.

As mentioned before, the photocurrent – voltage values are measured under AM 1.5 conditions such that the power inlet is 100 mV/cm$^2$. The efficiency, $\eta$ (%) is the conversion percentage of the input solar power into electrical power as indicated in Eq. 4.4.

$$\eta(\%) = \frac{P_{con}}{P_{in}}$$

Eq. [4.4]

where the $P_{con}$ is maximum obtained power within the cell and $P_{in}$ is input power, which is 100 mV/cm$^2$ considering AM 1.5 conditions.

In hypothetical solar cells the maximum obtained power is as indicated in Eq. [4.5] such that the I-V curve is expected to exhibit a perfect rectangular shape.

$$P_{con} = V_{OC} * J_{SC}$$

Eq. [4.5]

However, due to the series resistances within the cell and the contact regions, it is impossible to obtain a perfect rectangular I-V curve, by which the Eq. [4.5] is not applicable. Therefore, the term “Fill Factor (FF)” is introduced in order to define the deviation of the obtained maximum power of the cell from the hypothetical maximum power values in Eq. [4.6]

$$FF(\%) = \frac{V_{MP} * J_{MP}}{V_{OC} * J_{SC}} * 100$$

Eq. [4.6]

Substituting the FF (%), $V_{OC}$ and $J_{SC}$ terms into the Eq. [4.4], the calculation of efficiency, ɳ (%) is conducted by using Eq. [4.7].

$$\eta(\%) = \frac{V_{OC} * J_{SC} * FF(\%)}{100mV/cm^2}$$

Eq. [4.7]

Table 4.10 Overall solar performances of the assembled cells

| **Sample** | **$J_{SC}$ (mA/cm$^2$)** | **$V_{OC}$ (V)** | **FF (%)** | **ɳ (%)** |
|---|---|---|---|---|
| **CIP 225 MPa** | 10.3 | 0.61 | 67.25 | 4.22 |
| **CIP 150 MPa** | 9.4 | 0.60 | 62.90 | 3.55 |
| **EPD** | 4.6 | 0.57 | 59.06 | 1.55 |
| **CIP 300 MPa** | 0.37 | 0.54 | 5.11 | 0.01 |

Upon obtaining the $J_{SC}$, $V_{OC}$ values the calculated FF (%) and ɳ (%) is calculated in accordance with the Eq. [4.7] and tabulated on table 4.10. The enhancement in the photocurrent values are clearly observed as the compression level increases up to 225 MPa. Although the effect of the quality of the interconnection among the particles enhances the photocurrent values, there is no net effect of which on voltage enhancement.

Considering the sample compressed at 300 MPa, excessive series resistances are observed such that almost no photocurrent is obtained while the corresponding I-V profile is linear rather than a curve indicating the dominance of the series resistances over shunt resistances within the cell. Therefore, it is proved that the cracking of the ITO layer due to excess compression level. Additionally, increasing FF (%) indicates the decrease in the series resistances within the cell by which the I-V profiles approach to the hypothetical.

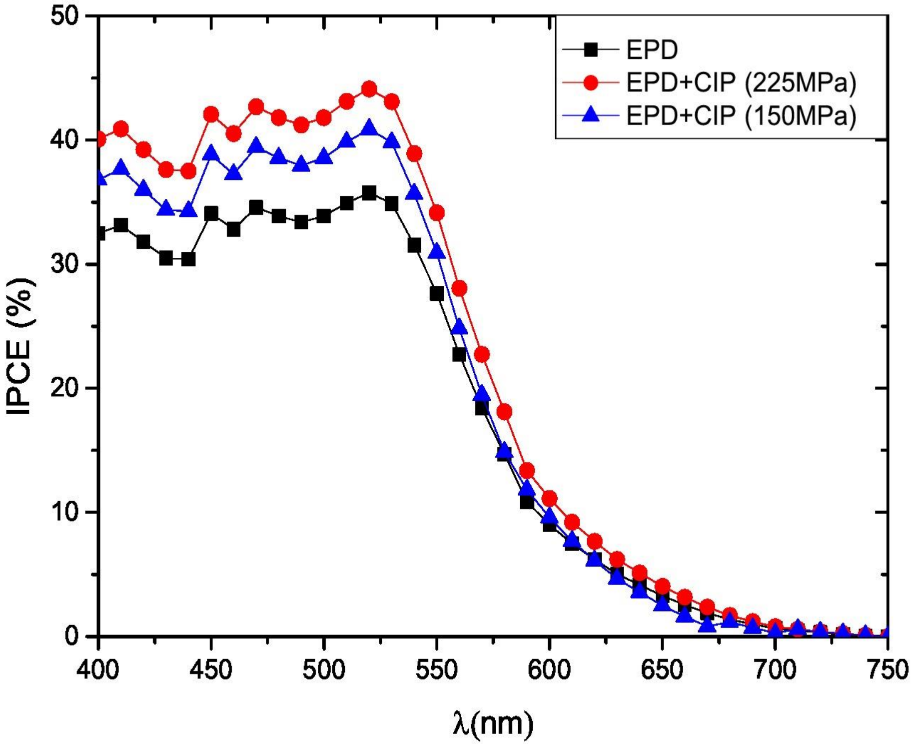

Figure 4.25 Incident photon to current conversion efficiencies (IPCE) of the assembled cells.

As mentioned in section 2.3.3, the short circuit losses directly effects the IPCE (%) performances of the cells. In dye sensitized solar cell, the most common reason for short circuit losses is due the lack proper interconnection among the particles. Although the investigation of the I-V curves of the cells provided a remarkable observation on the increase in the particular interconnection with the increasing compression levels up to 225 MPa, comparison of the IPCE (%) performances of the cells is the most accurate investigation in order to examine the effect of the compression levels on the particular interconnection.

In fig. 4.25, the IPCE (%) performances of the cells depending on the corresponding wavelength of the incident light are plotted. Similar to the I-V curves of the cells, the IPCE (%) performances confirms the desired effect of the compression. The cells which are compressed at 225 MPa exhibited the highest IPCE (%) values while the non-compressed cells exhibited the lowest values compared to the others. Additionally, considering the cells which are compressed at 300 MPa did not exhibit any photon to current conversion with the incident light such that damage on the ITO layer restrained the transport of the electrons.

# CHAPTER 5

# CONCLUSION AND SUGGESTIONS

In this study, the production and development of “flexible” dye sensitized solar cells using electrophoretic deposition method with a subsequent cold isostatic compression has been accomplished.

The deposition of the P-25 nanoparticles are performed by electrophoretic deposition method. The formation of the nanoporous thick films of rutile free anatase particles are achieved using the selective coating ability of the electrophoretic deposition. The preparation and the optimization of the colloidal solutions of P-25 titania nanoparticles for electrophoretic deposition process was conducted, initially. The criteria for the determination of the optimum solution were desired attainable pH values at around pH 5.2-5.3 for the selective anatase coating, minimum possible agglomerate sizes for colloids within the EPD solutions, stable dispersion, unreactive solution media and increased zeta potential values for enhanced electrophoretic mobilities of the particles. Among 20 experimented solutions 4 of which was initially labelled as candidate solutions satisfying the all criteria mentioned. However, a secondary investigation of the colloidal solutions was necessary concerning the criteria of enhanced zeta potential values, reduced agglomerate sizes of colloids, desired coating thickness values with homogeneous coating morphology and formation of rutile free titania nanoporous coatings. Therefore, EPD coating performances of ethanol and isopropanol based and their acetylacetone additive colloidal solutions are investigated by Zeta Potential measurements, particle size analysis, SEM and XRD method. The mean colloid sizes were measured using Zetasizer in order to obtain the mean agglomerate sizes of the colloids within the solution and the zeta potential values of the particles within each distinct solutions are measured in order to compare the electrophoretic mobilities of the particles and the minimum necessary voltage values to be applied for EPD process.

Using SEM, the coating thickness measurements and examination of the coating morphologies are conducted while analysis of selective coating properties is performed using XRD method.

Investigation and the comparison of the coatings of the 4 distinct colloidal solutions non-additive ethanol based solutions are determined to be the optimum colloidal solution in order to perform nanoporous anatase coatings using EPD method. The coatings using isopropanol based solutions were suffered from the lack of proper coating homogeneities while the mean particle size values were much higher and the zeta potential values were moderate considering the ethanol based solutions. Although, the acetylacetone addition into the isopropanol based solutions resulted in enhancement in the EPD properties of the solutions by increasing the coating homogeneity and decreasing the mean agglomerate size, the effect of acetylacetone in the ethanol based solutions was limited to enhancement of zeta potential only. In fact, the mean colloid size has increased due to such addition which can be considered as a highly adverse effect. Furthermore, comparing the SEM and XRD results, the optimum colloidal solution for fabrication of nanoporous photoanodes was determined to be the non-additive ethanol based solution since the coating homogeneity was maintained at the desired thickness values while the rutile free nanoporous coatings were achieved, simultaneously.

Upon overall optimization of the EPD process, the cold isostatic compression is applied with an alternating pressure profile in order to enhance the obtained the photocurrent and the incident photon to current conversion efficiencies of the assembled cells by increasing the interconnection of the nanoparticles. The substrates were coated with a thickness of 16 µm with anatase nanoparticles, then the photoanodes were subjected to compression levels of 150, 225 and 300 MPa. The coating thickness values of the compressed photoanodes measured by profilometer and the contraction in the coating thickness values are obtained to be less than 1.5 µm at 300 MPa. The morphologies and the distribution of the pores of the coatings were investigated using SEM. It is acquired that the optimum compression level is 225 MPa while the compression at 300 MPa is observed to crack the ITO coating on the PEN substrate. However, SEM characterizations were insufficient to determine the overall optimum compression level. Therefore, the compressed and non-compressed samples were assembled into cells by adsorption of the sensitized dye, sandwich closure with Pt coated ITO/PEN counter electrode and injection of the liquid redox electrolyte.

Finally, the solar performances of the assembled cells were investigated for four types of samples with surface areas of 1x1 cm$^2$. Plotting the I-V curves of the samples, remarkable enhancements in photocurrent values of the samples at compression levels up to 225 MPa for which the obtained efficiency was at maximum as 4.22%. Comparing the samples which are compressed at 150 MPa and 225 MPa with non-compressed specimens, major increase in the short circuit current ($J_{SC}$) values from 4.6 mA/cm$^2$ to 9.6 mA/cm$^2$ for 150 MPa and 10.3 mA/cm$^2$ for 225 MPa compression. Similarly, the fill factors (FF) values were enhanced from 59.06 to 62.90 and to 67.25, respectively, indicating the interconnection among the particles for electron transport within the nanoporous layer. Considering the samples compressed at 300 MPa, the IPCE measurements have revealed and proved the damage of the ITO layer which was also observed by SEM characterizations. The IPCE (%) value of which was measured to be zero such that there exists no photon to current conversion occurring within. Therefore, it was obtained that the optimum compression value is 225 MPa.

In conclusion, the production of the “flexible” dye sensitized solar cells by using selective electrophoretic deposition method with a subsequent cold isostatic compression has been successful. These processes are highly versatile, easily applicable and require almost no heat treatment apart from simple drying process. The electrophoretic deposition of the titania nanoparticles is highly applicable not only for polymeric substrates but also for any other substrates types like ITO/Glass, stainless steel and titanium foils. The elimination of the undesired phase of the titania (rutile) and the homogeneity of the coatings proved that the electrophoretic deposition is superior to other types of coatings utilized for fabrication of dye sensitized solar cells. Although the obtained efficiency values are highly satisfying, these values are way more minor comparing with the obtained efficiencies for conventional ones. It is obvious that cold isostatic compression cannot be a perfect alternative for the heat treatment applied for conventional dye sensitized solar cells in order to obtain perfect interconnection among the nanoparticles. Additionally, the liquid electrolyte is not practical for flexible dye sensitized solar cells and should be replaced with gel electrolyte in order to increase the stability upon exposure of bending. Combining these two facts, the maximum attainable efficiency for flexible dye sensitized solar cells are obliged to be dominated by the conventional ones. Although dye sensitized solar cells may be perceived not to be perfectly applicable to flexible substrates, considering small scale mobile electronics such as mobile phones, tablets, radio, mp3 players, “flexible” dye sensitized solar cells are one of the best candidate available for in-situ renewable energy devices.

# REFERENCES

[1] Luque, S. Hegedus, Handbook of photovoltaic science and engineering (2nd edition), Wiley, UK 2011

[2] Monthly Module Price Index, Photon International (November 2009), pp 84–87.

[3] Fath P, Keller S, Winter P, Joos W, Herbst W, Proceedings of the 34 IEEE PVSC, Philadelphia, pp 002471-76 (2009).

[4] Wiser R, Barbose G, Peterman C, Darghouth N, Tracking the Sun – II: Installed costs of PV in the US from 1998–2008, US Department of Energy Lawrence Livermore Berkley Laboratory (on-line) 2009. Retrieved from: http://eetd.lbl.gov/ea/emp/re-pubs.html. (Accessed on 14.07.2014)

[5] S. Kambe, 3rd Int. Conference on Industrialisation of DSC, Japan, April 2009

[6] S. Ito, T.N. Murakami, P. Comte, P. Liska, C. Grätzel, M.K. Nazeeruddin, M. Grätzel, Thin Solid Films, 516, 4613, 2008

[7] M. Grätzel, Acc. Chem. Res., 42, 1788, 2009

[8] N. Ikeda and T. Miyasaka, Chem. Lett. 36, 466, 2007

[9] C. Kothandaraman, T. Tonon, C. Huang, A. Delahoy, Mater. Res. Soc. Symp. Proc. 219, 475, 1991

[10] A. Hedler et al., Proc. 34th IEEE Photovoltaic Specialists Conference, 1102, 2009

[11] A. Fahmi, C. Minot, Physical Review B, Volume 47, 18 (1993) 11 717 – 11 724

[12] Marek Kosmulski “Chemical Properties of Material Surfaces” Marcel Dekker, Inc.: New York, Basel. 2001.

[13] Total Solar Irradiance, National Geophysical Data Center (on – line), 2014. Retrieved from: www.ngdc.noaa.gov/stp/solar/solarirrad.html. (Accessed on 11.07.2014)

[14] Best Research – Cell Efficiency Chart National Renewable Energy Laboratory (on – line), 2014. Retrieved from: www.nrel.gov/ncpv/images/efficiency_chart.jpg. (Accessed on 13.07.2014)

[15] R. C. Neville, Solar Energy Conversion The Solar Cell 2nd Edition, Elsevier Science B.VA., Amsterdam, 1995

[16] T. Markvart and L. Castafier, Solar Cells: Materials, Manufacture and Operation, Elsevier, Amsterdam. 2005

[17] F. Kreith and Y. Goswami, Handbook of Energy Efficiency and Renewable Energy, Taylor and Francis Group, USA, 2007

[18] Tanaka T et al., Proc. 17th Euro. Conf. Photovoltaic Solar Energy Conversion, pp 989–994 (2001).

[19] B. Sorensen, Renewable Energy: Its physics, engineering, use, environmental impacts, economy and planning aspects 3rd Edition, Elsevier Science, Amsterdam, 2004

[20] R Sastrawan, Photovoltaic modules of dye solar cells, PhD dissertation, Freiburg im Breisgau, 2006

[21] Wu X, Mulligan W, Coutts T, Thin Solid Films 286, 274 (1996).

[22] Wu X, Coutts T, Mulligan W, J. Vac. Sci. Technol. A15 (3), 1057 (1997).

[23] Kluth O, Agashe C, Hupkes J, Muller J, Rech B, 3rd WCPEC-3, 2, 1800 (2003).

[24] Minami T, Semicond. Sci. Technol. 20, S35 (2005).

[25] Yaglioglu B, Huang Y-J, Yeom H-Y, Paine D, Thin Solid Films 496, 89 (2006).

[26] Z. Xue, W. Zhang, X. Yin, Y. Cheng, L. Wang, B. Liu, RSC Advances, 2, 7074–7080, 2012

[27] D. O. Scanlon, C. W. Dunnill, J. Buckeridge, S. A. Shevlin, A. J. Logsdail, S. M. Woodley, C. R. A. Catlow, M. J. Powell, R. G. Palgrave, I. P. Parkin, G. W. Watson, T. W. Keal, P. Sherwood, A. Walsh, A. A. Sokol Nature Materials 798–801 2013

[28] Ferrere S, Gregg B A, J. Am. Chem. Soc. 120, 843–844 (1998).

[29] Islam A, et al., New J. Chem. 24, 343–345 (2000).

[30] Kuciauskas D, et al., J. Phys. Chem. B 105, 392–403 (2001).

[31] Altobello S, et al., J. Am. Chem. Soc. 127, 15342–15343 (2005).

[32] A. Hagfeldt, G. Boschloo, L. Sun, L. Kloo, H. Pettersson, Chem. Rev. 110, 6595–6663, 2010

[33] Tachibana Y, et al., J. Phys. Chem. 100, 20056–20062 (1996).

[34] Kohle O, Gratzel M, Meyer A F, Meyer T B, Adv. Mater. 9, 904 (1997).

[35] G. E. Tulloch, Light and energy dye solar cells for the 21st century. Journal of Photochemistry and Photobiology A: Chemistry, 164: p. 209–219

[36] M. Gratzel et al., Highly efficient dye-sensitized solar cells based on carbon black counter electrodes. Journal of The Electrochemical Society, 2006. 153: p. A2255-A2261

[37] M. Gratzel, Conversion of sunlight to electric power by nanocrystalline dye-sensitized solar cells. Journal of Photochemistry and Photobiology A: Chemistry, 2004. 164: p. 3–14

[38] L.M. Peter et al, Electron transport in the dye sensitized nanocrystalline cell, Physica E, 2002. 14: p. 203 – 209.

[39] A. J. Frank, N. Kopidakis and J. van de Lagemaat, Electrons in nanostructured TiO2 solar cells: transport, recombination and photovoltaic properties. Coordination Chemistry Reviews, 2004. 248: p. 1165–1179

[40] Li-Chieh Chen, Jyh-Ming Ting, Yuh-Lang Leed, Min-Hsiung Hon, A binder-free process for making all-plastic substrate flexible dye-sensitized solar cells having a gel electrolyte, J. Mater. Chem., 2012, 22, 5596

[41] Lu-Yin Lin, Min-Hsin Yeh, Chuan-Pei Lee, Chen-Yu Chou, R. Vittal, Kuo-Chuan Ho, Enhanced performance of a flexible dye-sensitized solar cell with a composite semiconductor film of ZnO nanorods and ZnO nanoparticles, Electrochimica Acta 62 (2012) 341– 347

[42] Wenchao Huang, Xiao Li Zhang, Fuzhi Huang ,Zhipan Zhang, Jiangjing He, Yi-Bing Cheng, An alternative flexible electrode for dye-sensitized solar cells, J Nanopart Res (2012) 14:838

[43] Chun-Ren Ke, Jyh-Ming Ting, Anatase TiO2 beads having ultra-fast electron diffusion rates for use in low temperature flexible dye-sensitized solar cells, Journal of Power Sources 208 (2012) 316–321

[44] Hasitha C. Weerasinghe, Prasad M. Sirimanne, George P. Simon and Yi-Bing Cheng, Cold isostatic pressing technique for producing highly efficient flexible dye-sensitised solar cells on plastic substrates, Prog. Photovolt: Res. Appl. (2011)

[45] T. A. Nirmal Peiris, S. Senthilarasu, K. G. Upul Wijayantha, Enhanced Performance of Flexible Dye-Sensitized Solar Cells: Electrodeposition of Mg(OH)2 on a Nanocrystalline TiO2 Electrode, J. Phys. Chem. C 2012, 116, 1211–121

[46] Nian Qing Fu, Xu Rui Xiao, Xiao Wen Zhou, Jing Bo Zhang, Yuan Lin, Electrodeposition of Platinum on Plastic Substrates as Counter Electrodes for Flexible Dye-Sensitized Solar Cells, J. Phys. Chem. C 2012, 116, 2850−2857

[47] Xiong Yin, Zhaosheng Xue, Long Wang, Yueming Cheng, Bin Liu, High-Performance Plastic Dye-sensitized Solar Cells Based on Low- Cost Commercial P-25 TiO2 and Organic Dye, ACS Appl. Mater. Interfaces 2012, 4, 1709−1715

[48] Jingzhen Shao, Fengjuan Liu, Weiwei Dong, Ruhua Tao, Zanhong Deng, Xiaodong Fang, Songyuan Dai, Low temperature preparation of TiO2 films by cold isostatic pressing for flexible dye-sensitized solar cells, Materials Letters 68 (2012) 493–496

[49] Shanghua Wang, Jingbo Zhang, Shen Chen, Haotian Yanga, Yuan Lina, Xurui Xiao, Xiaowen Zhou, Xueping Li, Conversion enhancement of flexible dye-sensitized solar cells based on TiO2 nanotube arrays with TiO2 nanoparticles by electrophoretic deposition, Electrochimica Acta 56 (2011) 6184– 6188

[50] Xue-Long He, Mei Liua, Guan-Jun Yanga, Sheng-Qiang Fan, Chang-Jiu Li, Correlation between microstructure and property of electroless deposited Pt counter electrodes on plastic substrate for dye-sensitized solar cells, Applied Surface Science 258 (2011) 1377– 1384

[51] Hsin-Wei Chen, Chih-Peng Liang, Hou-Sheng Huang, Jian-Ging Chen, R. Vittal, Chia-Yu Lin, Kevin C.-W. Wu, Kuo-Chuan Ho, Electrophoretic deposition of mesoporous TiO2 nanoparticles consisting of primary anatase nanocrystallites on a plastic substrate for flexible dye-sensitized solar cells, Chem. Commun., 2011, 47, 8346–8348

[52] Xiong Yin, Zhaosheng Xue, Bin Liu, Electrophoretic deposition of Pt nanoparticles on plastic substrates as counter electrode for flexible dye-sensitized solar cells, Journal of Power Sources 196 (2011) 2422–2426

[53] Hsin-Wei Chen, Kuan-Chieh Huang, Chih-Yu Hsu, Chia-Yu Lin, Jian-Ging Chen, Chuan-Pei Lee, Lu-Yin Lin, R. Vittal, Kuo-Chuan Ho, Electrophoretic deposition of TiO2 film on titanium foil for a flexible dye-sensitized solar cell, Electrochimica Acta 56 (2011) 7991– 7998

[54] Hsin-Wei Chen, Chia-Yu Lin , Yi-Hsuan Lai, Jian-Ging Chen , Chun-Chieh Wang , Chih-Wei Hu , Chih-Yu Hsu, R. Vittal, Kuo-Chuan Ho, Electrophoretic deposition of ZnO film and its compression for a plastic based flexible dye-sensitized solar cell, Journal of Power Sources 196 (2011) 4859–4864

[55] Yaoming Xiao, Jihuai Wu, Gentian Yue, Jianming Lin, Miaoliang Huang, Leqing Fan, Zhang Lan, Fabrication of high performance Pt/Ti counter electrodes on Ti mesh for flexible large-area dye-sensitized solar cells, Electrochimica Acta 58 (2011) 621– 627

[56] Wei-Hao Chiu, Kun-Mu Lee, Wen-Feng Hsieh, High efficiency flexible dye-sensitized solar cells by multiple electrophoretic depositions, Journal of Power Sources 196 (2011) 3683–3687

[57] Yong Peng, Jefferson Zhe Liu, KunWang, Yi-Bing Cheng, Influence of Parameters of Cold Isostatic Pressing on TiO2 Films for Flexible Dye-Sensitized Solar Cells, International Journal of Photoenergy, 2011, 410352

[58] A. Vomiero, V. Galstyan, A. Braga, I. Concina, M. Brisotto, E. Bontempi, G. Sberveglieri, Flexible dye sensitized solar cells using TiO2 nanotubes, Energy Environ. Sci., 2011, 4, 3408

[59] Yaoming Xiao, Jihuai Wu, Gentian Yue, Jianmin Lin, Miaoliang Huang, Zhang Lan, Low temperature preparation of a high performance Pt/SWCNT counter electrode for flexible dye-sensitized solar cells, Electrochimica Acta 56 (2011) 8545– 8550

[60] Chia-Hu Lee, Wei-Hao Chiu, Kun-Mu Lee, Wen-Feng Hsieh, Jenn-Ming Wu, Improved performance of flexible dye-sensitized solar cells by introducing an interfacial layer on Ti substrates, J. Mater. Chem., 2011, 21, 5114

[61] Ke Fan, Chuqing Gong, Tianyou Peng, Junnian Chen, Jiangbin Xia, A novel preparation of small TiO2 nanoparticle and its application to dye-sensitized solar cells with binder-free paste at low temperature, Nanoscale, 2011, 3, 3900

[62] Cunxi Cheng, Jihuai Wu, Yaoming Xiao, Yuan Chen, Leqing Fan, Miaoliang Huang, Jianming Ling, Jiangli Wang, Ziying Tang, Gengtian Yue, Polyvinyl pyrrolidone aided preparation of TiO2 films used in flexible dye-sensitized solar cells, Electrochimica Acta 56 (2011) 7256– 7260

[63] Young-Wook Jang, Young-Keun Kim, Hyun-Woo Park, Du- Hyun Won, Sang-Eun Cho , Won-Pill Hwang , Ki-Suck Jung, Mi-Ra Kim, Jin-Kook Lee, Preparations and Characterizations of TiO2 Pastes for Flexible Dye-Sensitized Solar Cells, Mol. Cryst. Liq. Cryst., Vol. 538: pp. 240–248, 2011

[64] You-Han Chen, Kuan-Chieh Huang, Jian-Ging Chen, R. Vittal, Kuo-Chuan Ho, Titanium flexible photoanode consisting of an array of TiO2 nanotubes filled with a nanocomposite of TiO2 and graphite for dye-sensitized solar cells, Electrochimica Acta 56 (2011) 7999– 8004

[65] Takeshi Yamaguchi, Nobuyuki Tobe, Daisuke Matsumoto, Takuma Nagai, Hironori Arakawa, Highly efficient plastic-substrate dye-sensitized solar cells with validated conversion efficiency of 7.6%, Solar Energy Materials & Solar Cells, 94, (2010),812–816

[66] Wei Chen, Yongcai Qiu, Shihe Yang, A new ZnO nanotetrapods/SnO2 nanoparticles composite photoanode for high efficiency flexible dye-sensitized solar cells, Phys. Chem. Chem. Phys., 2010, 12, 9494–9501

[67] Jian-Ging Chen, Chia-Yuan Chen, Chun-Guey Wu, Chia-Yu Lin, Yi-Hsuan Lai, Chun-Chieh Wang, Hsin-Wei Chen, R. Vittal, Kuo-Chuan Ho, An efficient flexible dye-sensitized solar cell with a photoanode consisting of TiO2 nanoparticle-filled and SrO-coated TiO2 nanotube arrays, J. Mater. Chem., 2010, 20, 7201–7207

[68] Ke Fan, Tianyou Peng, Bo Chai, Junnian Chen, Ke Dai, Fabrication and photoelectrochemical properties of TiO2 films on Ti substrate for flexible dye-sensitized solar cells, Electrochimica Acta 55 (2010) 5239–5244

[69] Lili Chen, Weiwei Tan, Jingbo Zhang, Xiaowen Zhou, Xiaoling Zhanga, Yuan Lin, Fabrication of high performance Pt counter electrodes on conductive plastic substrate for flexible dye-sensitized solar cells, Electrochimica Acta 55 (2010) 3721–3726

[70] Yuelong Li, Kicheon Yoo, Doh-Kwon Lee, Jong Hak Kim, Nam-Gyu Park, Kyungkon Kim, Min Jae Ko, Highly bendable composite photoelectrode prepared from TiO2/polymer blend for low temperature fabricated dye-sensitized solar cells, Current Applied Physics 10 (2010) e171-e175

[71] H.C. Weerasinghe, P.M. Sirimanne, G.V. Franks, G.P. Simon, Y.B. Cheng, Low temperature chemically sintered nano-crystalline TiO2 electrodes for flexible dye-sensitized solar cells, Journal of Photochemistry and Photobiology A: Chemistry 213 (2010) 30–36

[72] Qinghui Zeng, Yuan Yu, Liangzhuan Wu, Bin Qi, Jinfang Zhi, Low-temperature fabrication of flexible TiO2 electrode for dye-sensitized solar cells, Phys. Status Solidi A 207, No. 9, 2201–2206 (2010)

[73] Lu-Yin Lin, Po-Chin Nien, Chuan-Pei Lee, Keng-Wei Tsai, Min-Hsin Yeh, R. Vittal, Kuo-Chuan Ho, Low-Temperature Flexible Photoanode and Net-Like Pt Counter Electrode for Improving the Performance of Dye-Sensitized Solar Cells, J. Phys. Chem. C 2010, 114, 21808–21815

[74] Lu-Yin Lin, Chuan-Pei Lee, R. Vittal, Kuo-Chuan Ho, Selective conditions for the fabrication of a flexible dye-sensitized solar cell with Ti/TiO2 photoanode, Journal of Power Sources 195 (2010) 4344–4349

[75] Aurelien Du Pasquier, Mattew Stewart, Timothy Spitler, Mike Coleman, Aqueous coating of efficient flexible TiO2 dye solar cell photoanodes, Solar Energy Materials & Solar Cells 93 (2009) 528–535

[76] Kun-Mu Lee, Shi-Jhang Wu, Chia-Yuan Chen, Chun-Guey Wu, Masashi Ikegami, Kozo Miyoshi, Tsutomu Miyasaka, Kuo-Chuan Ho, Efficient and stable plastic dye-sensitized solar cells based on a high light-harvesting ruthenium sensitizer, J. Mater. Chem., 2009, 19, 5009–5015

[77] Weiwei Tan, Xiong Yin, Xiaowen Zhou, Jingbo Zhang, Xurui Xiao, Yuan Lin, Electrophoretic deposition of nanocrystalline TiO2 films on Ti substrates for nuse in flexible dye-sensitized solar cells, Electrochimica Acta 54 (2009) 4467–4472

[78] H.C.Weerasinghe, P.M. Sirimanne, G.P. Simon, Y.B. Cheng, Fabrication of efficient solar cells on plastic substrates using binder-free ball milled titania slurries, Journal of Photochemistry and Photobiology A: Chemistry 206 (2009) 64–70

[79] Zhaoyue Liu, Vaidyanathan (Ravi) Subramania, and Mano Misra, Vertically Oriented TiO2 Nanotube Arrays Grown on Ti Meshes for Flexible Dye-sensitized Solar Cells, J. Phys. Chem. C 2009, 113, 14028–14033

[80] Daibin Kuang, Jeremie Brillet, Peter Chen, Masakazu Takata, Satoshi Uchida, Hidetoshi Miura, Kohichi Sumioka, Shaik. M. Zakeeruddin, Michael Gratzel, Application of Highly Ordered TiO2 Nanotube Arrays in Flexible Dye-Sensitized Solar Cells, ACS Nano, Vol. 2, No. 6

[81] Jong Hyeok Park, Yongseok Jun, Ho-Gyeong Yun, Seung-Yup Lee, Man Gu Kang, Fabrication of an Efficient Dye-Sensitized Solar Cell with Stainless Steel Substrate, Journal of The Electrochemical Society, 155, 7,F145-F149,2008

[82] Xizhe Liu, Yanhong Luo, Hong Li, Yuzun Fan, Zhexun Yu, Yuan Lin, Liquan Chena and Qingbo Meng, Room temperature fabrication of porous ZnO photoelectrodes for flexible dye-sensitized solar cells, Chem. Commun., 2007, 2847–2849

[83] Yongseok Jun, Jongdae Kim, Man Gu Kang, A study of stainless steel-based dye-sensitized solar cells and module, Solar Energy Materials & Solar Cells 91 (2007) 779–784

[84] Yongseok Jun, Man Gu Kang, The Characterization of Nanocrystalline Dye-Sensitized Solar Cells with Flexible Metal Substrates by Electrochemical Impedance Spectroscopy, Journal of The Electrochemical Society, 154, 1, B68-B71, 2007

[85] Seigo Ito, Ngoc-Le Cevey Ha, Guido Rothenberger, Paul Liska, Pascal Comte, Shaik M. Zakeeruddin, Peter Pechy, Mohammad Khaja Nazeeruddin, Michael Gratzel, High-efficiency (7.2%) flexible dye-sensitized solar cells with Ti-metal substrate for nanocrystalline-TiO2 photoanode, Chem. Commun., 2006, 4004–4006

[86] G. N. Howatt, Method of Producing High-Dielectric High-Insulation Ceramic Plates, US Patent 2582993

[87] P. Gaskell, B. Rand, J. Summers, H. Thompson, The effect of reservoir geometry on the flow within ceramic tape casters. J. of the Europ. Ceram. Soc., 17, 1185 (1997)

[88] R. Runk, M. Andrejco, A precision tape casting machine for fabricating thin ceramic tapes, A. Ceram. Soc. Bull., 54(2), 199 (1975)

[89] Kirby B. Micro- and Nanoscale Fluid Mechanics: Transport in Microfluidic Devices (1st edition), Cambridge, NY 2010

[90] Besra L, Zha S, Liu M. Preparation of NiO–YSZ/YSZ Bi-layers for solid oxide fuel cells by electrophoretic deposition. J Power Sources, in press.

[91] J.H. Dickerson, A.R. Boccaccini, P.J. Sides, “Fundamentals of Electrophoretic Deposition. Electrophoretic deposition of nanomaterials”, Springer, New York 2012

[92] Ferrari B, Moreno R. The conductivity of aqueous Al2O3 slips for electrophoretic deposition. Mater Lett 1996;28:353–5.

[93] Ferrari B, Moreno R. Electrophoretic deposition of aqueous alumina slip. J Eur Ceram Soc 1997;17: 549–56.

[94] Hirata Y, Nishimoto A, Ishihara Y. Nippon Seramikkusu Kyokai Gakujutsu Ronbunshi 1991;99:108.

[95] Fischer R, Fischer E, De Portu D, Roncari E. Preparation of ceramic micro-laminate by electrophoresis in aqueous system. J Mater Sci Lett 1995;14(1):25–7.

[96] Ishihara T, Sato K, Takita Y. Electrophoretic deposition of Y2O3 stabilised ZrO2 electrolyte films in solid oxide fuel cells. J Am Ceram Soc 1996;79(4):913–9.

[97] Mathews T, Rabu N, Sellar JR, Muddle BC. Fabrication of La1-xSrxGa1-yMgyO3-(x+y)/2 thin films by electrophoretic deposition and its conductivity measurement. Solid State Ionics 2000;128:111–5.

[98] Peng Z, Liu M. Preparation of dense platinum-yttria stabilized zirconia and yttria stabilized zirconia films on porous La0.9Sr0.1MnO3 (LSM) substrates. J Am Ceram Soc 2001;84(2):283–8.

[99] Ducheyne P, Radin S, Heughebaert M, Heughebaert JC. Calcium phosphate ceramic coatings on porous titanium: effect of structure and composition on electrophoretic deposition, vacuum sintering and in vitro dissolution. Biomaterials 1990;11(4):244–54.

[100] Abolmaali SB, Talbot JB. Synthesis of superconductive thin films of YBa2Cu3O7-x by a nonaqueous electrodeposition process. J Electrochem Soc 1993;140:443.

[101] Nicholson PS, Sarkar P, Haung X. Electrophoretic deposition and its use to synthesize zirconia/alumina micro-laminate ceramic/ceramic composites. J Mater Sci 1993;28(23):6274–8.

[102] Zhitomirsky I, Petric A. Electrolytic and electrophoretic deposition of CeO2 films. Mater Lett 1999;40: 263.

[103] Zhitomirsky I. JOM-e Miner Met Mater Soc J 52;2000. Retrieved from: www.tms.org_pubs_journals_JOM_0001_Zhitomirsky_Zhitomirsky-0001.html. (Accessed on 07.07.2014)

[104] Hayashi S, Nakagawa Z, Yasumori A, Okada K. Effects of H2O in EtOH–H2O disperse medium on the electrophoretic deposition of CaSiO3 fine powder. J Eur Ceram Soc 1999;19(1):75–9.

[105] Yamashita K, Nagai M, Umegaki T. Fabrication of green films of single and multi-component ceramic composites by electrophoretic deposition technique. J Mater Sci 1997;32:6661–4.

[106] Van Tassel J, Randall CA. Electrophoretic deposition and sintering of thin/thick PZT film. J Eur Ceram Soc 1999;19:955–8.

[107] Foissy AA, Robert G. Bull Am Ceram Soc 1982;61:251.

[108] Andrews JM, Collins AH, Cornish DC, Dracass J. Proc Brit Ceram Soc 1969;12:211.

[109] Kopeliovich D. Isostatic Pressing of Metal Powders, 2014. Retrieved from: http://www.substech.com. (Accessed on 17.07.2014)

[110] Larissa Grinis, Snir Dor, Ashi Ofir, Arie Zaban Journal of Photochemistry and Photobiology A: Chemistry 198 (2008) 52–59